UNIVERSITY OF OKLAHOMA

GRADAUTE COLLEGE

ENGINEERED BACTERIOPHAGE ENABLED NANOPROBES FOR SKBR-3 CANCER CELL SPECIFIC IMAGING AND THERAPY

A DISSERTATION

SUBMITTED TO THE GRADUATE FACULTY

in partial fulfillment of the requirements for the

Degree of

DOCTOR OF PHILOSOPHY

BY
GOPAL NAGA VENKATA ABBINENI
Norman, Oklahoma
2011

ENGINEERED BACTERIOPHAGE ENABLED NANOPROBES FOR SKBR-3 CANCER CELL SPECIFIC IMAGING AND THERAPY

A DISSERTATION APPROVED FOR THE
DEPARTMENT OF CHEMISTRY AND BIOCHEMISTRY

BY:

_____
Dr. Chuanbin Mao, Chair

_____
Dr. Helen I. Zgurskaya

_____
Dr. Barbara Safiejko-Mroczka

_____
Dr. Susan Schroeder

_____
Dr. Daniel T. Glatzhofer

_____
Dr. Scott Russell

Acknowledgements

Firstly, I would like to thank my major advisor, Dr. Chuanbin Mao for accepting me as his graduate student and providing me an opportunity to work in his lab. His hard work and persistent behavior motivated me to work hard in his lab during the last five years. He gave me complete freedom and encouraged me to learn several interesting techniques within and outside his lab. This provided me a great opportunity to enhance and broaden my research skills necessary for science. I would like to thank Dr. Barbara Safiejko-Mroczka, for all her support, help and guidance. In the last two years she spent lot of her valuable time in teaching me specialized techniques in cell biology. She gave me complete freedom to use her lab for my research purpose. Personally, she has been very kind and affectionate to me. I would like to thank my committee members Dr. Helen Zgurskaya, Dr. Susan Schroeder, Dr. Daniel T. Glatzhofer and Dr. Scott Russell for providing me an opportunity to pursue my doctoral degree in this department and providing valuable suggestions during general exam and annual evaluations. I would like to thank Dr. Ivan Yip for help, suggestions and discussions. I would like to specially thank my dearest friend and well wisher Sita Devi Modali for everything she provided me in the last 12 years. She has been a great supporter and friend of mine since 1998 when we were doing our under graduation at Dr. L. Bullayya College, India. Without her support and help it might have not been possible for me to come to United States. She helped me to join this university, department and this lab. In spite of her personal issues she constantly provided me a helping hand in difficult situations. I also would like to

thank all my undergraduate lecturers who encouraged me to pursue my higher studies in abroad. I would like to thank all post doctoral fellows in our lab namely Dr. Naveen Gandra, Dr. Ananta laxmi Ayyagari, Dr. Haibo Zhu, Dr. Zipeng Zhen, Dr. Kay Guo, Dr. Pascaline Ngweniform, Dr. Ziwei Zeng, Dr. Helen Lu, Dr. Aihua Liu, Dr. He Tao, Dr.Sreeram Kalarical, Dr.Shoba Narayan, Dr.Sundaram Meenakshi, and Dr. Fuke Wang, for sharing their knowledge with me and their help in my research. I would like to thank my lab members Dong Li, Penghe Qiu, Binrui Cao, Harold Castano, Xu Hong and Dong Dong for all their help and friendly suggestions. I would like to thank my undergraduate students Byung Kim, April Clevenger and Christina Jensen for their help in my research work. Thanks to my friends from other labs Steven Harris, Sachin Chavhan, Rahul Kadam, and Nehul Shah for sharing their joys and happiness.

I would like to say big thanks to my father A.V.Satyanarayana, mother A.Vijaya Lakshmi and brother A.Venu Gopal for all their sacrifices to give me a great life. I would like to thank the Almighty GOD Saibaba for the opportunity and blessing bestowed upon me.

Table of Contents

List of Tables

Chapter 2

Chapter 3:

List of Figures

Chapter 1:

Chapter 2:

Abbreviations

ADH	**Atypical ductal hyperplasia**
ATP	**Adenosine triphosphate**
BOC	**tert-Butyl carbamate**
BSA	**Bovine serum albumin**
CDR	**Complimentary determining regions**
Cfu	**Colony forming unit**
CNTs	**Carbon nanotubes**
CTAB	**Hexadecyl trimethyl ammonium bromide**
DAPI	**4', 6-diamidino-2-phenylindole**
DCIS	**Ductal carcinoma insitu**
DMSO	**Dimethyl sulfoxide**
DOTAP	**1,2-dioleoyl-3- trimethylammonium propane chloride**
DOPC	**1,2-dioleoyl-sn-glycerophosphocholine**
EDC	**1-Ethyl-3-(3-dimethylaminopropyl)carbodiimide**
EGF	**Epidermal growth factor**
ELISA	**Enzyme linked immune sorbent assay**
E8	**Eight glutamic acid residues**
FITC	**Fluorescein isothiocyanate**
FTIR	**Fourier transform infrared spectroscopy**

GNRs	**Gold nanorods**
HBEC	**Human breast epithelial cancer lines**
H&E	**Hematoxylin and eosin staining**
RELIC	**REceptor Ligand Contacts**
RF	**Replicative form**
MeSH	**Mercapto ethanol**
Mol wt	**Molecular weight**
MSCs	**Mesenchymal stem cells**
MTT	**3-(4,5-dimethylthiazol-2-yl)-2,5-diphenyl tetrazolium bromide**
MUDA	**11-Mercaptoundecanoic acid**
MWCNT	**Multi walled carbon nanotube**
Nacl	**Sodium chloride**
NAP	**Sodium ammonium phosphate**
NHS-Dextran	**N-hydroxysuccinimide-dextran**
NIR	**Near infra red**
PAGE	**Polyacrylmide gel electrophoresis**
PDT	**Photo dynamic therapy**
PPa	**Porphyrin, pyropheophorbid-a**
PTT	**Photo thermal therapy**
PCR	**Polymerase chain reaction**
Phage-PPA	**Phage-porphyrin, pyropheophorbid-a complex**
PEI	**Polyethylenimine**

PEG	**Polyethylene glycol**
SCC	**Squamous cell carcinoma**
SDS	**Sodium dodecyl sulphate**
SPR	**Surface plasmon resonance**
ssDNA	**Single stranded DNA**
TBS	**Tris buffered saline**
TEM	**Transmission electron microscopy**
TGF α	**Transforming growth factor α**
TKI	**Tyrosine kinase inhibitors**
WT	**Wild type**
ZnPc	**Zinc phthalocyanine**

Abstract

With the recent progress in nanoscience and great deal of understanding in molecular biology, it is now possible to combine genetic tools with synthetic nano-constructs for improved biotechnology applications. Viruses with its inherent nanosize architecture, genetic flexibility, stability to harsh conditions, circulatory behavior and targeting ability, in combination with nano science, are currently an excellent source for designing nano based therapeutics for cancer diagnosis and treatment. Here, we integrate phage display technology (PDT) with nanotechnology to synthesize novel nano-conjguates for potential biomedical applications.

The first part of this dissertation is focused on the identification and characterization of novel SKBR-3 breast cancer cell targeting/internalizing ligands using landscape phage libraries. We used several computational methods and biochemical approaches to characterize the specificity, affinity and selectivity of the screened bacteriophage against target SKBR-3 breast cancer cells. In order to understand the mechanism of entry, we investigated the actin dynamics by using live cell and fluorescence imaging during selected phage internalization into target SKBR-3 cells. In conclusion, we demonstrate that phage harboring VSSTQDFP and DGSIPWST peptides could selectively internalize into SKBR-3 cells with high affinity and show rapid involvement of membrane ruffling and rearrangements of actin cytoskeleton during phage entry.

The second part of this dissertation is focused on the isolation of major coat proteins, pVIII from screened bacteriophage, its conjugation on functionalized gold

nanorod using appropriate chemistry and its multipurpose applications. The successful conjugation of coat proteins on functionalized gold nanorods was verified by using spectroscopic and microscopic techniques. In conclusion, we demonstrate that the resulting protein/peptide- nanoconjugates can be used for imaging and selective photo thermal destruction of SKBR-3 breast cancer cells upon exposure to near-infrared (NIR) light. In order, to gain insight into the mechanism and understand the key cellular processes involved following the treatment of these nanoconjugates, we used illumina microarray technique to explore the molecular interactions with in our model SKBR-3 breast cancer cells. We identified 76 genes to be up regulated and 26 genes are down regulated following the treatment of protein nanoconjugates. Our recent preliminary animal studies in SKBR-3 tumor model (nude mice) shows that these protein-nanoconjugates are feasible for in vivo applications. However, more *in vivo* experiments are under investigations before its clinical significance is realized.

The third part of this dissertation is focused on the assembly of coat proteins on functionalized carbon nanotubes and other biomedical applications of engineered bacteriophage in nanoscience. Using various spectroscopic and microscopic studies, we demonstrate phage proteins assembled on carbon nanotubes can be used for imaging purpose, and SKBR-3 specific bacteriophage can be used as a template for conjugation of photosensitizer, pyropheophorbid-a for targeted photo dynamic therapy. We also demonstrate filamentous bacteriophage displayed with eight glutamic acid residues [E_8] on the N-terminus of major coat protein using phage display can be used as a template to assemble liposomes and form phage-liposome complex for targeted drug delivery.

Chapter1: Introduction

1.1. Bacteriophage libraries and their applications

1.1.1. Structure and Biology of Filamentous bacteriophage

Bacteriophages are a group of viruses that infect bacteria. Filamentous bacteriophage is a flexible rod like virus (with ~0.9 μm length and ~6.5 nm width) that specifically infects a wide variety of gram negative bacteria, including *Escherichia coli, Xanthomonas, Pseudomonas and Salmonella* [1]. Previous X-ray diffraction studies identified two classes of filamentous viruses: Class I, includes M13, fd, f1 and Ike, and Class II, includes Pf1 and Xf [2]. Here, the discussion is restricted to Class I viruses (M13 and fd specifically) as they were well characterized and were used in this dissertation research. Class I viruses are grouped under Ff class because of their host cell entry through F conjugative pilus on the surface of male *E. coli* cells [3]. The Ff phage genome encodes a total of 11 proteins including five structural proteins (pVIII, pIII, pVI, pVII, and pIX), and six non structural proteins (pI, pXI, pIV, pII, pX, and pV) [4]. The intact Ff viruses posses single stranded (ss)-DNA as its genome surrounded by major and minor coat proteins. Figure 1-1A shows the schematic organization and the relative positions of all structural proteins on filamentous bacteriophage [5] and Figure 1-1B shows the electron micrograph of filamentous bacteriophage [6]. In M13 bacteriophage, Gene VIII codes for approximately 2700 copies of major coat proteins pVIII (50 amino acids and Molecular weight 5253) which constitutes the major fraction (~85%) of the virus

particles. It forms a thin flexible cylinder around the single-stranded DNA. Each pVIII subunit is α-helical protein with three distinct domains: [7] acidic N-terminus domain (residues 1-20) exposed to the solvent; basic C-terminal domain (residues 40-50) with four lysine residues responsible for electrostatic interactions with the negative charge DNA backbone; and a hydrophobic core (residues 21-39) responsible for protein-protein interactions in the major coat. The proximal end of the bacteriophage has five copies of minor coat proteins, namely pIII (406 amino acids, and mol wt 42, 522) and pVI (112 aminoacids, and mol wt 12,342) encoded by Genes III and V1 respectively. pIII is essential for virus infection and pVI is responsible for mediating pIII attachment to virus particle. Structurally pIII consists of three separate domains namely two amino terminal domains N1 and N2 and one carboxyl terminal CT domain. All these three domains are connected by glycine rich repeats. On the other hand, the distal end of phage has approximately five copies of two small proteins encoded by Genes VII and IX. They are mainly responsible for initiation of viral assembly [8].

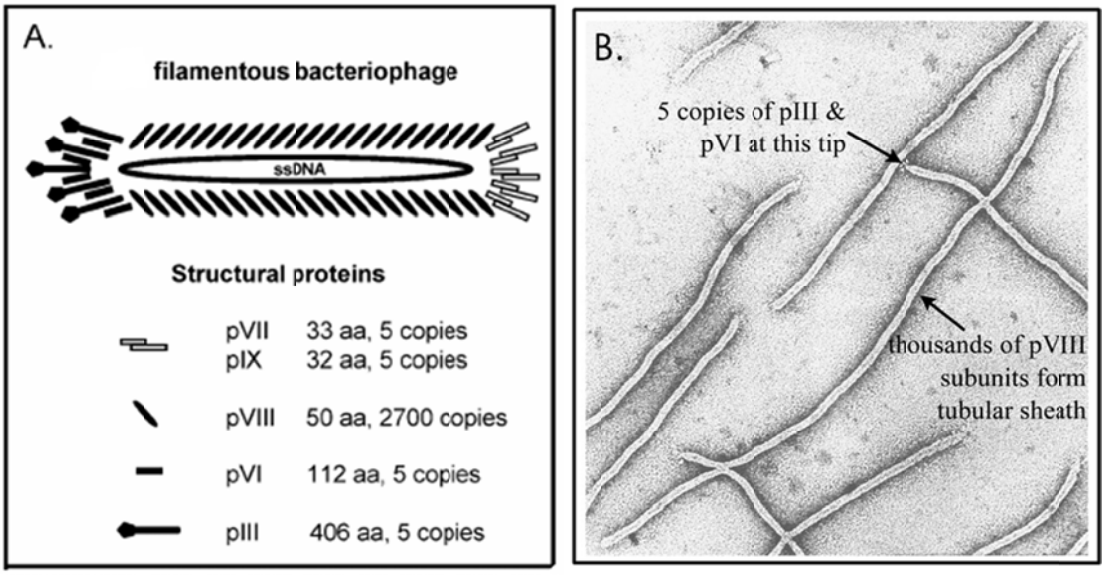

Figure 1-1: Structure of filamentous bacteriophage A. Typical structure of filamentous bacteriophage with relative positions of coat proteins figure adapted with permission from Ref [5]. B. Transmission electron micrograph of a phage figure adapted with permission from Ref [6].

Figure 1-2 shows the life cycle of filamentous bacteriophage Ff [9]. Filamentous phage infection begins with the binding of N2 domain of pIII to the tip of F-pilus on bacterial surface [3]. When the F- pilus on the bacteria is retracted, the coat proteins get integrated with bacterial cell membrane and the uncoating and translocation of viral DNA (positive strand) into the host cell cytoplasm takes place. Inside the bacterial cytoplasm, a complementary single strand (negative strand) DNA is synthesized using the host cell machinery (polymerases) to form the double stranded replicative form (RF). In the presence of replication proteins pII, pX, rolling circle replication takes place and

produces progeny phage. Later in the infection, when ss-DNA binding protein pV reaches high concentration, it anchors and sequesters plus strands into filamentous complex. Finally, during the extrusion of progeny virus, the five coat proteins are incorporated into the nascent virus [10]. As the phage does not kill the bacterial cells during this infection process, its life cycle is called non-lytic. However, the infected bacterial cells undergo comparatively slow cell division than normal bacterial cells [11]. Thus, viruses can be simply produced in large quantities by inoculating bacterial cultures with phage suspension under natural and appropriate conditions.

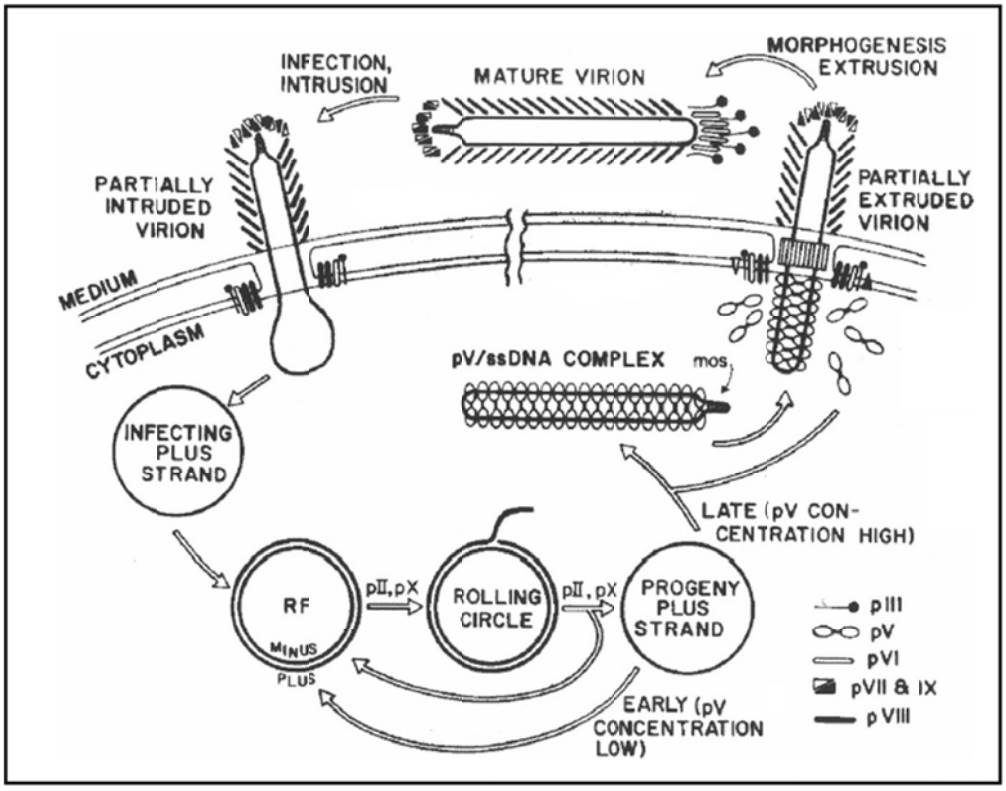

Figure 1-2: Infection cycle of filamentous bacteriophage Ff (figure adapted with permission from Ref [9]).

1.1.2. Evolution and Construction of Phage libraries

Genetic engineering has been proven to be an invaluable tool in molecular biology allowing the direct manipulation of genes in organisms such as bacteria, viruses, insect cells, and yeasts resulting in the display of desired guest peptides or proteins on the surface of these biomolecules [12]. Since the inception of genetic engineering in late 1970's, phage based vectors were chosen to be the first cloning vectors [13]. Later, because of their structural simplicity, ability to grow in bacterial hosts, and withstand extreme conditions (high pH's and temperatures) along with greater understanding of filamentous phage biology, they were chosen as suitable candidates for phage display.

Phage display is simply defined as incorporation of foreign peptides/polypeptides on the surface of phage particle. This is achieved by splicing a gene encoding a unique peptide into the phage genome [14]. Phage display took its birth in 1985 when George Smith successfully cloned a fragment of *E*coR1 endonuclease gene into the middle of minor coat protein, pIII of M13 bacteriophage [15]. After that several researchers have successfully displayed foreign peptides, proteins and antibodies on the surface of variety of viruses. Even though a number of other display systems such as bacteria [16] , insects [17] , yeast [18] and other bacteriophages such as T4 [19] and λ [20] can be used, the following discussion is limited to filamentous bacteriophage display.

To date most of the filamentous phage display work using genetic engineering was limited to M13 and its close relative fd bacteriophage [21]. Even though any

structural protein (either major or minor coat protein) on the virus surface can be used for peptide display, fusion of foreign sequence to amino terminus of pIII or pVIII is most common approach [5]. Also, it is believed that minor coat proteins can display larger proteins more efficiently than major coat proteins. From previous studies phage can withstand up to 38 amino acid residues on the amino terminus of pIII without altering its assembly and infectivity [22].

There are several excellent reviews and books which discuss the design, construction and applications of phage display libraries [9, 14, 23, 24, 25]. During, 1985 and 1988 George Smith reported the first construction of random peptide libraries on the surface of filamentous bacteriophage and its use in identifying antibody accessible peptide inserts [15, 26, 27]. In 1996, Renata Pasqualini et. al. have reported the first *in vivo* selection of random peptide libraries by studying the organ selective targeting in mice models [28] . Currently these phage libraries are being applied on human beings to generate cancer targeting ligands. In 2006, David Krag et. al. have reported the first phase I clinical use of phage display libraries in human cancer patients [29].

In general, recombinant peptide libraries are constructed by using two different methodologies. One is by using a synthetic degenerate oligonucleotide construct and another is by adopting random mutagenesis. The first random peptide library generated by George Smith contained fUSE5 as a cloning vector [15, 26]. The resulting phage library consists of multi-billion recombinant phages generated by fusing random peptides

to the N- terminus of all five copies on minor coat proteins pIII or on major coat proteins, pVIII. If the random peptides are present on pIII protein, it is termed as type-3 library; and if the random peptides are present on pVIII proteins, then it is termed as type- 8 library. Even though display of foreign sequences on all five copies of minor coat proteins, pIII was achieved two decades ago, the display of fusion peptide on all copies of major coat proteins was not successful till recent years. In 1996 Valery Petrenko et. al. reported the first construction of landscape phage libraries (termed owing to the global functional moieties on the entire virus surface) [30] using f8-1 as a cloning vector. These phage libraries are used in the current dissertation work (as shown in Figure 1-3) and are obtained from Valery Petrenko upon request. These libraries are constructed by splicing degenerate oligonucleotide sequence into gene VIII of f8-1 phage based vector by shot gun approach [30]. The resulting recombinant phages with fusion peptides on all copies of pVIII subunits are called landscape phages and the collection of these phages are known as landscape phages. Similar to complimentary determining regions (CDR) on antibodies, foreign peptides are displayed in a fixed frame work on bacteriophage. These phage libraries exhibit emergent properties that are specific for a variety of targets. Hence, these libraries are mainly used to explore novel protein–protein interactions along with other interesting applications as discussed below.

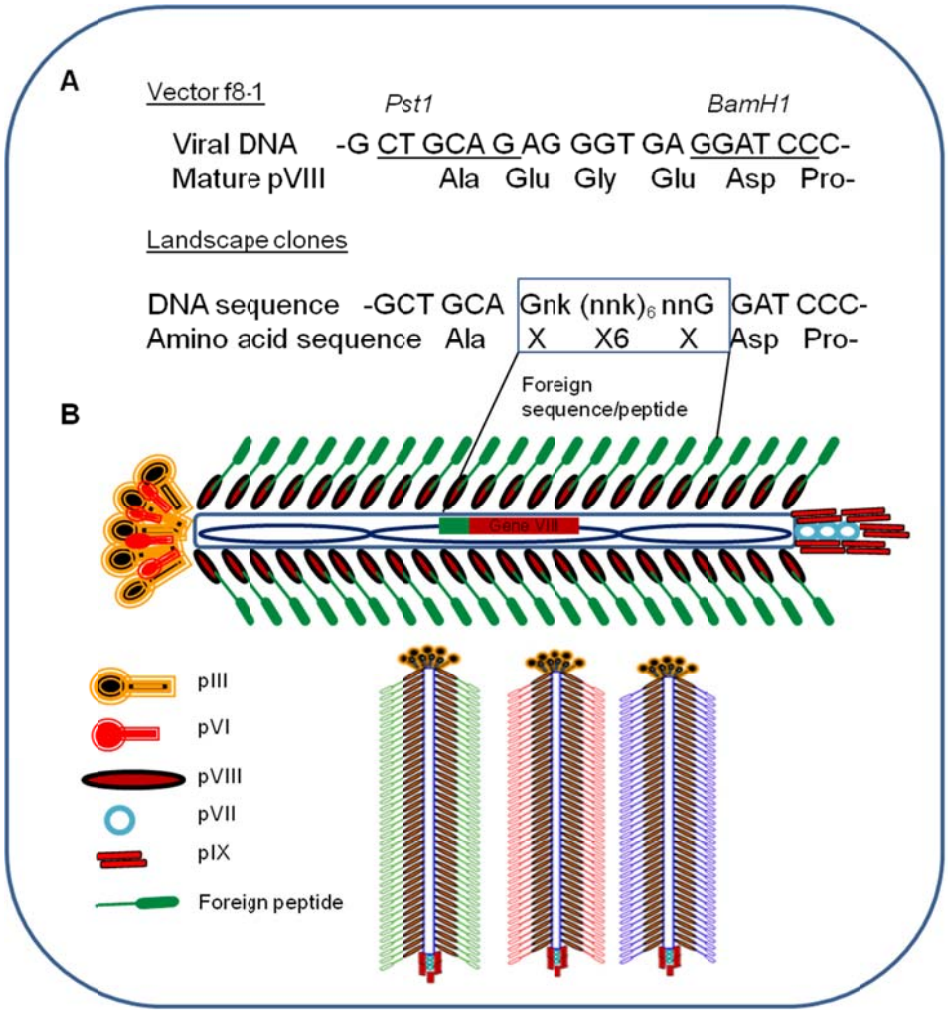

Figure 1-3: **Construction of landscape phage libraries**. (A) Nucleotide and corresponding amino acid sequence of pVIII (mature form) in vector f8-1 and recombinant VIII in the library: n represents equal mixture of G,A,T and C; k is an equal mixture of G and T [30]. (B) Cartoon showing the recombinant bacteriophage with foreign sequence incorporated at the gene VIII and resulting landscape phage libraries.

1.1.3. Applications of Phage Display Technology

There are numerous applications of phage display technology including studying protein-protein interactions [31], evaluation of small molecule drug candidates [32], selection of peptide mimotopes for vaccine production [33], gene targeting [34], tumor targeting [35] and epitope mapping [36]. Here, the discussion is limited to identification of novel targeting agents using phage libraries for understanding protein-protein interaction.

1.1.3.1. *In vitro* and *In vivo* screening of novel receptor-ligands complexes:

In most cases receptor-ligand (protein-protein) interactions occurs through three or four conserved residues (for example: RGD sequence binds to integrins). Hence it is believed phage libraries would provide a novel means to identify protein-protein interactions. A typical diagnostic assay uses antigens to detect the presence of antibodies in serum or blood; similarly phage libraries are used as a rich antigen source to identify known or unknown receptors present on a target cell. Thus, it is now possible to define the region of a protein/peptide recognized by an antibody based on the motifs revealed through phage display [22, 37].

Over the past two decades phage libraries have been successfully applied on numerous targets to determine epitopes to which antibody binds. Several researchers have successfully explored the applications of phage selection against purified antibodies [15], receptors [38] and whole cell extract [39]. Two interesting examples validating the use

of phage display technology are binding of tripeptide RGD to integrins bearing cell surface receptor [40] , and identification of highly conserved tyrosine residues when phage libraries are screened against SH2 domains [41].

Previous studies also confirmed that there is a functional link between the phage display identified peptides and receptors. For example, Annexin binds to beta 5 integrin and cause programmed cell death [42]. Previously, Cardo-Vila et. al. have carried out identification of β-5 integrins binding peptides using phage display libraries. When they synthesized the internalization version of the peptide using penetratin, their study clearly demonstrated the trigger of cell apoptosis in a caspase dependent manner [42]. This study validated that both structurally and functionally related targeting ligands can be obtained using random peptide libraries.

Initial studies of phage screening were limited to purified antibodies and receptors. Since mid 1990's to date, phage selection studies tremendously progressed towards heterogeneous cell surfaces including complex mammalian cell surface, *in vivo* animal and human tissues. For example, Goodson et.al. have isolated peptide ligands that bind to urokinase receptor using phage libraries [43] . Pasqualini *et.al.* was the first to identify targeting ligands that bind to renal and cerebral vacular endothelium using phage libraries [28]. *In vivo* phage display selection yielded novel targeting ligands against benign [44] and malignant diseases [45]. Hence, previous studies confirm phage libraries have been an in exhaustible tool for recognizing short ligands that specifically interact with target macromolecules with distinct confirmations.

The resulting cell specific affinity reagents from screening of phage libraries can be used for various bio-medical applications including delivery, diagnostics and therapeutics.

1.2. Cancer

Despite the progress in science during recent years, cancer continues to be one of the leading killers in United States with more than 1 million new cases every year [46]. Current treatment methods not only affect the disease cells but also harm the healthy cells. This resulted in a continuous demand for new therapeutic approaches to passively or actively destroy the cancer cells. Recent advancement in virology and material science provides a new direction to treat tumor.

1.2.1. Breast cancer:

Breast cancer is a major disease causing death among women in the United States. The estimated number of new breast cancer cases among American women in 2010 is approximately 207,090 and estimated deaths is 39,840 according to the statistics provided by American Cancer Society (ACS) in its annual cancer facts and figures [47].

Breast cancer is commonly associated with the over expression of epidermal growth factor receptors which are responsible for the normal breast tissue development and regulation [48]. Breast cancer is a heterogeneous disease that develops along a continuum [49] . There are five stages in breast cancer. Stage 0: It is also known as the noninvasive or *in situ* breast cancer. In this case the cancer cells do not possess an ability

to spread to other parts of the body. Stage 1-4 is invasive tumors which mean cancer acquires the ability to spread to other parts of the body. Stage 1 is local and can be easily cured. Stage 4 is very dangerous and can spread beyond breast to other organs. The normal breast terminal ductal lobular unit (TDLU) contains lobules and ducts made up of bilayered epithelial cells, namely outer luminal epithelial cell and inner myoepithelial cell. Any kind of abnormal changes in the luminal epithelial cells leads to breast cancer. During the progression of breast cancer first, atypical ductal hyperplasia (ADH) is developed which is characterized by an abnormal cell layers within the duct or lobule. It is also thought to be the precursor for ductal carcinoma *in situ* (DCIS) which gives rise to invasive breast cancer. The risk of metastasis increases once the cells start invading. It is also shown that the lymph nodes are the primary sites for breast cancer metastasis.

There are several methods to treat breast cancer patients; treatment usually depends on the type and stage of breast cancer. Treatments include surgery followed by additional therapy such as radiation, chemotherapy, hormone therapy and immunotherapy to remove the tumor tissue completely. However each approach has its own applications and limitations. Because of the heterogeneous nature of the breast tissue, it is highly essential to develop novel methods that target known or unknown receptors on breast cancer cell surface that may find clinical significance in the treatment of human breast cancer.

1.2.2. ErbB receptors and Signal transduction:

Receptor tyrosine kinases are the most common and play an important role in the transduction of extracellular signals into the cells [50]. Epidermal growth factor receptor (known as EGFR/HER1/ErbB1) and other ErbB family receptors (ErbB2/HER2, ErbB3/HER3 and ErbB4/HER4) are typical tyrosine kinase receptors implicated in breast cancer tissue and trigger cell proliferation, differentiation, survival and migration [50]. From earlier studies, it was found ErbB1 receptors are over expressed in 27-30% of breast tumors, and ErbB2 is over expressed in 20-25% of breast cancer patients [51]. Since mid 1990's ErbB receptors and their ligands were found to play crucial role in cell-cell interactions and responsible for aggressiveness and prognosis of variety of solid tumors [52]. Each of these four receptors has three main components, a highly glycosylated and ligand-binding extra-cellular domain, a middle transmembrane domain that crosses the cell membrane, and an intracellular kinase domain and a tyrosine residues containing cytoplasmic tail (as shown in Figure 1-4) [53].

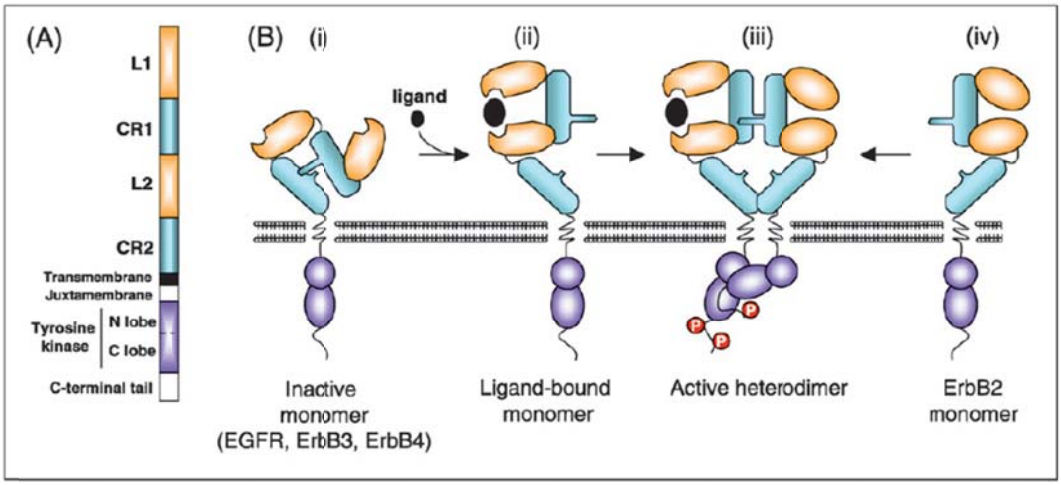

Figure 1-4: Structure of ErbB receptors figure adapted with permission from Ref [53].

All these four receptors share significant difference in their extra cellular and c-terminal tails but show homology in the kinase domain. Each receptor is characterized by binding to a unique ligand leading to protein-protein interactions and diverse signaling pathway. Normal signaling in ErbB receptors involves ligand-induced homo-dimerization or hetero-dimerization. So far at least twelve different soluble ligands binding to ErbB family members were found, including epidermal growth factor (EGF), epiregulin, β-cellulin, heparin binding (HB)- EGF, amphiregulin transforming growth factor and neuregulins [48]. Interestingly, to date no soluble ligands that binds to ErbB2 alone is identified. In addition, it was previously observed that the kinase domain of ErbB3 is catalytically inactive. Thus, even though a ligand can efficiently bind to ErbB3, it requires a heterodimer partner for signal transduction. When ligand binds (growth factor) to a receptor, a conformational change takes place in the extra cellular domain and results in the activation of cytoplasmic tyrosine kinase residues and stimulate signaling pathways that direct cellular process.

The activated ErbB receptors can result in diverse signaling pathways (as shown in Figure 1-5) [48]. There are four major signaling pathways used in erbB family members: Ras-Raf /MAP-Kinase pathway, STATs pathway, PI3K/Akt pathway and PLCγ (Phospho lipase Cγ) pathway. Under regular growth conditions, the expression and signal transduction of all these receptors are usually normal. But under extreme conditions, such as mutations or alteration in the gene or over expression or activation of

these genes or failure to counteract, may lead to abnormal growth of normal cells and may result to cancer.

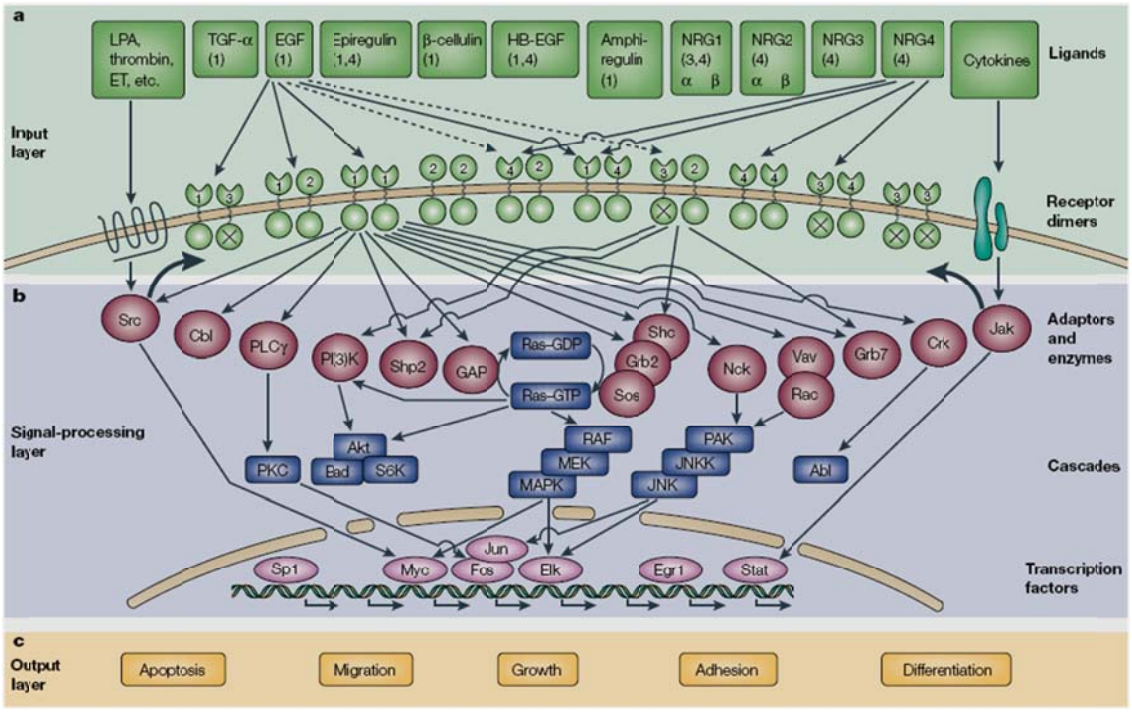

Figure 1-5: **Signaling pathways initiated by ErbB family members** figure adapted with permission from Ref [48].

Members of ErbB family receptors are frequently over expressed in a variety of solid tumors. Numerous therapeutic approaches that interfere with these receptors and neighboring members are under constant investigations.

1.2.3. ErbB receptor as target for breast cancer treatment :

As ErbB receptors are over expressed in breast cancer patients, it serves as an excellent candidate for targeted anti-cancer therapies [54]. At present most of the targeted approaches to treat breast cancer patients are centered towards ErbB2 receptor and other ErbB members.

There are three different approaches to inhibit the over expression of these receptors. One is to inhibit the ligand binding, two is to block the dimerization partner of the receptor by using monoclonal antibodies (as shown in Figure 1-6) and three is to inhibit the enzyme activity at the cytoplamic end. Currently, several biotech/pharmaceutical companies have come up with drugs that selectively inhibit one of the above mentioned processes [55]. Trastuzumab (Herceptin) and cetuximab are used in the treatment of breast tumor and colorectal centers by targeting the ErbB2 and ErbB1 respectively [56]. Erlotinib (AstraZeneca) and Gefitinib (Genentech/ OSI) are two small tyrosine kinase drugs that block the nucleotide binding pocket of ErbB1. Tyrosine Kinase inhibitors mainly attack the active tyrosine kinase domain of ErbB members and compete with ATP binding. On the other hand, monoclonal antibodies are designed to inhibit dimerization and/or induce anti-tumor immune response. Even though antibody therapy is an excellent approach to treat breast cancer, because of the complexity of cancer biology and the heterogeneous nature of human tissue, a single approach is not sufficient to destroy all tumors.

Hence, researchers around the world are constantly investigating new methods to image and destroy cancer. Having said that, here we design and develop a new approach to image and destroy the breast cancer cells. As a model, we chose ErbB2 positive breast cancer cells (SKBR-3) and ErbB2 negative normal breast cells (MCF-10A) cells.

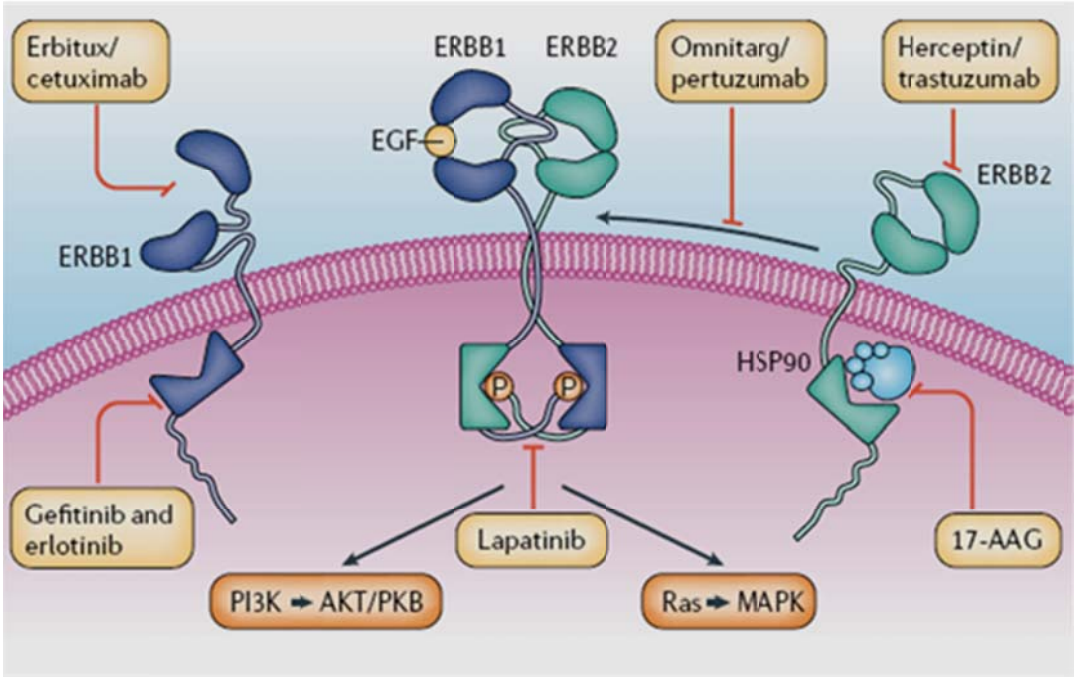

Figure 1-6: **ErbB family receptor based cancer therapy** figure adapted with permission from Ref [55].

1.3. Nanotechnology and its role in cancer treatment

Currently surgery, chemotherapy and radiation therapy represents the most common route to treat cancers [57]. However chemotherapy limitations in non specific uptake and inadequate distribution of antitumor agents and drugs resulted in searches for new and efficient methods to replace the traditional approaches. As the functional elements of biology (DNA, RNA and proteins) are in nanoscale range, nanotechnology is setting high expectations to explore biological processes [58]. Nanotechnology deals with the control of matter at the nano level. It utilizes multidisciplinary approach to provide devices that are in 1-1000 nm dimension range [59, 60]. A decade ago nanotechnology is primarily focused on attaining monodisperse synthesis and in understanding the physical and chemical properties of nanoparticles. Now it is largely extended to templated assembly and their biomedical applications.

Nanovectors (nano size particles which carry anti tumor drug or imaging agent) exhibits unique electronic, optical, magnetic and structural properties. Because of the availability of large surface area and easy functionalization with biomolecules, nanoparticles are viewed as an attractive agent for targeted cancer treatment [60]. Even though several nanovectors are available for biomedical applications, currently only few of them are clinically approved for targeted cancer treatment. Since there are several reviews which provide a clear perspective on the use of nanotechnology in cancer treatment [58, 60, 61], here I limit my discussion to few clinically approved nanovectors such as liposomes, polymeric nanoparticles [62, 63, 64] and nanoshells [65, 66, 67] for targeted cancer treatment and their mechanism of action (as shown in Figure 1-7).

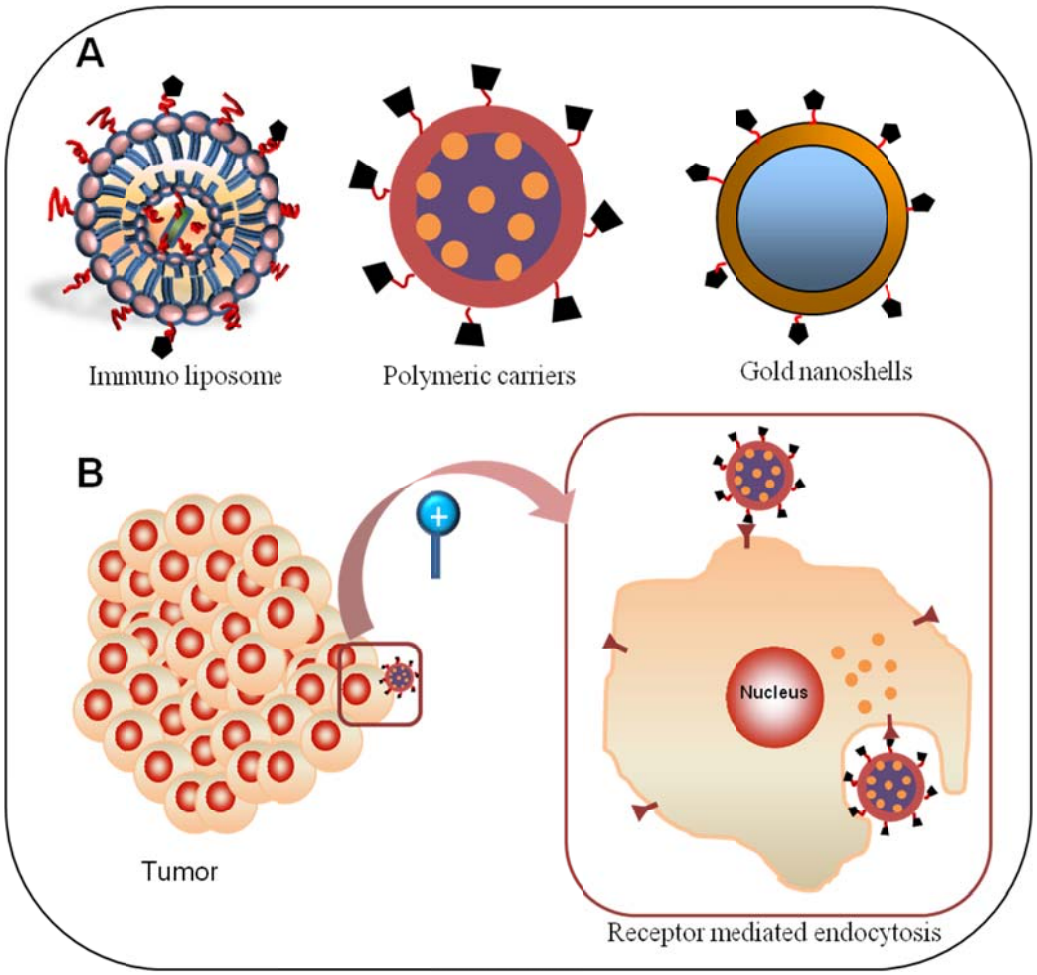

Figure 1-7: Novel nanovectors for targeted cancer treatment. A: Clinically approved nanocarrier's immunoliposomes, polymeric nanoconjugates, and gold nanoshells. B: Mechanism of action at the target tumour site is active targeting via receptor mediated endocytosis.

Earlier studies on tumor models showed there is an increased therapeutic upload upon conjugating targeting agents to nanocarriers with suitable chemotherapeutic [68,

69]. As the toxicity of the chemotherapeutic drug is enhanced if delivered selectively to a target tissue, new approaches for anticancer therapeutics using targeting ligands are accelerated [70]. These ligand mediated therapeutics are designed by associating the drug with antigen molecules that specifically binds to the receptors that are over expressed or uniquely present on the target cancer cell and not present in normal healthy cells. This targeting approach has been successfully applied to nanocarriers such as liposome (lipid based), polymers (organic polymer based) and nanoshells (inorganic gold based) and resulted in a new source for clinical products.

In mid-1980's liposomes emerged as an ideal candidate for drug delivery using passive targeting and received special attention because of their unique ability to isolate drug from the surrounding environment [71, 72]. However, the initial liposome composites are limited by their circulation times and serum instability. This resulted in the modification of liposomes with Polyethylene glycol (PEG) which later increased its *in vivo* circulation time and stability. Currently, conjugation of antigen specific ligands onto liposomal fractions carrying anticancer drug greatly improved the therapeutic efficiencies and reduced the adverse side effects of chemotherapy [73]. This resulting complex is termed immuno liposomes (as shown in Figure 6). At present, some of these liposome encapsulated formulations are in clinical use for Kaposi's sarcoma, Ovarian and Breast cancers [58]. In addition there are several other drug entrapped liposomal products which are in different phases of clinical trial and reviewed in great details elsewhere [74] .

Polymer-drug conjugates represent another interesting class of nanocarrier in which polymers are chemically conjugated with drugs. These polymeric drug conjugates contain a water-soluble polymer as a bioactive component to which drug are covalently attached. Previous studies showed polymeric micelle formulation of paclitaxel allowed increased uptake of the drug at the target site without significant toxicity [75]. Some of the polymer therapeutics such as Zinostatin and Adagen are currently in market and few others are under clinical trials for targeting blood vessels in tumors [58]. Likewise, metal based inorganic nanoparticles For Example: gold nanoshells (100-200nm size) are being used as an excellent source for hyperthermia. The gold nanoshells have central silica as a core surrounded by thin layer of gold. Recently, nanoshell based therapeutics received great attention in photo thermal therapy [67] and more recently reached clinical phases because of its great success in both *in vitro* and *in vivo* systems [66]. Currently these gold based nanoshells are under clinical trials for treating head and neck cancer.

Nanocarriers reach their target site using two different mechanisms. The first being passive targeting, and the second is active targeting. Passive targeting exploits the characteristics of tumor vasculature (leaky blood vessels). The new blood vessels formed in tumor tissue greatly differs from the normal blood vessels due to the presence of irregular shape, dilated vessels, and large gaps between endothelial cells. These characteristic features in tumor tissue allow the nanocarrier to enter into tumor tissue through enhanced permeability and retention effect (EPR effect) [76, 77, 78]. However

passive targeting may not be feasible in all cases as it is a random approach and some drugs (>200nm) cannot be diffused efficiently [58, 79]. In order to overcome the limitations resulting from passive targeting, the nanocarrier can be conjugated with tumour specific targeting ligands that bind specifically and tightly to cell surface through receptor-ligand interactions. The binding of some targeting ligands to the receptor may cause receptor-mediated endocytosis [70, 80] and results in the release of therapeutic drugs (as shown in Figure 1-7). For example, Earlier reports showed that certain breast cancer cells over express ErbB2 receptors on their surface and when doxorubicin encapsulated liposomes targeted with anti-ErbB2 antibody, it improved the therapeutic efficiency relative to the non targeted liposomal fraction [81]. Thus, the ultimate goal of nanotechnology is to properly integrate with established cancer biology (over expressing antigens) and develop more versatile, effective, sensitive and safer tools for tumour destruction.

1.4. Synthesis, Properties and Biomedical applications of Gold nanorods

1.4.1. Synthesis of Gold nanorods

Synthesis of metal nanoparticles has been of particular interest to scientists since 1857 when Michael Faraday was first fascinated by the ruby color of glass and reported the first synthesis of colloidal gold [82]. As the properties of nanoscale materials depend

on the size and shape of these particles, it is a great challenge to control the morphology of nanoparticles. Fortunately, there has been a tremendous progress in the synthesis of gold nanorods in the recent years [83].

In general, rod shaped nanoparticles can be synthesized in presence of rigid template or soft surfactant. Three different approaches are used to synthesize gold nanorods: photo chemical reduction method [84], electrochemical method [85], and seed mediated growth [86]. In all the methods discussed below, self assembled soft lipids are used as a source for the preparation of anisotropic gold nanorods. Among the three methods, photochemical reduction is the oldest method used to synthesize colloidal gold nanorods [87]. In this method, gold chloride ($HAuCl_4$) is first interacted with a cationic surfactant to form a complex ($AuCl_4^-$). When excited with UV light (253 nm), the metal ions are reduced to metal through electron transfer mechanism from ions to ligands. However, the resulting nanorods had several spherical gold nanoparticles in them. In order to synthesize gold nanorods with high yield, quality and mono-dispersity other methods are proposed [83, 85, 88] . In the electro chemical method, a gold metal plate is used as anode and a platinum plate is used as a cathode and are immersed in an electro chemical cell with surfactant hexadecyl trimethyl ammonium bromide (CTAB) as an electrolytic solution and stabilizing agent [85]. During electrolysis under controlled conditions (temperature and current), the bulk gold metal is converted to gold nanoparticles at the interface of cathode surface and electrolyte solution. The addition of acetone facilitated cylindrical growth of nanorods with an unknown mechanism [89].

Currently the most common and widely used method to synthesize nanorods is the modification of seed mediated growth [83] which was first reported by Jana et.al. in 2001 [86]. Synthesis of gold nanorods through a seed mediated growth takes place in a multi step process. In the first step a seed solution is prepared (3-4 nm of gold nanoparticles) by the reduction of gold chloride in the presence of CTAB with a strong reducing agent (sodium borohydride). In the second step, the growth of spherical seed is converted into rod in the surfactant environment. In the growth phase, mild reducing agent such as ascorbic acid is used for the reduction of gold salt into metallic nanorod along with the presence of gold seed. The synthesized nanorods are described by aspect ratio which is defined as the ratio of longitudinal length to the transverse length. The different aspect ratios of gold nanorods are controlled by adjusting the silver ion concentration. Thus, using any of the above mentioned methods, the synthesis of one dimensional gold nanorod takes place in a two step mechanism. One is crystal aggregation or nuclei formation, and the second is crystal stabilization and nanorod formation.

1.4.2. Properties of Gold nanorods

The properties of materials can be described by the evolution of electronic states from atoms to clusters and finally to bulk solids. In most cases, the physical and chemical properties of matter depend on the motion of electrons which are largely dependent on the type of materials and available space for their motion [89]. In bulk solids the energy

levels are considered to be continuous band of energy and not discrete where as in case of atoms, the energy levels are discrete. Thus, when the size of an object is reduced from bulk to small (nanosize), its electronic and optical properties are drastically changed. In particular, with plasmonic metals, the surface phenomenon gets predominant and gives unique optical properties to them.

The metal nanoparticles have oscillating electrons in the conduction band. When electromagnetic radiation hits a metal surface, its electric field component induces coherent collective oscillation of conduction band electrons with respect to the positive charged metallic core. This results in a collective oscillation of electron charge in resonance with the light frequency. This phenomenon is known as surface plasmon resonance (SPR) as shown in Figure 1-8 [90].

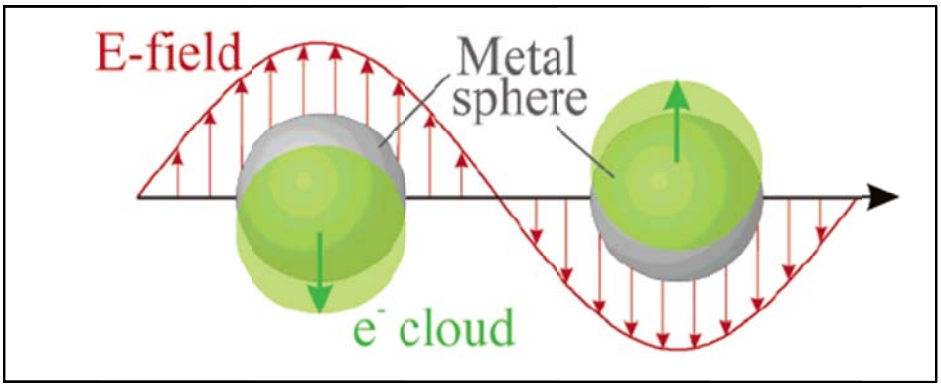

Figure 1-8. Scheme of Surface Plasmon Resonance (SPR) figure adapted with permission from Ref [90].

In case of gold nanorods, the electron oscillations takes place in two directions based on the polarization of incident light on the short and long axes resulting in two strong SPR bands, one in the visible region and the other in the NIR (near infra red) region (based on aspect ratio). These collective electron oscillations have a unique frequency that depends on the size, shape and interparticle distance. Since the resonant photons within the nanoparticles confine to their size, the amplitude of light wave is increased by several orders of magnitude. Hence, the radiative properties of metal nanoparticles such as absorption, scattering and phosphorescence are enhanced by several orders of magnitude [89].

Gans dipole approximation is used to explain the optical properties (absorption) of ellipsoid nanoparticles [91]. The absorption cross-section (σ_{abs}) for ellipsoid nanorods is given by the following equation.

$$\langle \sigma_{abs} \rangle = \frac{2\pi}{3\lambda} \varepsilon_m^{3/2} V \sum_i \frac{\varepsilon_2 / \left(n^{(i)}\right)^2}{\left(\varepsilon_1 + \frac{1-n^{(i)}}{n^{(i)}} \varepsilon_m\right)^2 + \varepsilon_2^2}.$$

Where ε_m is the dielectric constant of the medium, ε_1 and ε_2 are the real and imaginary components of the dielectric constant of gold, V is the particle volume, n^i is the depolarization factor in the i-th direction of nanorod. The difference in the absorption maxima of nanorods with various aspect ratios can be experimentally visualized by a

physical change in the color of nanorods as shown in Figure 1-9 [92, 93]. Thus, gold nanorods with desired aspect ratios can be synthesized based on the requirements. Previously, Juan et. al. have presented the theoretical basis for light scattering [94]. Gold nanorods scatter red light when illuminated with a beam of light. These scattering properties can be used for imaging applications as discussed below. Likewise, the strong surface plasmon absorption can be used to efficiently convert light into heat in a pico second time scale using laser radiation through electron-phonon and phonon-phonon interactions [95].

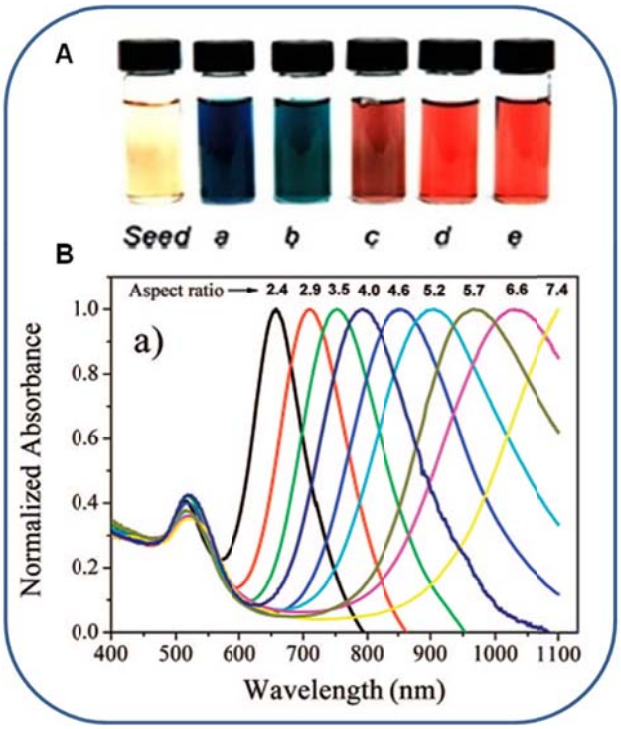

Figure 1-9. Optical absorption spectra of gold nanorods. A. Size dependent physical change in color figure adapted with permission from Ref [96]. B. Absorption spectra figure adapted with permission from Ref [92].

Currently, photo thermal therapy using near infra radiations (NIR) is receiving tremendous attention. This dissertation is aimed at synthesizing gold nanorods with strong absorption properties in the near infra red region (808nm).

1.4.3. Biomedical applications of Gold nanorods

Owing to its excellent radiative and non radiative properties and easy conjugation with biomolecules, gold nanorods are emerged as promising tools for biomedical applications including sensing, imaging, destruction, drug and gene delivery, and for catalytic efficiencies [89]. The SPR band resulting from absorption or scattering of incoming light can be used to monitor the changes in the local environment hence gold nanorods are well suited for plasmon sensing.

Previous studies by Yu et. al. have demonstrated that antibodies conjugated to gold nanorods using 11-Mercaptoundecanoic acid (MUDA) as a linker can simultaneously be used to detect multiplex surface markers on human breast epithelial cancer lines (HBEC) [97]. Nanorods act as strong contrast agents because of unique light-gold nanoparticle interactions (excitation). This enhances linear and nonlinear optical properties and offer ability for light scattered imaging [98]. Previously, Ding et al. have used dark field light scattering to image and monitor the uptake of nanorods into HeLa cells [99]. These nanorods can also be used for gene delivery applications. When gold nanorods are irradiated with pulse laser, they undergo changes in the shape; hence this strategy can be used to deliver DNA into the desired cell. Previous studies by Chen

et. al. have successfully demonstrated the release of thiolated enhanced green fluorescence protein (EGFP) from EGFP conjugated to gold nanorods using Nd:YLF laser [100]. Their study shows the release is due to thermal and electron heating of the particles. Similarly, conjugating gold nanorods with pH/temperature sensitive polymer could lead to the release of drug upon laser irradiation. Gold nanorods are also proved to be an excellent source of photo thermal agents for cancer destruction. For the first time in 2006, EI-Sayed and coworkers used plasmonic gold nanorods as photo thermal therapeutic agents to selectively destroy human oral cancer cells [98]. Recent studies are focused on their biocompatibility and there *in vivo* distributions. Niidome *et. al.* have developed a technique to quantitatively monitor the accumulation of gold nanorods in vivo animal models [101].

Thus gold nanorods provide exceptional optical properties for wide range of applications including cancer diagnosis and treatment. From recent progress in science using gold nanorods as photo thermal agents, there is a great chance for its advancement into clinical trials in the near future. The current research is also focused on understanding their role at molecular level.

1.5 Aims and Scope of this Dissertation.

A transition has occurred over the period of time in replacing the concept of virus as a toxic pathogenic agent to a useful agent for biomedical applications. In the last two decades, phage display technology is emerged as a powerful tool to identify unique cancer targeting ligands which can serve as a substituent's to antibodies. More recently, nanovectors with unique physical and chemical properties are currently being evolved as alternative tools for cancer diagnosis and treatment. Therefore, integration of engineered phage or phage derived components with nanomaterials might result in attractive and in-expensive tools for cancer imaging and therapy. Thus, the primary goal of this dissertation is to identify novel targeting ligands on SKBR-3 breast cancer cell surface and synthesize novel protein/peptide nanoconjugates that can be used for imaging and destruction of these breast cancer cells. In order to achieve this goal, the aims are 1) To identify and characterize new SKBR-3 breast cancer cell targeting ligands using landscape phage libraries and understand their mechanism of entry. 2) Synthesize multi functional nanoconjugates for cancer diagnosis and treatment and understand its role at molecular level. 3) Genetically modify bacteriophage surface and conjugate with nanoparticles for other biomedical applications.

Chapter 2 : Identification and Characterization of SKBR-3 breast cancer cell specific targeting peptides using landscape phage libraries.

2.1 Introduction

Breast cancer is one of the most serious deaths causing disease among women. Identification of new breast cancer cell-specific targeting or internalizing peptides is attractive for cancer imaging and therapy because they serve as excellent substitutes for antibodies on nanomaterials which are limited by their large size, cost of production and non specific binding to reticuloendothelial system [102].

The search for new cell-penetrating peptides has been very active in the recent years because they can assist in delivering molecules to a variety of cells. Earlier studies on tat protein from HIV-1 and antennapedia homeodomain from drosophila showed that short protein domains can cross the plasma membrane through translocation process [103, 104]. These studies indicated that small proteins or short peptides can enter the cells. However, cell-penetrating peptides are limited in applications because of their lack of specificity to a particular cell [102]. Such limitation has led the scientists to search for new cell targeting/ internalizing peptides that can show specific binding affinity against a target cell.

These cell-targeting peptides which are specific to a particular cell can be uptaken into the cells through initial electrostatic interactions between their amino acids and plasma membrane components and internalized by endocytosis or energy independent methods [105]. RGD is one of the most extensively studied cell-targeting peptides [106] and its derivatives, such as galacto-RGD, have already been used in therapeutic assays [106]. Phage particles displaying cyclic peptide RGD4C can bind surface integrins and be effectively internalized into cells [107]. Recently, the heptapeptide LTVSPWY was also identified as a potential cell-targeting peptide against the ErbB2 receptor [108]. However, there is a need for more diverse repertoire of the cell-targeting and internalizing peptides that can help in diagnosis and treatment of breast cancer.

ErbB2 (also called HER2) is a very attractive target for cancer cell-specific detection and treatment because it's over expression may result in neoplastic transformation [109]. It is one of the four members of ErbB family receptors as described in chapter 1. Human ErbB2 is a large glycoprotein with 1234 amino acid residues. Like EGFR, the extracellular portion of human ErbB2 (1-632 residues) consists of four domains (I-IV) designated as L1, CR1, L2, and CR2 [110, 111]. ErbB2 acts as a major signal transducer following ligand-driven recruitment into heteromeric complex with other ErbB family members (such as ErbB1, ErbB3 and ErbB4), but it does not bind specifically to any known ligand of ErbB family [112]. Other members of ErbB family such as ErbB1, ErbB3 and ErbB4 can selectively bind to ligands such as epidermal growth factor (EGF), transforming growth factor α (TGF α), amphiregulin, β-cellulin,

epiregulin, epigen, heparin binding EGF and the neuregulins [109, 110, 111, 113]. The binding of these ligands and dimerization leads to the activation of tyrosine kinase domain and results in cellular signaling [114, 115]. Since human breast carcinoma SKBR-3 cells over express the ErbB2 receptor [109], it is a plausible target for cancer cell-targeting ligands. Development of the short peptide ligands that can specifically recognize the uniquely expressed proteins on cancer cells could facilitate the design of cell-targeting nanomedicines for cancer diagnosis and treatment.

Phage display has been demonstrated to be a powerful approach for the selection of short cell-targeting or internalizing ligands [116]. The principles and applications of phage display for studying protein-ligand interactions were reviewed elsewhere [23, 117]. To identify cell-binding peptides, a phage-displayed random peptide library is allowed to interact with target cells (in our case SKBR-3 cells), then the unbound phages are washed away and the bound phages are eluted by using an elution buffer [116]. The phage that is specifically internalized in the target cells during the selection process can be obtained by lysing the cells to release the cell-internalized phage.

One of the advantages of using phage display to select short cancer cell-targeting or internalizing peptides is that no prior information on the landscape of the cancer cells is needed before desired peptides are selected. Since the receptors over expressed on the cancer cells can be the preferred targeting sites for the phage-displayed peptides, we used human breast carcinoma cells SKBR-3 as a model, which are known to over express

ErbB2 receptors [118]. For selection of cell-binding and/or penetrating phages that can specifically target the SKBR-3 cells, we used landscape phage library – a multibillion collection of phages with random octamers fused to each copy of the major coat protein (called pVIII). The multivalent display of the binding peptides in the landscape phage dramatically increases the affinity of peptide-cell interaction because of avidity effect and increases a repertoire of selected binding clones [119]. Furthermore, the fusion pVIII protein comprises a dominant fraction (~95%) of viral mass and can be directly converted into specifically targeted drug- and gene-delivery vehicles [120, 121, 122]. The general strategy of the selection of cell-targeting/internalizing peptide by using a landscape phage library is outlined in Figure 2-1.

2.2 Experiments Performed

2.2.1. Landscape phage library and cells used

We used an 8-mer landscape phage display library (called f8/8) in our selection experiments. The detailed information about the library construction were described elsewhere [123]. Random peptides in this library are fused to N-terminus of the major coat protein pVIII of fd-tet bacteriophage, so that each landscape phage virion displays a unique 8-mer random peptide on each of the 3900 copies of pVIII. The human breast carcinoma SKBR-3 (HER-2 positive) cells were obtained from the American Type Culture Collection (ATCC, Rockville,MD). As a control we used normal breast MCF-10A (HER-2 negative) cells purchased from ATCC.

2.2.2. Mammalian cell culture

The target SKBR-3 cells and control MCF-10A cells obtained from ATCC were cultured in 25 cm^2 culture flask containing McCoys 5A modified medium and Dulbecco's modified Eagles medium (DMEM) respectively supplemented with 10% (v/v) fetal bovine serum, 11.2 μg/L penicillin, 11.2 μg/L stepromycin, and 11.2 μg/L ampicillin. The cells were incubated at 37^0C with 5% CO_2, and the cell culture medium was changed once in two days until the cells reached 90% confluence. The cells were harvested by 5 min incubation at 37^0C with a 0.25% trypsin, 1 mM EDTA solution followed by centrifugation at 2100 rpm for 5 min. The cell pellet was dissolved in 5 ml of medium and cell count was determined. The Phase contrast images of target SKBR-3 cells and control MCF-10A cells are shown in Figure 2-2.

2.2.3. Preparation of the bacterial host starved cells

A fresh loop of *E. Coli* K91 BlueKan cells was inoculated into three test tubes containing 2 ml NZY/Kanamycin (100 μg/ml) in each tube. The tubes were incubated in a shaking incubator at 220 rpm at 37^oC overnight. 300 μl of overnight cultures were transferred into a 250 ml flask containing 20 ml NZY medium. The flask was incubated at 220 rpm, 37^0 C until OD_{600} =0.45, followed by gently shaking (50 rpm) for additional 8 min. The cells in the sterile tube were then centrifuged at 2000g for 10 min at 4^oC. The supernatant was discarded and the cells were gently re-suspended in 20 ml of 80 mM NaCl solution. The re-suspended solution was then gently shaken at 50 rpm for 45 min,

followed by centrifugation as above. The cell pellet was re-suspended in 1 ml of cold sodium ammonium phosphate buffer (NAP buffer) (80 mM NaCl, 50mM NaH_4PO_4 pH=7.0 adjusted with NH_4OH) and stored in a refrigerator.

2.2.4. Affinity selection of SKBR-3 cell-binding phage clones

The affinity selection procedure as shown in Figure 2-1 was followed with a slight modification of a previously reported protocol described elsewhere [116]. Briefly, the landscape phage library (~$1x10^9$ phage virions) was first incubated with empty 25 cm^2 culture flask at 37^oC for 1 h to remove the phages that non-specifically bound to the culture flask. This process is known as depletion. The resultant depleted library was then used as an input library to the culture flask containing the control MCF-10A cells (HER-2 negative cells). This process is known as negative selection, which was performed to remove phage that binds to the receptors of healthy cells and increase a portion of the phage binding target SKBR-3 cancer cells. The depleted phage library was transferred to the flask with target SKBR-3 cancer cells (HER positive cells), and incubated at 37^oC for 1 h. The flask was washed 10 times with Bovine Serum Albumin (BSA)/Tween washing buffer to remove the unbound phages. The cell surface bound phages were eluted from the culture flask with 800 µl of low pH elution buffer (0.1N HCl, 1mg/ml BSA and pH adjusted to 2.2 with glycine) for 10 min. The eluate was transferred into a 1.5 ml eppendorf tube and neutralized by mixing it with 150 µl of 1 M Tris-HCl (pH= 9.1) immediately. At the same time, the cell internalized phages were recovered using a cell

lysis buffer (2% sodiumdeoxycholate, 10 mM Tris, 2 mM EDTA, pH 8.0).The tubes were stored at 4^0C for further use.

2.2.5. Amplification of eluates

The entire first-round eluate (950 µl) was concentrated to reach a final volume of 150 µl by using a Centricon 100-KDa Ultrafilter (Amicon). 150 µl of concentrated eluate was added to 150 µl of the starved cells and incubated for 15 min at room temperature. The phage-infected cells were transferred to 40 ml of NZY medium with tetracycline (0.2 µg/ml) in a 125 ml flask and incubated for 45 min at 37^{o}C with shaking. The tetracycline concentration was increased to 20 µg/ml and the shaking of the flask was continued at 37^{o}C for 16-24 h.

2.2.6. Amplification of cell lysate fraction

The SKBR-3 cell-internalized phage clones were recovered using the cell lysis buffer (2% sodiumdeoxycholate, 10 mM Tris, 2 mM EDTA, pH 8.0). In order to recover internalized phages, the cell monolayer from the cell culture flask was scraped with a sterile pasture pipette and taken into 5 ml of cell culture medium and centrifuged at 130 g for 10 min. Later, the supernatant was removed and 200 µl of the cell lysis buffer was added to the pellet. The fraction was stored at 4^{o}C until amplification. The phages were used for amplification and further selection as stated above.

2.2.7. Purification of amplified phages by using double PEG precipitation

Phage was purified by double polyethylene glycol (PEG) precipitation as described previously [124]. Briefly, 40 ml of NZY medium containing 20 µg/ml tetracycline was inoculated with a fresh single colony of phage-infected cells in a 250 ml flask. The culture was incubated in a shaking-incubator at 200 rpm, 37^{o}C overnight. The overnight culture was poured into a 250 ml Beckman centrifuge bottle and centrifuged at 3000 g for 10 min at 4^{o}C. The supernatant was then poured into a fresh tube and centrifuged at 9300 rpm for 10 min at 4^{o}C. The resultant cleared supernatant was again poured into a fresh tube, to which 6 ml PEG/NaCl solution (100 g PEG 8000, 116.9 g NaCl and 475 ml water) was then added. The tube was kept at 4^{0}C overnight for phage precipitation. The precipitated phages were collected by centrifugation at 13000 rpm for 60 min and the supernatant was removed. The pellet was then dissolved in 1 ml Tris buffered saline (TBS) in a micro-centrifuge tube and centrifuged again at 13000 rpm for 10 min to remove any undissolved material. 150 µl of the PEG/NaCl solution was added to the supernatant which was then kept on ice overnight. The tube was then centrifuged at 13000 rpm at 4^{o}C for 60 min and the supernatant was removed. The final pellet was dissolved in 200 µl TBS and vortexed thoroughly.

2.2.8. Titering of phage

Serial dilutions (10^{-2} -10^{-8}) were prepared by using TBS (pH 7.4). For example, a 10^{-2} dilution was reached by taking 10 µl of phage in 490 µl of TBS and 500 µl of sterilized water. In a 1.5 ml eppendorf tube 10 µl of starved cells were mixed with 10 µl of each phage dilution and incubated for 15 min at room temperature. 180 µl NZY with tetracycline (0.2 µg/ml) was added to each tube and the tube was incubated for 45 min at 37^{o} C. Suspensions from the tubes were spread onto NZY plates with tetracycline (20 µg/ml). The plates were incubated overnight at 37^{o} C in an incubator and the number of colonies on the plates was counted the following day. The phage titer was calculated as follows:

Titer = N X 100 X dilution factor, where N= number of colonies formed

2.2.9. Second- fourth rounds of affinity selection

The purified phage after each round was used as an input library for the next round of selection (Figure 2-1), which proceeded similar to the first round described. After the fourth round of selection, the eluted as well as lysate phages were not amplified. Instead, they were titered and 65 random colonies were picked up for sequencing in order to determine the SKBR-3-binding peptides that were fused to the major coat protein pVIII of the selected phages.

2.2.10. Sequencing of selected phage colonies

Each colony of phage infected *E. Coli* K91 BlueKan cells on the plates was inoculated into a tube containing 2 ml NZY/Tetracycline (20 μg/ml) and the tubes were kept in the shaking incubator at 220 rpm, 37^{o} C overnight. 1 ml culture from each tube of phage infected K91 BlueKan cells and 30 μl of 830 μM related primer (5' – CAAAGCCTCCGTAGCCGTTG-3') were sent to MC Lab Inc. for sequencing. The nucleic acid sequences of the insert-coding region of the phage DNA were translated to the corresponding peptide sequences using EB1 tool Transeq.

2.2.11. Phage capture ELISA on target SKBR-3 cells

Phages that specifically interact with the SKBR-3 cells due to the presence of specific peptides fused to the major coat protein were revealed using phage capture ELISA. The target cells (SKBR-3) and control cells (MCF-10A) (~1 x10^4 cells/well) were applied to a 24 well plate and incubated at 37^{0}C overnight. All the wells were blocked with 100 μl of 0.1% bovine serum albumin (BSA) and incubated at room temperature for 1 h. Later each well was washed five times with 200 μl of TBS containing 0.5% Tween 20, and 50 μl (1x10^{10} virions/ml) of purified phage preparation was applied to SKBR-3 cell-coated wells, MCF-10A cell-coated wells and an empty well, which were then incubated at room temperature for 1h with gentle mixing. After incubation the plates were washed with 200 μl of TBS buffer and supplemented with 40 μl of anti-fd bacteriophage IgG. The plates were then incubated at room temperature for 1

h, washed with TBS buffer and incubated with 40 µl of anti rabbit IgG conjugated with alkaline phosphatase at room temperature for 1 h. After a final washing step, alkaline phosphatase substrate, *p*-nitrophenyl phosphate, was added to the wells and the absorbance was measured at 405 nm using a plate reader. The *p*-nitrophenyl phosphate is a substrate, which turns yellow when cleaved by alkaline phosphatase. A relative amount of phage bound to the cells was determined by measuring the rate of color change in each well.

2.2.12. Immunofluorescence studies of phage-cell interactions

The SKBR-3 cells were cultured on a cover slip in a six well plate. Two days after seeding, the medium was removed and the cells were incubated in serum-free medium for 1 h. Later, the serum free medium was removed and approximately $1x10^9$ phages in TBS were added to the chamber and incubated at 37^0 C for 1 h. The cells were washed three times with PBS and fixed in 4% formaldehyde in PBS for 15 min. The fixed cells were washed three times in PBS and incubated for 1 h in room temperature with 1:10 dilution of Alexa Fluor conjugated anti–pIII antibody. The detailed procedure for conjugation of dye and antibody and purification of dye-conjugated antiboby from free dye can be obtained from Invitrogen Alexa Fluor® 488 Monoclonal antibody labeling Kits (cat# A-20181). The cover slips were washed 5 times with PBS and then incubated with DAPI, a nuclear staining dye, for 5 min. The cover slips were again washed for 5 more times with PBS and mounted on a microscope slide. The cells were examined using a Zeiss

Universal epiflourescence microscope equipped with Olympus oil immersion DApo UV objectives. Digital images of cells were collected using Olympus DP-70 camera and software.

2.2.13. Energy dependent mechanism of phage entry

In order to determine the energy-dependency of phage entry, SKBR-3 cells were incubated with phage clone, labeled with rhodamine B at either 37^{o}C (in presence and absence of inhibitors) or 4^{o}C. Briefly, rhodamine B labeling of engineered phages was performed by mixing 0.2 g of a coupling agent, 1-[3-(Dimethylamino)propyl]-3-ethylcarbodiimide hydrochloride (EDC), and 2.5 mg of rhodamine B in 10 mL of affinity selected phage stock solution (1x10^{12} pfu) in phosphate buffer (pH 5.6). This procedure results in the attachment of the dye through EDC assisted caging. The rhodamine-labeled phages were extensively dialyzed for 3 days under stirring to remove unbound dye molecules. The modified phages were stored at 4^{o}C in dark until further use. SKBR-3 cells were seeded 48 h prior to phage incubation on cover glasses in the six-well plates (8000 cells/well). The growth medium was replaced with 200 µl of rhodamine conjugated phage in PBS (1x10^{9} cfu/ml), and cells were incubated for 1 h, either at 37^{o}C (in the absence and presence of ATP inhibitors) or at 4^{o}C (all the solutions were prechilled to 4^{o}C). Later the cells were extensively washed three times with PBS at corresponding temperature and fixed in 4% paraformaldehyde in PBS for 15 min at 37^{o}C. After incubation the cells were washed twice with PBS and stained with 250 µl of DAPI (1

μg/ml) for 5 min, the cover slips were again washed for 5 more times with PBS and mounted on a microscope slide. The cells were examined under Zeiss Universal epiflourescence microscope equipped with Olympus oil immersion DApo UV objectives. Digital images of cells were collected using Olympus DP-70 camera and software.

2.2.14. Quantification of cell associated phage on target and control cell lines

The specificity was determined by comparing the selected phage binding to a control wild type phage (f8-5 vector without any foreign insert) on target SKBR-3 cells. To test the selectivity, L1 phage was incubated with target SKBR-3 cells and other control cell lines. Controls used in this study are MCF-10A cells obtained from ATCC, Fibroblasts, Mesenchymal stem cells (MSCs), and Squamous cell carcinoma (SCC-15) (sourced from Cell Culture Core facility at BWH Dermatology/Harvard Skin Disease Research Center, Harvard Institutes of Medicine, and USA). All the cells are cultured at 37°C in a humidified sterile atmosphere of 95% air and 5% CO_2, using recommended procedures. Once the cells reached 90% confluence, the target and control cells were incubated with 1x 10^9 pfu/ml of L1 phage in blocking buffer for 1h at 37^0C. Before, the additions of phage, the cells are first incubated with serum free medium for 1h at 37^0C. The phage bound to the target and control cells were isolated using elution and lysis buffer as stated before. The phage titers were obtained by bacterial infection of recovered phage and represented as output to input phage. All experiments were done in triplicates.

2.2.15. Blocking of L1 phage uptake by 12 mer synthetic peptide

Target SKBR-3 cells were cultured in 25cm^2 tissue culture flask and incubated with 2 ml of VSSTQDFPDPAK synthetic peptide (Neopeptide, Cambridge, Massachusetts) in Mc Coy's 5A medium at concentration 0.25mM, 0.75mM and 1.25mM. These concentrations of synthetic peptide were incubated with the SKBR-3 cells for 1hr at 4^{0}C as previously described. [125] After incubation, 1x10^9 cfu of L1 phage in 1ml of blocking buffer was added to the cells and incubated for 1 h at 37^{0}C. Unbound phage was removed using sterile pasteur pipette and the cells were thoroughly washed five times for 5 min each with cold washing buffer. The phage associated with cells in presence of synthetic peptide was recovered with lysis buffer as described above. The amount of phage bound was quantified using titration method.

2.2.16 Live cell imaging of landscape phage treated SKBR-3 cells using video microscopy

SKBR-3 cells cultured on 25-mm cover glasses were transferred to a perfusion filming chamber. The chamber was placed on Zeiss Standard microscope stage maintained at 37°C with an air curtain incubator. The cell images were recorded with Hamamatsu C2400 camera and Scion software. Cells were recorded for 15 min in McCoy's 5a medium and then 1x10^9 cfu/ ml selected phage was perfused into the chamber from a 2.5-cc syringe driven by a syringe pump (Sage model 341 A) and recorded for additional 45 min.

2.2.17 Immunofluorescence of labeled F-actin with phage internalization

The SKBR-3 cells were cultured on the cover glasses in a six well plate. Two days after seeding, the medium was removed and the cells were incubated in serum-free medium for 2 h. The medium was removed and 200 μL of phage suspension (approximately $1x10^9$ virions/ml in TBS) in cell culture medium was added to each well and incubated at 37^0 C for 15 min, 30 min, and 45 min respectively. The cells were washed three times with D-PBS and fixed in 4% paraformaldehyde in D-PBS for 15 min. The fixed cells were washed three times in D-PBS and incubated with 2 μM rhodamine-phalloidin in D-PBS for 15 min in dark at room temperature. The cover glasses were washed 5 times with D-PBS and mounted on a microscope slide. The cells were examined using an Olympus fluoview FV 500 confocal laser scanning microscope and the images were acquired at constant PMT, gain, offset, magnification (60 x objectives) and resolution.

2.2.18 Statistical analysis

All the statistical analyses were performed using student unpaired two-sided t-test analysis as stated before [126]. P values were considered to be statistically significant with $p \leq 0.0002$.

2.2.19 Preparation of Cross-Linked L1 Phage

L1 phage was cross-linked to dextran polymer as reported by Smith et.al. [127] and Samaoylova et. al. [128]. In this procedure 1 ml of L1 phage (1.6×10^{13} virions/mL) in coupling buffer was mixed with 10 μL of N-hydroxysuccinimide-dextran (NHS-dextran; a water-soluble multifunctional dextran polymer custom-synthesized by CarboMer, Westborough, MA, USA) in a 1.5 ml eppendorf tube. The mixture was vortexed and 150 μL of 50% PEG in water is added immediately. The reaction mixture was incubated under shaking for overnight at room temperature. The following day, the solution was transferred to 15ml centrifuge tube and the unreacted N-hydroxysuccinimide (NHS) groups were quenched by the addition of 8 mL of 1 M Tris-HCl, pH 9.5, and 890 μL 5 M NaCl. The resulting mixture is kept under shaking for an additional 1–2 h at room temperature. The cross-linked phage was pelleted by centrifugation (12,000× g) for 15 min, washed thoroughly and the final pellet of cross-linked phage is suspended in 1ml of TBS. The concentration of the cross-linked phage was determined spectrophotometrically and solution is stored at 4^{o}C until further use.

2.2.20 Isolation and analysis of SKBR-3 cell lysate using Cross-Linked L1 Phage

SKBR-3 cells were cultured in six 25 cm^2 flasks till they reached 90% confluence. The medium was removed, and the cells were rinsed with ice-cold PBS buffer. The cells were lysed in cell lysis buffer (purchased from Sigma) with protease inhibitor cocktail (Sigma) for 15 min at 37°C. In one flask, intact SKBR-3 cells were biotinylated with the EZ-Link Sulfo-

NHS-LC-LC Biotin (Pierce, Rockford, IL, USA) prior to cell lysis. All the lysates were centrifuged and the supernatant was used for the isolation of SKBR-3 cell membrane proteins. Later, the lysate fractions were incubated with cross-linked LI phage (10^{13} virions) under shaking for overnight at 4°C. Finally, the cross-linked phage with cell components was pelleted at 20,000× g for 15 min at 4°C. At the end cell components bound to the phage was eluted with 200 µL of elution buffer (0.1% BSA, 0.2 M glycine-HCl, pH 2.2) for 15 min at 4°C. The phage matrix was separated from eluate by centrifugation for 10 min at 13000 rpm. The eluate was transferred to a fresh microcentrifuge tube and neutralized with 37.5 µL of 1 M Tris-HCl, pH 9.0. Finally, the cell lysate, clarified cell lysate, biotinylated SKBR-3 cell lysate, and proteins isolated through L1 phage matrix fractions were separated by 12% sodium dodecyl sulfate- polyacrylamide gel electrophoresis (SDS-PAGE) and protein isolated was further analyzed using N-terminal protein sequencing and mass spectrophometer analysis.

2.3 Results

2.3.1 Selection of cell targeting/internalizing phage against SKBR-3 cells

Phage clones that bound to SKBR-3 cells were selected from the landscape phage library f8/8 [123] through successive rounds of affinity selection procedure, in which the phage library was incubated with SKBR-3 cells cultured in a 25 cm^2 tissue culture flask (as shown in Figure 2-1). During the affinity selection process, the unbound phages were

washed away and the cell surface bound phages were eluted with mild acid treatment. It should be noted that phage library was allowed to interact with normal breast cells first in order to get rid of phages that might bind to normal cells before interacting with breast cancer cells. During each round of affinity selection, after cell-surface-bound phages were eluted, the cells were lysed to release the cell-internalized phages to obtain cell-internalizing peptides. The cell-internalized phages were recovered from cell lysates. Phages that bound to SKBR-3 breast cancer cell surface and internalized in the initial selection procedure were amplified separately by infecting bacteria and used as the input for the next round of affinity selection. This procedure was repeated four times. After the fourth round of affinity selection, 65 clones were randomly picked from both the eluate and lysate fraction and a segment of genomic DNA encoding the octapeptide (i.e., insert-coding region) was sequenced. The cell-surface-targeting peptides (denoted as S) and cell-internalizing peptides (denoted as L) and their frequencies were shown in Table 2-1a and Table 2-1b, respectively. A comparison between them indicates that two peptides (DGSIPWST and VSSTQDFP) are both surface-targeting and cell-internalizing.

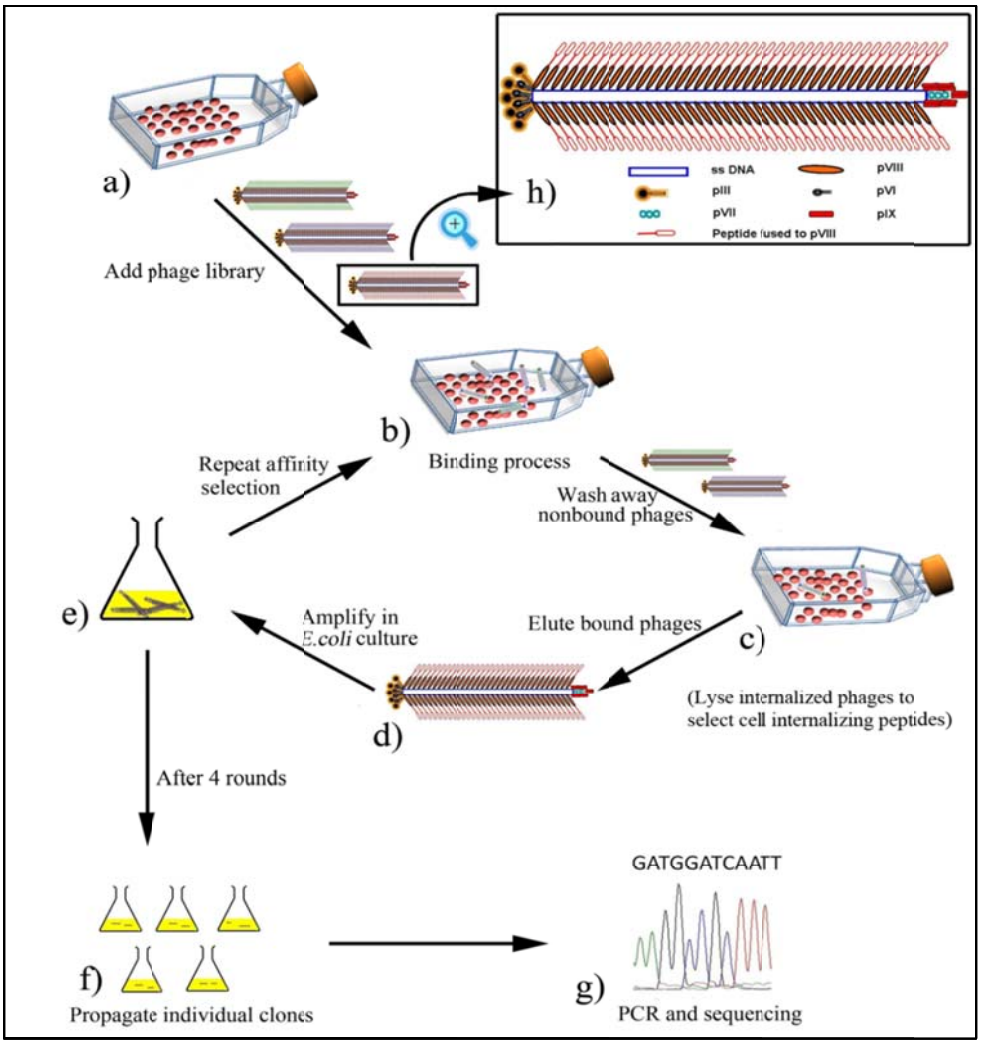

Figure 2-1: Illustration of the procedure of selecting cancer cell-targeting/internalizing peptides from a landscape phage library (affinity selection). (a) The SKBR-3 breast cancer cells are cultured in 25 cm^2 flask. (b) Some phages bind the cancer cells while some don't after a landscape phage library is added to the cancer cells. (c) Non-binding phages are washed away and the cell-binding phages still bind to the cells in the flask. (d) The cell-specific phage is eluted from the flask by using an

elution buffer. (e) The eluted phage is amplified by infecting bacteria *E. Coli*. (f) Amplified phage clones are propagated by PEG/NaCl precipitation and re-dissolved in TBS buffer (pH 7.0). (g) Part of phage genome (insert-coding region) is amplified by PCR and sequenced. (h) Scheme of a single phage particle, which shows that 5 copies each of pIII and pVI are at one end and 5 copies each of pVII and pIX are at the other end of phage whereas ~3900 copies of pVIII, form a protein coat wrapping single-stranded DNA. The foreign peptide is inserted in the solvent-exposed end of pVIII. To identify a cell-internalizing peptide, the procedure is same as above except that after Step (c), the cancer cells are lysed by using a cell lysis buffer to release the cell-internalized phage, which is followed by step (e) figure obtained with permission [129].

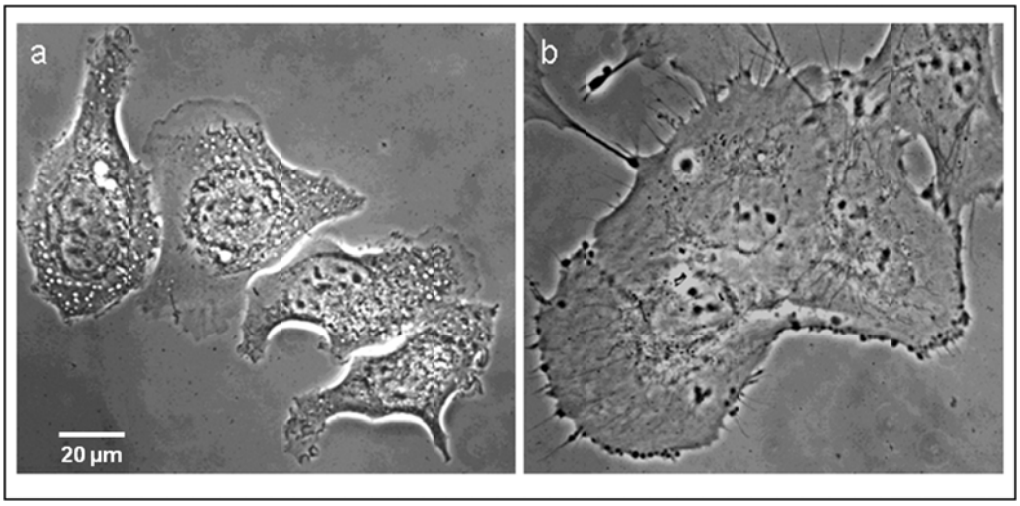

Figure 2-2: Phase contrast images of cells used for affinity selection a) SKBR-3 breast cancer cells and b) MCF-10A normal breast cells (Magnification 63x from objectives) figure obtained with permission from Ref [130].

Table 2-1a: **New SKBR-3 cell targeting peptide clones recovered from landscape phage library by using an elution buffer.** S: denotes cell surface binding fraction

Cell-Targeting clones		
Clone ID	Motif sequence	Frequency
S1	DGSIPWST	13
S2	VSSTQDFP	10
S3	DNGSGISW	5
S4	DTKTAPAW	3
S5	GSTDSDLK	2
S6	ATTAPSYP	1
S7	AAATKSDL	1

Table 2-1b: New SKBR-3 cell internalizing peptide clones recovered from landscape phage library by using a lysis buffer. L: denotes cell internalizing fraction. Table obtained with permission from Ref [39].

New Cell-internalizing clones		
Clone ID	Motif sequence	Frequency
L1	VSSTQDFP	13
L2	DGSIPWST	8
L3	AFSEAAQT	5
L4	ADAPSNGW	1
L5	DNDNYAFP	1
L6	DYADYSDL	1
L7	AADYDPLA	1

2.3.2 Characterization of selected peptides and phages:

Selected peptides were analyzed using the REceptor Ligand Contacts (RELIC) program, which is a bioinformatics tool for combinatorial peptide analysis and identification of protein-ligand interaction sites [131]. A complete review of RELIC and

its principle and application in analyzing affinity selected peptides can be found in the literature [131]. We used two RELIC programs (RELIC/POPDIV and RELIC/INFO) to analyze the binding affinity of our selected peptides towards SKBR-3 cancer cells. RELIC/POPDIV program uses a statistical sampling method to estimate the sequence diversity of a combinatorial peptide library based on the sequence obtained from a limited number of randomly sampled members of the library. According to this program, affinity selected peptides towards target SKBR-3 cells should have a less diversity than an equivalent number of randomly selected peptides from the native library. It has been demonstrated that the decrease in the diversity of the sequences obtained from successive rounds of selection is an indicator of affinity selection [132, 133, 134].

We calculated the diversities of both affinity selected peptides and random peptides from the native library by using RELIC/POPDIV program. Our affinity selected peptides yielded a diversity value of 0.00402 whereas the same number of randomly selected peptides from a native library yielded a diversity value of 0.00913**.** Compared to randomly selected peptides, our affinity selected peptides have a less diversified population, which is a clear evidence for successful selection of peptides with binding affinity towards SKBR-3 cells.

In order to verify that the selected peptides were from affinity selection and not from amplification noise, we used RELIC/INFO program because the noise from amplification has regular and measurable patterns [133, 134]. This program was designed to initially calculate the noise pattern and then subtract the noise pattern from

the affinity pattern to obtain information content [131]. Information content is defined as $-\ln(P_N)$, where P_N is the probability of randomly finding a given peptide. The principle of RELIC/INFO helps in determining the occurrence of information content of the affinity selected peptides and thereby confirms the binding affinity of selected peptides after affinity selection. A larger information content ($-\ln P_N$) of a peptide indicates a greater chance of observing this peptide in affinity selection due to specific binding to the target. Indeed, from Figure 2-3 the normalized distribution of the information content for our SKBR-3 selected peptides is positively shifted towards higher information content in comparison to that of the peptides selected from native phage library. This positive shift of red curve in Figure 2-3 suggests that our SKBR-3-selected peptides results from affinity selection. Both observed result are in accordance with the principle of RELIC/POPDIV and RELIC/INFO [131].

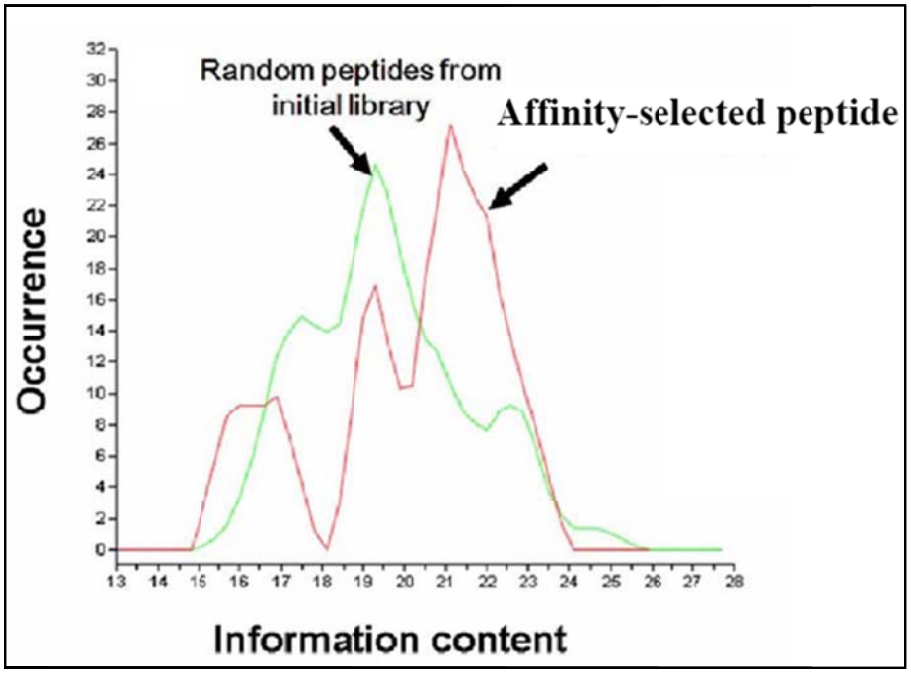

Figure 2-3: **Relative abundances of peptides plotted as a function of information content for peptides selected to SKBR-3 (RELIC/INFO analysis) [39].**

Phage capture ELISA shows that the selected cell-targeting phage has high specificity against SKBR-3 cells (Figure 2-4). Immunoflourescence studies (indirect labeling phage with green dye Alexa Fluor 488 through using anti-pIII phage antibody) confirms wild type fd phage cannot bind to SKBR-3 cells and L1 phage binds to SKBR-3 cells in the absence of synthetic peptide (as shown in Figure 2-5). However, L1 phage cannot enter the SKBR-3 cells in the presence of synthetic peptide. Figure 2-5 shows that the cell-targeting phage is labeled with alexa fluor dye and the cell nuclei are

counterstained with DAPI. These results confirm that the identified cell-targeting phage can recognize SKBR-3 cells and be internalized by the SKBR-3 cells due to the presence of the cell-internalizing sequence (VSSTQDFP) displayed on the major coat of the phage.

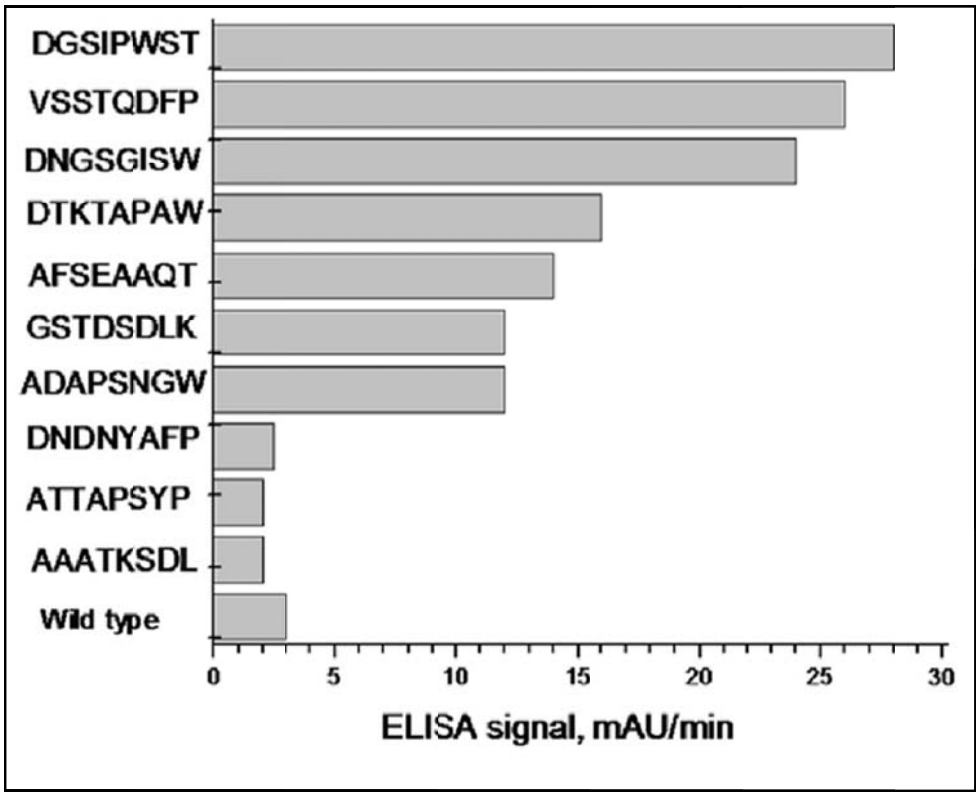

Figure 2-4: Binding of control phage and affinity selected phages to SKBR-3 cells immobilized on a microtiter plate (ELISA). X axis indicates the ELISA signal in milliabsorbance units (mAU)/min and Y axis shows the affinity selected peptide sequences displayed on the major coat of fd-tet phage figure obtained with permission from Ref [39] .

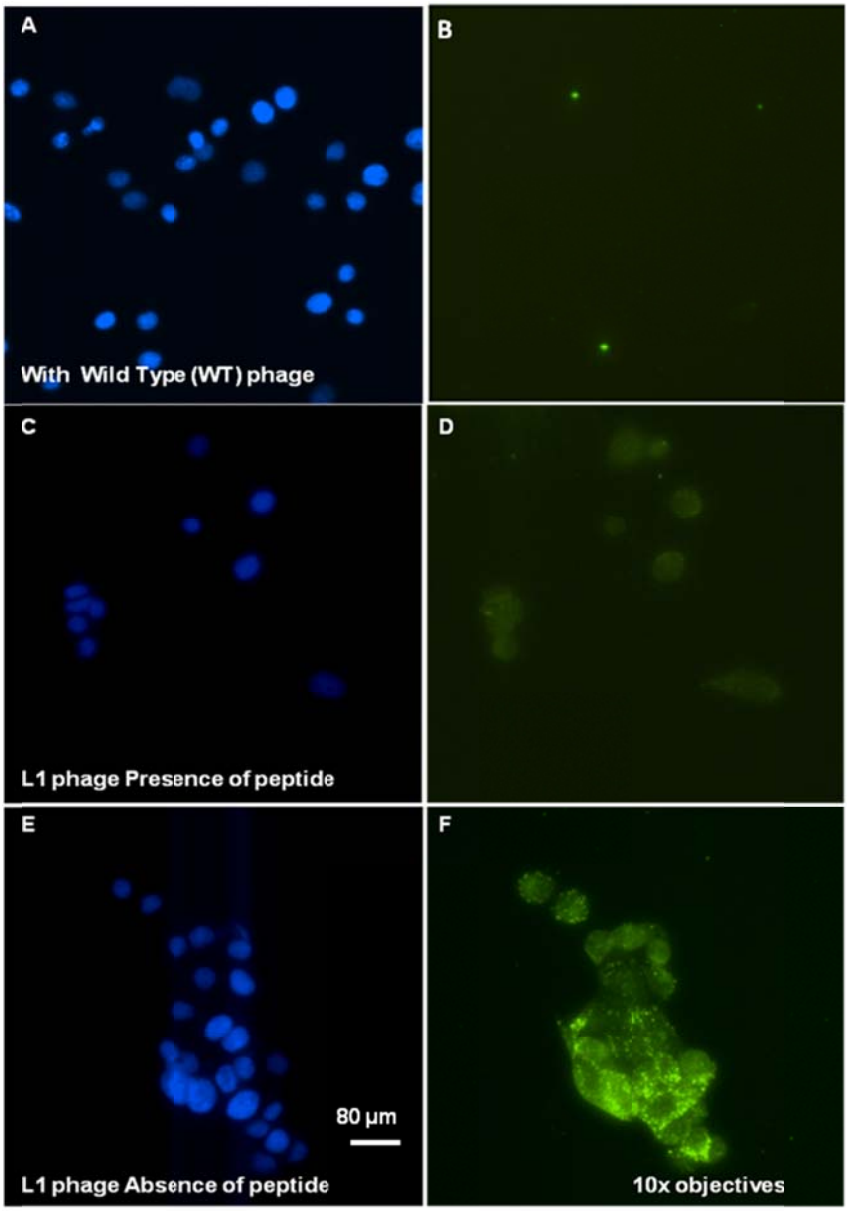

Figure 2- 5: Detection of phage binding to SKBR-3 cells in the absence and presence of peptide inhibitor using immune fluorescence microscopy. (A) DAPI-stained cells with treatment with wild type fd-tet phage, showing fluorescence associated with nuclei. (B) SKBR-3 cells treated with wild type fd-tet phage and labeled with anti-phage

antibody conjugated to Alexa Flour (No fluorescence indicates WT phage is not binding). (C, D) Cells treated with identified cell-internalizing phage (displaying peptide L1) and stained with DAPI and anti-phage antibody-labeled Alexa fluor fluorescently, showing the corresponding blue fluorescence from nuclei and green fluorescence resulting from the internalization of phage. (E, F) Cells treated with identified cell-internalizing phage in presence and stained with DAPI and anti-phage antibody-Alexa fluor.

To see the motif similarities between peptide inserts from selected phages and natural ligands binding to ErbB family receptors, we used RELIC/MATCH program to align our selected peptide sequences with the sequences of the proteins that were reported to recognize SKBR-3 cells. The alignment results are shown in Table 2-2 and 2-3 and suggest that our selected peptides show similarity with some domains on the proteins, which are known to recognize SKBR3 cells, including antibodies.

Table 2-2: Alignments of selected peptides with known ErbB family binding proteins (Red denotes same amino acids and Yellow denotes amino acids with similar properties).

Ligand	Receptor	Pair wise alignment	Phage clone/s
Epidermal growth factor (EGF)	EGFR (ErbB1)	25 LEEKKGKGVSRRLPRR 41 DNGSGISW	S3
Amphiregulin (AP)	EGFR (ErbB1)	56 EMSSGSEISPVSEMPS 71 DNGSGISW 26 GLDLNDTYSGKREPFS 41 DNDNYAFP	S3,L5
Neuregulin-1 (NRG)	ErbB3 and ErbB4	181 FSFLPSTAPSFPSPTR 196 DTKTAPAW ATTAPSYP	S4,S6
B-Cellulin	ErbB1 and ErbB4	1 MDPTAPGSSVSSLPLLL 17 DNGSGISW	S3
Heregulin	ErbB3	11 GKGKKKERGSGKKPESA 27 DNGSGISW 43 KSQESAAGSKLVLRCET 59 AAATKSDL	S3, S7
Epigen	ErbB1	14 NAMTALTEEAAVTVTPP 30 AFSEAAQT	L3

Table 2-3: Alignments of selected peptides with known anti ErbB2/Her2 proteins in humans (Red denotes same amino acids and Yellow denotes amino acids with similar properties).

Antibody	Receptor	Pair wise alignment	Phage clone/s
Anti-ErbB2 Fab2c4	ErbB2	LVTVSSASTKQPSVFPLAPSSKSTSGG AAATKSDL	S7
Anti-ErbB2 antigen binding region	ErbB2	GSKLEIKGSTSGSGKSSEGKQVQLQE DNGSGISW	S3
Antigen binding domains Anti-P185-Her2	ErbB2	TITCRASQDVNTAVAWYQQKPGKAP DTKTAPAW	S4

2.3.3 Mechanism of phage entry into target SKBR-3 cells.

In order to understand the mechanism of phage entry into SKBR-3 cells, initial experiments were conducted to determine the energy dependency of L1 phage uptake because endocytosis can be strongly inhibited by lowering the temperature [135]. For this purpose, selected phages were labeled with rhodamine as described earlier [136]. Phages conjugated to rhodamine were then incubated with SKBR-3 cells at 37^{o}C (in the absence of ATP inhibitors), at 4^{o}C and at 37^{o}C (in the presence of ATP inhibitors, sucrose and sodium azide). As shown in Figure 2-6, the phage uptake is only active at 37^{o}C in the absence of inhibitors. In contrast, lowering the temperature completely or in the presence of inhibitors reduced the phage uptake as shown in Figure 2-6 (D-I). The phage internalization efficiency was found to be less than 5% at 4^{o}C and in the presence of inhibitors as compared to phage internalization efficiency at 37^{o}C. These findings confirm that selected L1 phage enters the SKBR-3 cells by energy-dependent uptake mechanism.

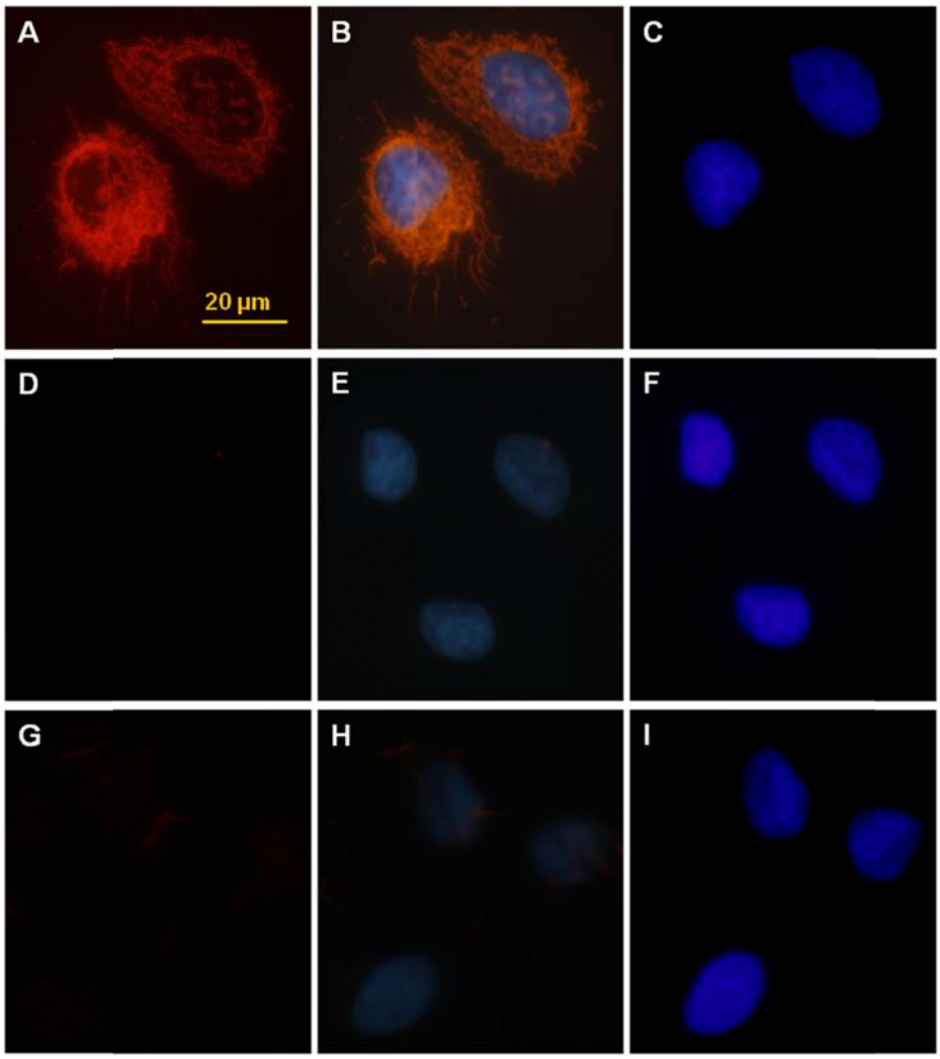

Figure 2-6. Detection of energy dependency of L1 phage entry in SKBR-3 cells using immune fluorescence (A-C) Rhodamine and DAPI fluorescence at 37^{o}C in absence of ATP inhibitors. (D-F) Rhodamine and DAPI fluorescence at 4^{o}C and (G-I) Rhodamine and DAPI flourescence at 37^{o}C in presence of ATP inhibitors (sucrose and sodium

azide). [A,D,G-rhodamine specific filter; B,E,H- rhodamine and DAPI specific filters; C,F,I- DAPI specific filter. Figure obtained with permission from Ref [129]

2.3.4 Competitive binding studies using synthetic peptide.

SKBR-3 cell internalizing phage clone, L1 bears VSSTQDFP peptide sequence on its N-terminus. In order to test whether L1 phage internalization takes place through a VSSTQDFP recognition motif, we performed competitive assay using a synthetic VSSTQDFPDPAK peptide. As described in earlier section, synthetic peptide was incubated with the cells prior to the incubation of L1 phage. Figure 2-7 shows that incubation of synthetic peptide reduced the L1 phage binding to the SKBR-3 cells in a concentration dependent manner. As the concentration of peptide is increased less number of L1 phage was bound to the cells. This confirms that L1 phage internalization is competitively inhibited in presence of synthetic peptide.

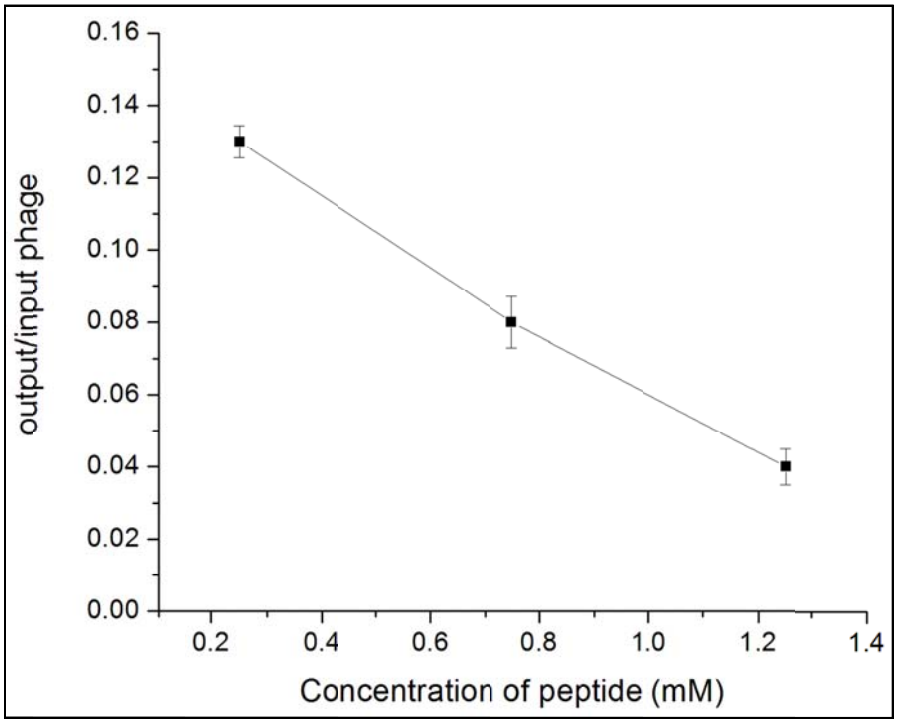

Figure 2-7. Blocking of L1 phage binding to SKBR-3 cells in presence of VSSTQDFPDPAK synthetic peptide. SKBR-3 cells were incubated with different concentrations of the VSSTQDFPDPAK peptide followed by L1 phage incubation. Phage bound to the cells was quantified via titering and is presented here as an output to input ratio (y-axis) versus peptide concentration (x-axis). Data presented here is mean of three independent experiments (±sd) figure obtained with permission from Ref [39].

2.3.5 Actin dynamics during the phage internalization into SKBR-3 cells:

In order to understand the mechanism of selected phage internalization into SKBR-3 cells, we first performed video microscopy to observe the behavior of SKBR-3 cells before and after the treatment of cells with internalizing phage (L1). SKBR-3 cells are polygonal cells and display cycles of protrusions and withdrawals of small lamellipodia at the cell edges forming small ruffles at random places around their periphery. The dorsal (upper) cell surface is relatively quiescent, with occasional small ruffles (Figure 2-8 a-c). After injection of internalizing phage into the filming chamber, SKBR-3 cells showed very intense ruffling in multiple places around the cell periphery. Cells were also rapidly forming numerous ruffles on their dorsal surfaces. As shown in Figure 2-8 d-f, cell edges and dorsal surface stay very active over the entire time of recording (45 min). In the control, no significant changes were observed in the behavior of cells before and after the addition of control wild type phage Figure 2-9 a-f. The representative still images of SKBR-3 cells before and after the addition of selected phage and WT phage are shown in Figures 2-8 and 2-9. The original videos clearly demonstrate that there are significant changes in the cell behavior in regard to activity of cell edges and dorsal surface during and after the internalizing phage entry into SKBR-3 cells. It is well established that formation of protrusions in a variety of cells is associated with dynamic changes in cortical actin.

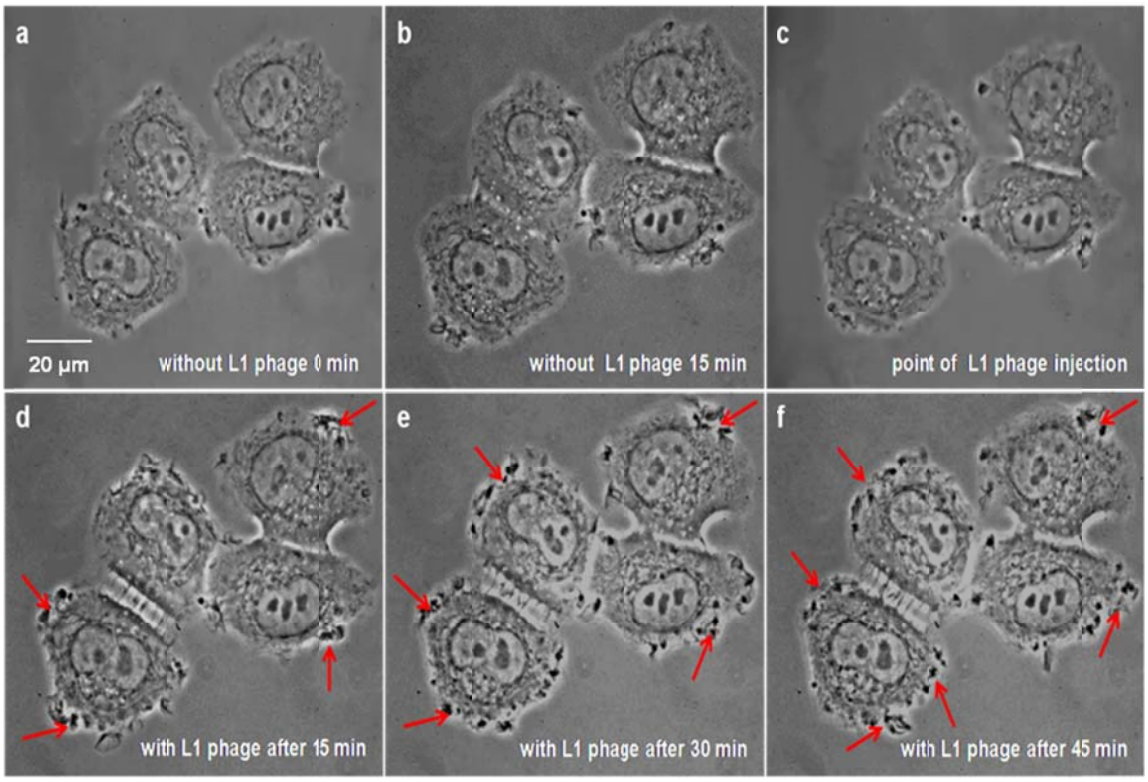

Figure 2-8: Live SKBR-3 cells recorded using digital video microscopy in the presence of selected SKBR-3 cell internalizing phage (L1): **(**a-c) before and (d-f) after phage injection. Red arrows indicate some areas of increased ruffling at the cell edges in the presence of internalizing phage figure obtained with permission from Ref [39].

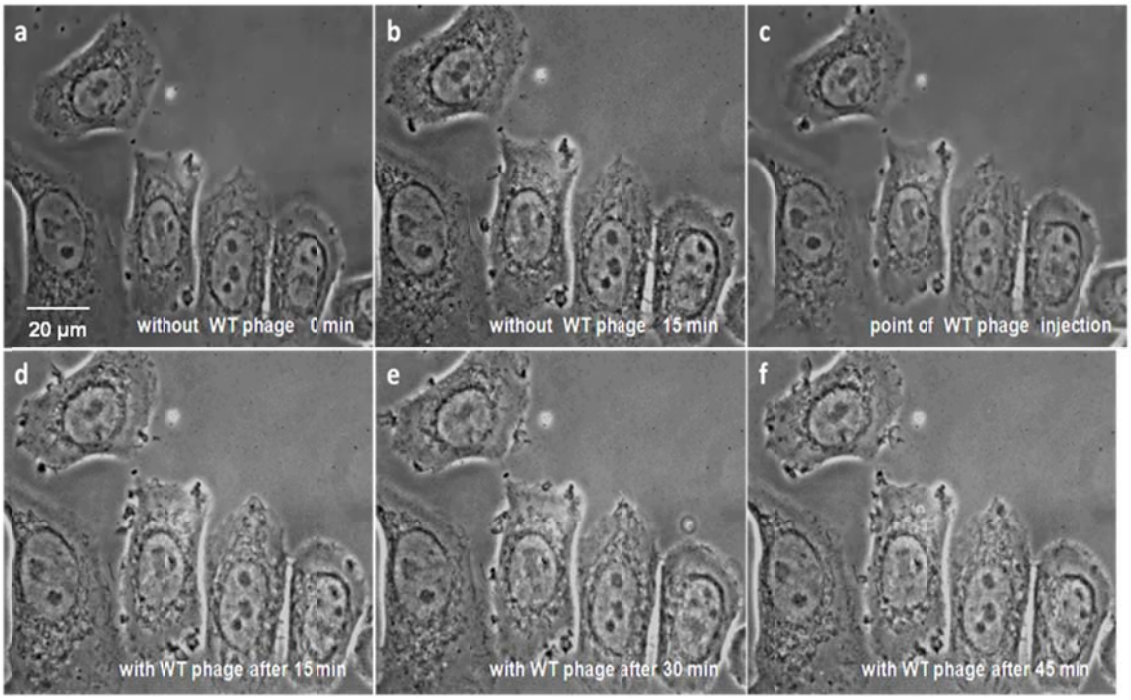

Figure 2-9: Live SKBR-3 cells recorded using digital video microscopy in the presence of control wild type fd-tet phage (a-c) before and (d-f) phage injection. There was essentially no cell response to the presence of the wild type phage in the environment figure obtained with permission from Ref [39].

In order to better understand the involvement of actin cytoskeleton in phage internalization, we labeled F-actin with rhodamine-conjugated phalloidin and examined actin distribution using confocal imaging. SKBR-3 cells were treated with cell internalizing phage for 15, 30 and 45 minutes and immediately after incubation, were fixed and labeled with rhodamine-phallodin. All fluorescence images were obtained at

constant PMT, gain and offset. Figure 2-10 shows the fluorescence images of labeled F-actin in SKBR-3 cells incubated with phage and fixed at different time points as stated above. F-actin in control, untreated cells was most diffusely distributed throughout the cell, and also thin bundles of filaments and occasional brighter granular structures were present. After 15 min incubation with internalizing phage, the bright granular structures and diffuse staining greatly diminished and thin actin bundles stain less intensely. At 30 and 45 min of incubation, small disperse granular structures became brighter and clearly visible all over the cells, while thin filament bundles were still less visible than in untreated cells. The F-actin was further quantified using fluorescence microplate reader. For all the quantitative measurements, a constant number of cells ($1x10^4$) were placed in all the wells, treated with phage and labeled with rhodamine-phallodin. For fluorescence measurements, the rhodamine was excited at 560 nm and the emission was collected between 590-600 nm. The quantitative measurements showed significant decrease in the amount of polymerized actin in cells incubated with phage for 15 min, followed by gradual increase in F-actin content, but still remaining lower than in untreated cells 45 min after introduction of internalizing phage into cell culture (Figure 2-11).

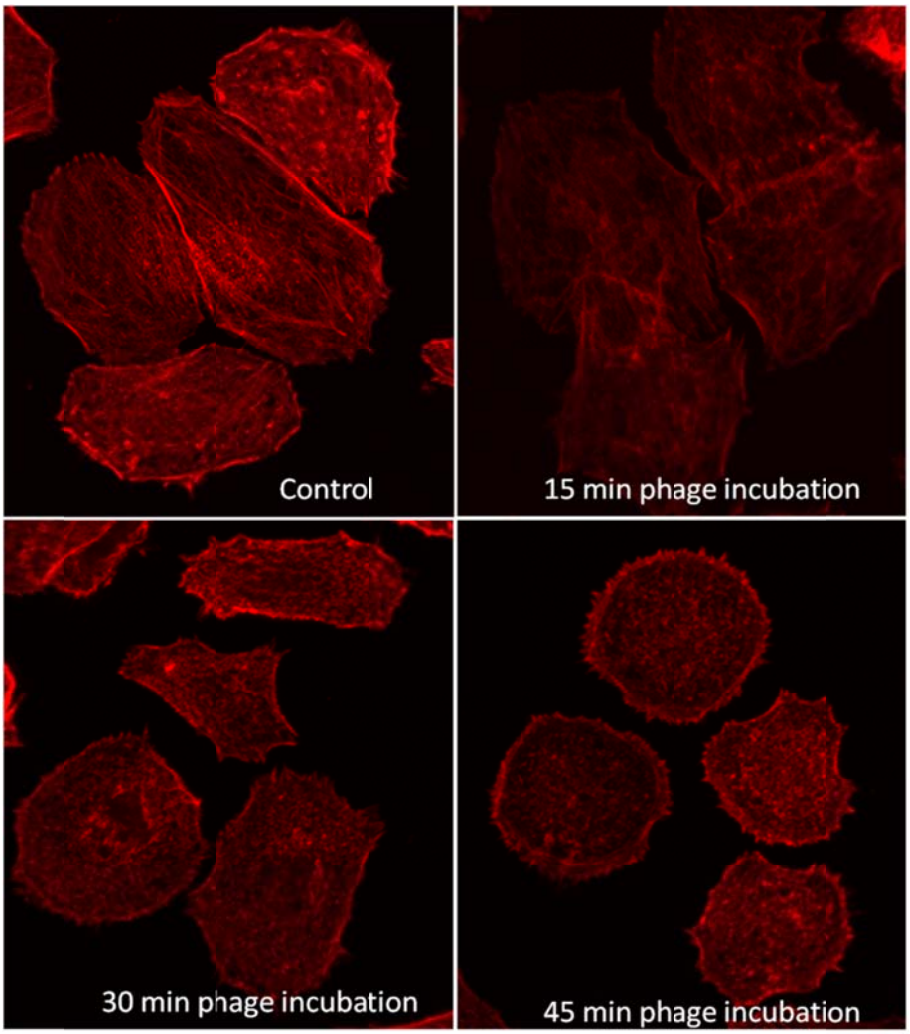

Figure 2-10: **F-actin distribution before and during internalization of phage (L1) into SKBR-3 cells**. Control: SKBR-3 without phage treatment; SKBR-3 cells treated with selected phage for 15min, 30min, and 45min (the actin is labeled with rhodamine conjugated phalloidin). F-actin organization in cells changes during incubation with L1 phage obtained with permission from Ref [39].

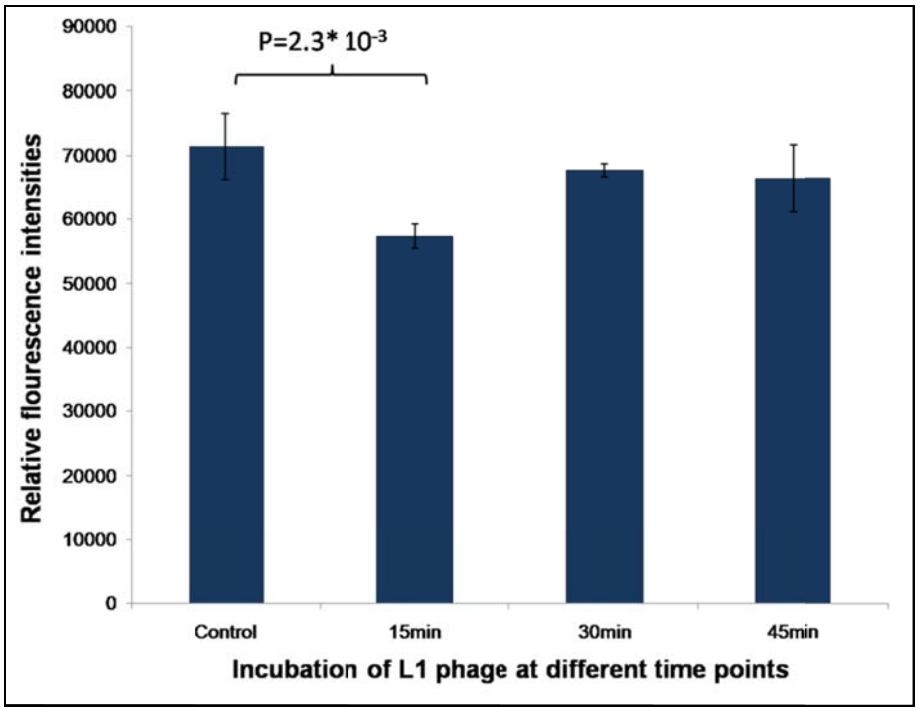

Figure 2-11: **Quantitative estimation of F-actin labeled with rhodamine-phalloidin using microplate reader.** Target SKBR-3 cells are treated with selected phage clone (L1) at different time points (control, 15min, 30min and 45min) obtained with permission from Ref [39].

2.3.6 Isolation and identification of SKBR-3 cell-membrane proteins:

In order to understand to which protein/receptor, the selected phage binds on the target SKBR-3 breast cancer cells we performed affinity precipitation with cross-linked phage. To form a phage-protein (receptor) complex, the selected phage (LI) was

incubated overnight with cell lysate fraction. Following incubation, the resulting complex is pelleted by centrifugation and the proteins adsorbed to the matrix were eluted with low pH elution buffer. As the phage has multiple copies of binding peptides on its surface, we believe it can act as an affinity matrix for isolation of specific proteins. The proteins eluted from the matrix were separated using SDS-PAGE, resulted in the appearance of four bands (approximately 65, 52, 42 and 37 kDa) visualized by silver staining (as shown in Figure 2-12). Following SDS-PAGE separation the bands were sent for N-terminal protein sequencing and mass spec analysis. However, only three bands were sent for N-terminal sequencing as the elution buffer has bovine serum albumin (BSA) and a corresponding band is observed at ~65 kDa. Among the remaining three bands, one strong and characteristic band is observed at around 52 kDa (shown in red asterisk). The samples were further stained with amido-black staining and excised for sequencing. The N-terminal protein sequencing result demonstrated it is a novel and unnamed protein. As the molecular weight from gel electrophoresis is relative, mass spec analysis confirmed the exact molecular weight is ~52 kDa. Alternatively, we are planning to obtain the complete sequence of the protein using peptide fingerprinting. Further experiments are under investigation to understand the exact nature and role of these isolated proteins.

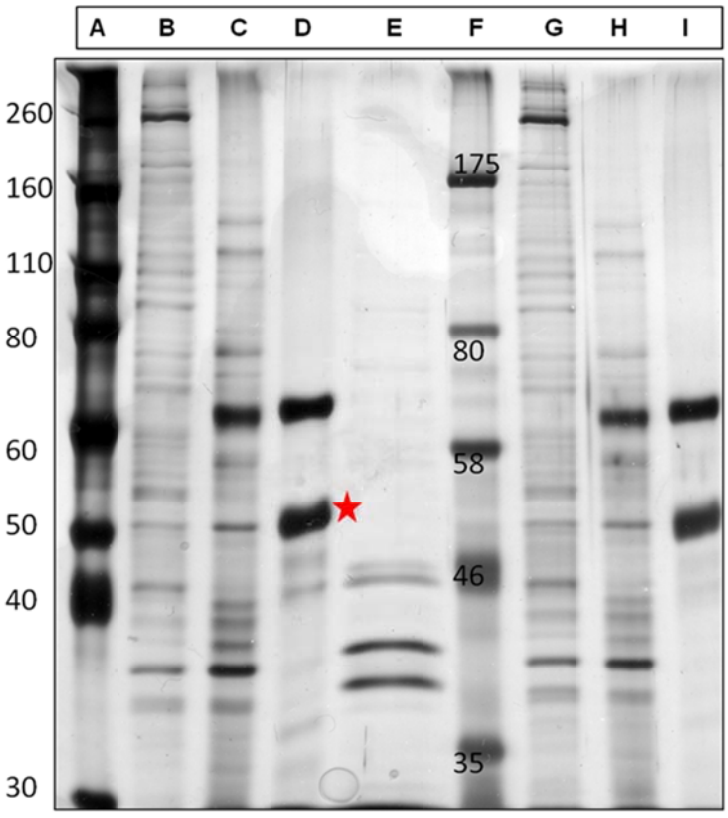

Figure 2-12: **Identification of L1phage-isolated SKBR-3 cells proteins.** (A, F are molecular markers, B: Biotinylated cell lysate fraction, C: represents clarified cell lysate, D: Contains LI phage isolated SKBR-3 proteins, E: L1 phage fraction. (All these samples are boiled for 5 min at 95^{o}C). Samples G, H, I represent the unboiled fractions of B, C, D respectively.

2.4 Discussion

There is a continuing demand for short peptide ligands such as cell internalizing peptides that can serve as cancer-specific diagnostic and therapeutic probes [102]. Phage display has been proven to be successful in exploring protein-protein interactions between the ligand and the receptor [137]. In this work, we used landscape phage display technique as a tool to identify such cell internalizing peptides specific to SKBR-3 cells and analyzed their similarity to the natural protein ligands of the breast cancer cells. Since earlier studies indicated that ErbB2 is overexpressed on the SKBR-3 cancer cells [138], we compared our selected peptide sequences with protein ligands and anti-ErbB2 antibody that bind to receptors of the ErbB family. As expected, our newly identified sequences show homology with natural ligands such as human EGF, amphiregulin, neuregulin, β-cellulin, heregulin and epigen and anti-ErbB2 antibody (Tables 2-2 and 2-3). Our results are also in agreement with earlier reports in which breast-tumor-binding peptides (**SSPWS**AY and Y**SS**P**TQ**R) were selected by using a pIII phage display library (C7C from New England Biolab) [139]. Obviously, our selected sequences (DG**SIPWS**T and V**SSTQ**DFP) with highest frequency (Table 2-1) have at least four amino acids in common with the previously described tumor-binding peptides (**SSPWS**AY and Y**SS**P**TQ**R). Based on the occurrence and phage capture ELISA results (Table 1 and Figure 2-4), we categorize the peptides VSSTQDFP and DGSIPWST as the best binders to SKBR-3 cells under stringent conditions. It is remarkable that the

sequences of these peptides differ from the earlier discovered binding peptide sequences, showing that the landscape libraries used in this work can provide a more diverse repertoire of the cancer cell-binding probes [118]. It is still unclear why and how the phages displaying VSSTQDFP and DGSIPWST (our selected cell internalizing peptides) can enter the SKBR-3 cells. From previous studies, proline and charged amino acids were found to be involved in cell internalization [140, 141, 142, 143]. Thus one possible explanation could be the presence of proline residue in these peptides in conjunction with charged amino acid residues in these peptides.

To further investigate the possible mechanism of phage penetration into SKBR-3 cells, we have studied the effect of energy depletion. The phage internalization was abolished at $4^{o}C$ (Figure 2-6 D-F) and in the presence of ATP inhibitors such as sucrose and sodium azide (Figure 2-6 G-I), indicating that the cellular uptake is an active process requiring energy supply. Our energy depletion studies and preliminary studies using specific inhibitors against individual cell internalization mechanisms such as phagocytosis, pinocytosis and endocytosis show that the phage is entering SKBR-3 cells through endocytosis or specifically through receptor mediated endocytosis. One possible reason for the internalization of phage displaying L1 or L2 sequence could be the intermolecular forces prevailing between the exposed peptides and amino acid residues in EGF receptor. There could be weak hydrogen bond formation between the side chains of threonine in selected peptide and asparagine residue in EGFR leading to the receptor mediated endocytosis. Another possibility could be the formation of hydrophobic

interactions between the isoleucine and phenyl alanine residues from selected peptides with that of leucine residues in the EGF receptor. Nonetheless, the detailed mechanism of phage entry displaying these peptides is still under investigation.

While studying the possible mechanism of phage internalization we also focused on the actin dynamics when selected filamentous phage (L1) is internalized into SKBR-3 cells. We hypothesize that phage is internalized using endocytosis mechanism as stated by previous studies [107]. Multiple studies indicate that actin reorganization is involved in the process of endocytosis [144, 145, 146, 147, 148, 149]. We believe that in the process of endocytosis, when the phage comes in contact with the cell membrane receptor, invagination of the membrane is initiated and might result in the formation of vesicles. Although the contact of phage with the cell membrane is the key step in the endocytosis, the exact underlying mechanism is not well understood. Since one possibility could be the involvement of cell cytoskeleton and its associated proteins in the process of phage internalization, we focused our study on the actin cytoskeleton dynamics during phage entry into breast cancer cells. We used video microscopy followed by confocal fluorescence imaging to study cell behavior and visualize actin filaments before and after the phage entry to further our understanding of the mechanism of phage entry. We observed two significant changes in cell motile activity when phage is internalized into SKBR-3 breast cancer cells. One is the change in the behavior of the leading edges of SKBR-3 cells and another is the change in the dorsal ruffling of SKBR-3 cells. Lamellipodia, a thin protrusive structures that arise from the cell cortex undergo a

dynamic fluctuation at the leading edges of cells. They are protruding and withdrawing in rather cyclical manner in SKBR-3 cells prior to a introduction of the phage into the cell environment. After the introduction of the phage, the characteristic increased ruffling of SKBR-3 cells was observed for the duration of the experiment (45 min). This increased rate of the lamellipodia formation both at the cell periphery and at the dorsal surface is a sign of dynamic reorganization of mostly cortical actin in the cells, since it is well known that actin polymerization and depolymerization is a driving force for the formation of protrusions and the ruffling of the cell edge [150, 151, 152, 153, 154, 155, 156, 157, 158]. The changes in F-actin pattern of distribution observed in fluorescence images in Figure 2-10 are characteristics of changes in the state of actin polymerization. Microspikes, filopodia and lamellipodia are shaped by dense core of actin filaments and changes in actin state of polymerization and distribution reflects the dynamic re-organization of actin during phage entry.

Inside the cell, actin exists in two forms either as polymerized helical form commonly known as filamentous actin or F-actin and as unpolymerized globular form known as G-actin. In order to investigate the changes in the state of polymerization of actin during phage internalization, the cells were treated with phage for different times and immediately fixed with paraformaldehyde and incubated with rhodamine-phalloidin to label F-actin. The relative fluorescence intensities of rhodamine in Figure 2-11 represent the amount of polymerized actin in phage treated cells. During incubation of cells with phages for up to 45 min we observed a net depolymerization of actin cytoskeleton in the

initial 15 min after the introduction of phage into the cells' environment. Interestingly, 15 min was the earliest time we observed phages bound to SKBR-3 cells using scanning electron microscopy in our previous study [159]. Thus the time of increased actin depolymerization correlates with the time during which the process of the phage entry into the cells takes place. The possible rearrangement of actin in SKBR-3 cells when landscape phage is internalized is shown in Figure 2-8. There have been reports indicating that actin dynamic reorganization is involved in the entry of the Kaposi's sarcoma herpes virus into endothelial cells [160] and influenza virus into epithelial cells [161]. Also it has been recently reported that the uptake of charged polystyrene nanoparticles into HeLa cells is mediated by the reorganization of actin [162]. Our results also show that entry of filamentous phage into the SKBR-3 cells involves the reorganization of actin cytoskeleton and similar mechanism may be used by the phage to enter breast cancer cells. More detailed biochemical investigations are necessary to understand the possible signaling pathway/s and associated actin binding proteins involved in phage internalization into epithelial breast cancer cells.

In conclusion, usage of landscape phage libraries identified new SKBR-3 breast cancer cell targeting or internalizing peptides (VSSTQDFP and DGSIPWST) which bind to SKBR-3 cells with high affinity, selectivity and specificity. These novel peptides can serve as targeting agents for multiple biomedical applications including targeted anti-cancer agents, improved diagnosis and treatment purposes.

Chapter 3 : Synthesis and Characterization of protein-nanoconjugates (GNR-pVIII) for SKBR-3 breast cancer cell imaging and destruction.

3.1 Introduction

Recent advancements in nanotechnology have opened doors for novel therapeutic agents that can be used for early detection of cancer [163, 164, 165]. However the current challenge is to understand their exact role at molecular level. Breast cancer is one of the most fatal cancer causing diseases [166] and can only prevented through the early detection and removal of premalignant lesions. Despite the advancement of science, breast cancer still remains the fourth most common cancer in the United States [47]. Thus, development of new approaches that are compatible with conventional methods are highly desirable [167].

Recently, photo thermal therapy involving deep penetrating near infra red (NIR) radiations has emerged as a promising treatment modality due to its ability to deliver lethal doses of heat at the target site. The desired thermal effect can be achieved by a suitable vector with two important capabilities: exogenous NIR absorbing ability and receptor binding moiety. Metal nanoparticles with excellent optical properties [168, 169] are believed to be suitable candidates for photo thermal therapy [170]. Even through receptor specific antibodies are good targeting source against cancer marker they are limited in use by their size, cost of production and immunogenicity in an *in vivo*

environment [171, 172]. Moreover, antibodies are limited in availability and may not recognize unknown receptors that over express in tumor cells. Thus, current identification of new cell targeting/ internalizing peptides using evolutionary selection procedure might serve as an alternative source for antibodies.

Biological systems involving bacteriophage offer enhanced specificity and are environmentally friendly for nanomaterial synthesis [173, 174]. Several researchers have used phage as therapeutic agent [175] and phage libraries as a tool kit for identifying novel cell targeting ligands [176, 177]. The primary structure of major coat isolated from phage libraries has three distinct domains 1) acidic N-terminus domain (retaining target specificity) 2) a central hydrophobic core (aids in protein-protein interactions) and 3) a basic C-terminus domains (electrostatically interacts with the DNA in native virus) [178]. Thus, filamentous virus can be simply viewed as the assembly of major coat proteins onto DNA template using non covalent interactions.

Recently, we identified new SKBR-3 cancer cell internalizing ligands using landscape phage libraries [179] as described in the previous chapter. As the screened filamentous viruses specific to a target cancer cell has unique amino acids sequences displayed on their N –terminus, we hypothesize the coat proteins isolated from target specific phage retains its target binding nature. Also, viral proteins have multifunctional groups on their surface; they can be easily conjugated with nanomaterials to form next generation nanovectors. Taking advantage of the specificity from isolated coat proteins

and optical properties from nanorods, we synthesize novel nanoprobes termed protein nanoconjugates (GNR-pVIII).

3.2 Experiments performed

3.2.1 Cell culture

Target human breast epithelial carcinoma (SKBR-3) and control normal breast epithelial cells (MCF-10A) were purchased from ATCC (HTB-30^{TM} & CRL-10317 respectively).The SKBR-3 and MCF-10A cells were cultured in Mc.Coy's 5a modified medium and DMEM/F-12 medium supplemented with fetal bovine serum (10%) and suitable antibiotics (100 μg/ml of penicillin and 100 μg/ml streptomycin from sigma). Additional control fibroblasts were maintained in DMEM medium. All the cells were grown at 37^{o}C in 5% CO_2 and sub-cultivated for experimental procedures every 3-4 days.

3.2.2. Amplification and purification of SKBR-3 specific fd-tet bacteriophage

Landscape phage libraries (f8/8 libraries) were obtained from Dr.Petrenko at Auburn University and SKBR-3 specific phage displayed with VSSTQDFP sequence on the N terminus of major coat protein was screened using landscape phage library as described elsewhere [179]. Phage suspension was obtained by infecting starved cells (*E. Coli* k91blukan) with fd-tet bacteriophage. 40 ml of NZY medium containing 20 μg/ml of tetracycline was inoculated with a fresh single colony of phage-infected cells in a 250

ml flask. The culture was incubated under shaking at 37^0C and 200 rpm overnight. The overnight culture was then poured into a 250ml Beckman centrifuge bottle and centrifuged at 3000 g for 10 min at 4^oC. The supernatant was poured into a fresh tube and centrifuged at 9300 rpm for 10 min at 4^oC. The resulting clear supernatant was again poured into a fresh tube into which a 6 ml PEG/NaCl solution (100 g PEG 8000, 116.9 g NaCl and 475 ml water) was already added. The tube was kept at 4^0C overnight for phage precipitation. The precipitated phages were collected by centrifugation at 13000 rpm for 60 min and the supernatant was removed. The pellet was then dissolved in 1 ml Tris buffered saline (TBS) in a micro-centrifuge tube and centrifuged again at 13000 rpm for 10 min to remove any non dissolved material. Later, polyethylene glycol/NaCl solution was added and incubated overnight at 4^oC. The phage precipitate was collected by centrifuging at 13000 rpm for 60 min using a high performance Beckman coulter centrifuge and the final phage pellet was resuspended in 1ml of fresh TBS. The concentration of phage was estimated using a UV-visible spectrophotometer at 269nm.

3.2.3 Isolation of major coat protein pVIII:

There are two different approaches to isolate major coat proteins from filamentous bacteriophage. One is phenol extraction method and the other is cholate extraction. Even though the major coat protein can be isolated using phenol extraction method [180], as demonstrated in previous studies, the cholate extraction yields a significant amount of α-helix structure with lower aggregation values. Therefore, we

adapted the cholate isolation method to obtain the cancer cell specific major coat protein. In this procedure, SKBR-3 specific phages were first disrupted into DNA and proteins by the sonication of a chloroform saturated buffer and then fractionated using sepharose column chromatography [121, 181]. Briefly, 5 mL of purified phage solution (1x 10^{14} virions/ml) was mixed with 10ml of 120mM cholate in 10mM Tris-HCl, 0.2mM EDTA, pH 8.0, and chloroform(2.5% v/v). The mixture was incubated for 1h at 37^{O}C with occasional stirring. The dissociated phage was then applied to a sepharose column and eluted with 10mM cholate in 10mM Tris-HCl/0.2 mM EDTA, pH 8.0, to separate the major coat proteins from the phage DNA. The various fractions at 1mL each was then collected and analyzed using a UV-Visible nanophotometer. Fractions with an absorbance ratio of A280/A260 greater than 1.5 were stored at 4^{o}C for further use. The protein concentration was estimated using a Bradford assay and the purified protein was confirmed by 15% SDS-PAGE electrophoresis and western blotting.

3.2.4 Synthesis of CTAB-capped gold nanorods (GNR)

Gold nanorods (GNRs) were synthesized using an established protocol developed by Nikkobath et. al. [83, 182]. First, 10 mL of seed solution was prepared in a 15 mL sterile centrifuge tube. In this procedure, to 9.6 mL of water 0.364 g of CTAB (0.1 M) was added and vortexed to form a clear solution. To this 0.425 mL of $HAuCl_4$ (5 mM) was added. Later under vigorous stirring 0.6 mL of freshly-prepared ice-cold $NaBH_4$ solution (10 mM) was added all at once. The resulting seed solution was allowed to sit

for at least 1 h to ensure the excess reducing agent is reacted. The growth solution was prepared in a separate 50 ml falcon tube by adding 75 μL of $AgNO_3$ (60 mM) to 1.6 g of CTAB solution (0.105 M) in 40 mL water. To this solution 3.825 mL of $HAuCl_4$ (5.886 mM) was added and allowed to sit for 1 h. Later, 1.05 ml of HCl (1M) was added to the above solution and the falcon tube is gently inverted. Then 465 μL of freshly prepared ascorbic acid solution (0.0788M) was added, and inverted with hand. The solution becomes color less when ascorbic acid is added. To this solution 112.5 μL of seed solution (prepared in the beginning) is added gently inverted with hands and left undisturbed overnight in dark. The synthesized GNRs were characterized by a UV-visible NIR spectrophotometer and transmission electron microscopy (TEM) measurement.

3.2.5 Synthesis of polyethylene glycol (PEG) functionalized GNRs:

For PEG modification, 3.0 mL of the above mentioned CTAB stabilized GNRs solution was centrifuged twice at 13,000 rpm for 20 min to remove the excess CTAB. The resulting pellet was resuspended in phosphate buffered saline (PBS) at pH 7.5. Meanwhile, a 20 μM PEG polymer (NH_2-PEG-SH; molecular weight: 5000 Daltons) was prepared in PBS. Later 1 mL of GNRs solution was mixed with 500 μL of PEG solution and incubated overnight under shaking. The following day, the solution was centrifuged at 13,000 rpm for 20 min and the pellet was dissolved in 1 mL of PBS (pH 7.5). The successful modification or coating was confirmed by UV-Visible spectrophotometer and Fourier transform infrared spectroscopy (FTIR).

3.2.6 Synthesis of protein nanoconjugates (GNR-Phage protein):

Based on the primary structure of coat proteins as described in introduction, the isolated protein has three distinct regions: 1) an acidic N-terminus with the cancer cell specific peptide exposed outside (1-20 amino acids), 2) a central hydrophobic core which aids in protein-protein interactions in the native virus (21-39 amino acids) and 3) a basic C-terminus with four lysine residues that are actively involved in forming electrostatic interactions with the DNA backbone in the native virus [178]. Since the foreign peptide specific to the target cancer cell is present on the N (amino)- terminus end, it is protected with a blocking agent and the carboxyl group on the C-terminus is utilized to form a covalent bond with the amino group of PEG in functionalized nanorods. Briefly, the N-terminus of the protein was first blocked with tert-Butyl carbamate (BOC) and carbodiimide (EDC) chemistry was used to form a covalent bond between the carboxyl terminus of the protein and the amino functionalized gold nanorod (GNR-PEG). There are four major steps involved in the synthesis of GNR-Phage protein complex. They are protection (BOC), activation (EDC/NHS), conjugation with nanorods (PEG functionalized nanorods) and deprotection (removal of BOC). We termed the resulting complex as protein-nanoconjugate (GNR-pVIII) or hybrid nanoconjugate. The schematic diagram of the protein-nanoconjugate (GNR-pVIII) is shown in Figures 3-1. In this procedure, 1 mL of protein (1.12 mg/mL determined from spectroscopic measurements A_{280}) was treated with 2.1 µl of BOC and incubated for 2-6 hrs. Then, the carboxyl terminus of the protein was activated with 50 µL of EDC (0.3 mg/mL) and 25 µL of NHS

(0.2 mg/mL). To synthesize protein-nanoconjugate (GNR-pVIII) with covalent interactions, 20µL of activated pVIII protein was added to 1 mL of GNR-PEG solution in an eppendorf tube and incubated for 30 min under oscillation. After incubation, the mixture was centrifuged twice at 13,000 rpm to remove any unbound pVIII protein and finally re-suspended in phosphate buffered saline, PBS (pH 7.4). The resulting protein-nanoconjugate is found to be stable at 4 ºC for up to 2 weeks. Finally, the BOC is unprotected using mild acidic conditions. The successful modification was confirmed by UV-Visible spectrophotometer and Fourier transform infrared spectroscopy (FTIR).

3.2.7. Binding studies (GNR-Phage protein complex)

The binding affinity between the phage proteins and the PEG functionalized gold nanorods were determined using a fluorescence spectrophotometer with constant protein concentration (A<0.05) and varied GNR-PEG concentration (0 – $2X10^{-12}$M). The intrinsic fluorescence of protein from tryptophan residues were excited at 280 nm and the emission was collected between 300-400 nm.

The binding and dissociation constants were calculated based on the following equation which is slightly modified from the previously reported formulae [183].

$$F_0\text{-}F/F\text{-}F_\infty = (GNR/K_{diss})^n \qquad \text{(equation 1)}$$

The binding constant, K_b, was obtained by plotting log $(F_0\text{-}F)/(F\text{-}F_\infty)$ versus log (GNR), where F_0 and F_∞ are the relative fluorescence intensities of tryptophan from protein alone and the protein saturated with GNRs, respectively.

3.2.8 Cytotoxicity (MTT assay) and serum stability measurements

The cytotoxicity of the synthesized nanoconjugates were evaluated by measuring the metabolic activity of the cells by using 3-(4,5-dimethylthiazol-2-yl)-2,5-diphenyl tetrazolium bromide assay (MTT assay) as described before [184, 185]. The results were expressed as percentage cell viability. Briefly, the target and control cells were cultured in a 96 well plate and incubated with different concentrations (0.2μM- 0.2nM) of GNRs, GNR-PEG, GNR-PEG-pVIII complexes for different time points (1h, 6h, 24h and 36h). After specified incubation, the cells were completely washed and treated with 50 μL of MTT reagent (5 mg/ml) and incubated for 4 h at 37^{o}C. After the incubation, the cell were thoroughly washed with PBS and treated with 100 μL of DMSO treatment. Later, the amount of color developed was measured using plate reader at 570nm and cell viability was calculated as a percentage viable cell in comparison to control untreated cells. To further verify the stability the nanoconjugates were centrifuged and dissolved in two different solvents (PBS and Serum) and the UV-Visible spectrum was measured to confirm its stability. TEM section cutting was performed to confirm the entry of GNR-pVIII into SKBR-3 cells.

3.2.9 Specificity, Imaging and Photo thermal destruction studies

Three different cell lines, namely SKBR-3 cells, MCF-10A cells and fibroblast, were incubated with GNRs, GNR-PEG and GNR-pVIII conjugates and tested for specificity, imaging and photo thermal destruction abilities. Briefly, stock solutions of

gold nanorod and protein conjugates which are stored at $4^{o}C$, are brought to room temperature and diluted with medium before incubation with target and control cell lines. The cells were rinsed with D-PBS and incubated with gold nanorods and nanoconjguates having an optical density of 0.5 at $37^{0}C$ for 30 min. As a control, free PBS without nanorods was added. After incubation, the unbound nanorods were removed by rinsing thoroughly with PBS. In case specificity experiments, the cells were fixed with 4% para formaldehyde in PBS and incubated for 15 minutes at $37^{o}C$. Later the buffer containing the fixative was removed and cells were rinsed twice in PBS. Then the cells were permeabilized with 0.1% triton x-100 and incubated for 2 min. After incubation period the cells were washed three times with PBS and incubated with anti pVIII antibody for 1hr. Rinsed thoroughly and labeled with IgG conjugated rhodamine for 1h. The non specifically bound dye is removed by repeated washes and the cells nuclei were counter stained with DAPI for 5 min and mounted on a microscope slide. The cells were examined using a Nikon Eclipse Ti inverted fluorescence microscope system. For imaging purposes, the cells were cultured on cover glasses and incubated with conjugates as described above, washed thoroughly to remove non specifically bound nanorods, fixed in 4% para formaldehyde in PBS and mounted on a microscope slide. The slides are directly viewed under a dark field microscope to get the back scattered images. For photo thermal therapy (PTT) experiments, the cells were incubated as described above and thoroughly washed. Later, the target and control cells were exposed to NIR (near infra red) light using a continuous wave (CW) laser at 808nm. The power densities were varied

from 0.079 W/cm^2 to 5 W/cm^2. The live and dead cells were analyzed using a viability kit (calcein AM and Ethidium homodimer live/dead viability/ kit for mammalian cells from Molecular Probes). The data obtained was further quantified according to the manufacturer's instructions. All the statistical analysis was performed using student's t-test.

3.2.10 Live imaging of SKBR-3 cells treated with protein-nanoconjugates

SKBR-3 cells cultured on 25-mm cover glasses as described above were transferred to a perfusion filming chamber just before filming. The chamber was placed on the stage of a Zeiss Standard microscope enclosed in a plastic bag and the temperature was maintained at 37^{o}C with an air curtain incubator (Sage Instruments). Digital images of live cells were recorded every 10 seconds. Cells were recorded for 15 min in McCoy's 5A modified medium and then for 70 min using only a GNRs solution (without protein) and a nanoconjguate (GNR-pVIII) solution. These solutions were perfused into the chamber using a 2.5-cc syringe driven by a syringe pump (Sage Instruments model 341A). Frame-by-frame analysis was performed using the software (Videos can be found in the original manuscript as separate files).

3.2.11 Gene expression studies using microarray

In order to explore the cascade of molecular interactions during protein-nanoconjugates incubation with our model SKBR-3 cells, we compared the

transcriptional profile of untreated SKBR-3 cells to that of cells treated with nanoconjugates. SKBR-3 cells were incubated with nanoconjugates for 6 h and washed thoroughly with PBS. The RNA from the untreated SKBR-3 cells as well as from the GNR-pVIII treated cells was isolated using an RNeasy Kit (Qiagen, USA) according to the manufacturer's instructions. All of the experiments were performed in triplicates. The quality control check (as shown in Figure 3-14), cDNA preparation, array hybridization and scanning was performed by the Oklahoma Medical Research Foundation (OMRF) microarray research core facility. The Illumina WG-6_v3 arrays targeting >48,000 transcripts and variants were used in triplicates for each experimental condition.

3.2.12 Microarray Data analysis

The Illumina WG-6_v3 array data for each experimental condition was exported from BeadStudio Software for further analysis. The data was normalized as described previously [186, 187], using the variability of lowly expressed genes as a reference point. In order to find genes expressed above the level of technical noise, a frequency histogram of raw expression values was examined for each array. The histogram yielded a right-skewed unimodal distribution curve with the mode around 75. A normal distribution curve representing the variability of the data around zero was then fitted around the mode, mirroring the Gaussian profile of the left part of the histogram. Its parameters were then defined (mean, SD) and the data were normalized to the standard deviation of the noise after subtraction of the mean. The arrays were then Log10-transformed and adjusted to each other by robust linear regression under the assumption

that the expression of most genes does not change. The data was then filtered to remove genes with an expression value less than 3.0. This is equivalent to setting a threshold at 3 SD above the noise level. Genes expressed below the noise level under all experimental conditions (about 1,600) were excluded from consideration, as their expression cannot be reliably assessed. Full microarray data were deposited in the Gene Expression Omnibus (GEO, GSE23118) and are accessible on the GEO web-site.

To identify differentially expressed genes between two experimental groups, we used associative analysis as described by Dozmorov et al. [187]. Briefly, in pooled microarray datasets, a reference group of genes expressed above background with a low variability of expression was identified by an F-test. The assumption is that because most genes do not change expression in any experiment, the variability of expression among the group is due to random, technical factors alone. Genes with statistically significantly variability above the random, technical variation are assumed to vary for biological reasons. A t-test, termed "associative t-test," was applied to test if a given gene belongs to or differs from the group. The associative t-test is a standard t-test applied to compare the expression variability rather than differences in mean values. To identify an evaluable number of differentially expressed genes, a stringent criterion was applied. Only genes expressed below noise level in one group and greater than 5 SD above noise level in another group were selected for further analysis. For genes that were expressed above noise level in both conditions, as well as those that have greater than 1.5-fold differences in expression levels and expressed greater than 10 SD above noise level in at

least in one condition were also selected. These genes can be considered as "beacons" that point to pathways or gene networks that are altered.

To classify each group of genes in more detail by their ontological properties, we used the Database for Annotation, Visualization and Integrated Discovery (DAVID) [188]. The Gene Functional Classification tool in DAVID builds clusters of genes with significantly similar ontologies as tested against an entire list of genes in the Illumina WG-6_v3 array. Medium stringency was used to yield a comprehensive set of ontological groups and to group genes with similar functions. Increasing or decreasing stringency resulted in the identification of fewer or more groups of genes with similar functions but did not produce any additional information.

Lists of genes from individual clusters were submitted to Ingenuity Pathway Analysis (IPA; Ingenuity® Systems, Redwood City, CA, http://www.ingenuity.com). Ingenuity maps gene IDs to a database and performs statistical computing to identify the most significant ontologies, canonical pathways, and networks overrepresented in a given gene list as compared with the entire list of genes in the Illumina WG-6_v3 array. By default $p<0.05$ was used in all calculations. Gene lists from each group were analyzed for overrepresented general functions, canonical pathways, and the networks that can be assembled from them.

3.2.13 In vivo feasibility experiments

3.2.13.1 Mice housing

All the animal experiments were conducted according to the guidelines provided by Institutional Animal Care and Use Committee (IACUC), University of Oklahoma, Norman campus. Nude mice of 3 to 5 weeks age (n=50), weight (15.67 ±2.09g) (Mean ± SD), weight ranged from 9.7g to 19.4g, purchased from Jackson laboratories were housed in a special caged ventilators for animal care. Mice were feed with standard mice food and bedding was changed twice a week. Body weight and tumor size was measured weekly. All the animal experiments were done in collaboration with our post doctoral fellows Dr. Kay Guo and Dr. Zipeng Zen.

3.2.13.2 Development of in vivo breast tumor model

Once the SKBR-3 cells reached 90% confluence and harvested, they are re suspended in serum and antibiotics free Mc. Coy's medium at a concentration of 1×10^7 cells/ml. In order to inject the cancer cells into the nude mice , skin was sterilized using 70% ethanol, and then 1×10^6 cells/side in 0.1 ml Mc. Coy's medium were injected into the back of mice under skin on either sides. After 2-3 weeks of SKBR-3 cells injection, the tumors were visible to the naked eye and the size of the tumor was measured from cross-sectional area (length/2 × width/2 × π) using a digital caliper. After two-three weeks, when the tumor size was reached to $25mm^2$ the mice is chosen for experiments. The tumor developed was confirmed using hematoxylin and eosin staining (H & E).

3.2.13.3 In vivo Specificity and Imaging studies

Once the tumor presence is confirmed by using H & E staining, three mice were chosen for specificity experiments. As a control one mouse was injected with 150 µl of PBS. The other two mice were injected with 150 µl of GNR and protein-nanoconjugates (GNR-pVIII) solutions respectively. The nanoparticles were allowed to circulate for 24 h and the following day the animal was sacrificed and the tumor is excised for immune-histochemcial studies. For immune labeling, the tissue sample is embedded in paraffin and cut into 5 micron thick slice using microtome and mounted on a positively charged slide. The slides were dried at room temperature overnight to remove water that is trapped under the tissue. Later, the slides are deparaffinized and rehydrated by placing them in the beaker in the following order : xylene for 5 minutes each (twice) ; xylene: ethanol (1:1) for 5 minutes (once) ; 100% ethanol for 5 minutes each (twice); One time with 95% ethanol for 5 minutes; one time with 70 % ethanol for 5 minutes; one time with 50 % ethanol for 5 minutes. Finally the slides are rinsed under running cold tap. (Slides should not be dried from this point). Later, the antigens were retrieved using enzymatic method and continued for immune staining. For primary antibody labeling the slides are washed twice with TBS- 0.02% Triton x-100 and blocked in 10% serum with 1% BSA in TBS for 2 hours at room temperature and then primary antibody (anti pVIII antibody) diluted in TBS with 1% BSA was added and incubated overnight at 4^{o}C. After incubation, the slides are rinsed with TBS-0.025% Triton under gentle agitation and diluted secondary antibody conjugated to fluorescent dye (IgG-rhodamine) was added

and incubated for 1 hour at room temperature. Finally, the slides are rinsed with TBS and tissue is counter stained with DAPI and cover sliped.

3.3 Results

3.3.1 Surface modification of protein-nanoconjugates

Earlier reports suggest that the wavelength shift in SPR or UV-Visible spectrum of gold nanoparticles is linear with the change in refractive index induced by the absorbate layer [189]. Hence, a UV-Visible spectrum is used to examine the possible surface layer coating on GNRs. The scheme of protein-nanoconjugate synthesis is shown in Figure 3-1. The isolated major coat protein used in this study was characterized by gel electrophoresis and western blotting as shown in Figure 3-2. Here, we synthesized nanorods (coated with phage protein) with an aspect ratio of 4.01 and absorption overlapping in the near infra red region with the laser (808 nm) in our lab. Here, the phage protein is bound to PEG functionalized gold nanorods using carbodiimide chemistry. The successful synthesis of the conjugates was confirmed by using TEM and UV-visible spectrophotometer. The electron microscope imaging shows the nanorods are uniform in size and monodispersed and not aggregated upon surface coating with phage protein (Figure 3-3 A-B). In order to visualize the protein bound to nanorod surface, the samples are negatively stained. The light background on the dark nanorod surface in Figure 3-3 (B) might be the protein coated on the nanorod surface. The synthesized gold nanorods exhibits two surface Plasmon absorption bands one strong wavelength band

~760nm corresponding to longitudinal oscillation of electrons and other weak band ~525nm corresponding to the transverse oscillation of electrons. Figure 3.3 (C) shows the absorption profiles of synthesized GNR coated with PEG and nanorod coated with phage protein. Because the λ_{long} (longitudinal SPR band) is systematically red shifted upon the successive coating with the coat protein, we believe the conjugation is successful. The amount of phage protein bound to the functionalized nanorods is measured either by theoretically calculating the amount of free protein present in the nanoconjugate sample or by using standard protein determination methods (bicinchoninic acid). By precipitating the GNR-PEG-pVIII complex in PBS, we could separate unbound protein on functionalized GNR. Thus the phage protein self assembles to form targeted nanoconjugates without any further modifications. Here, PEG is not only used as a linker to conjugate protein but also used to enhance the *in vivo* circulation of these particles.

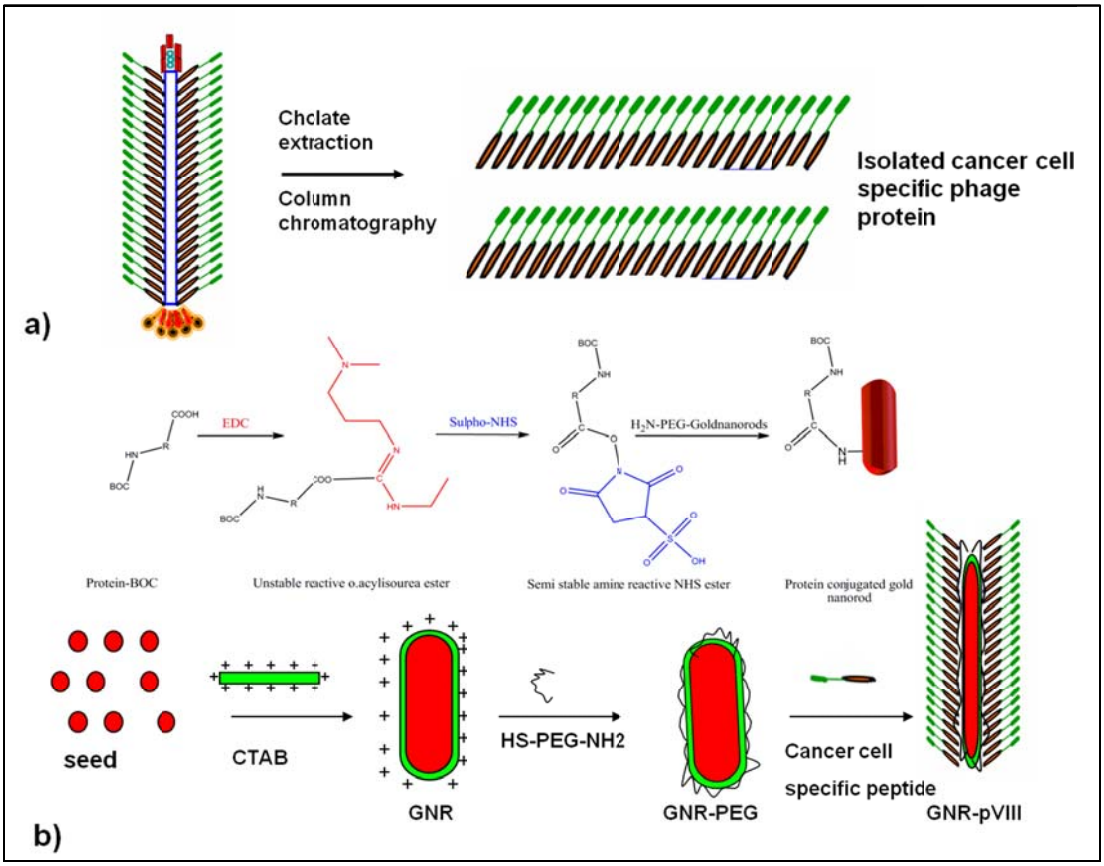

Figure 3-1: Schematic diagram showing the steps involved in the synthesis of GNR-Phage protein conjugates (protein-nanoconjugates) A. Isolation of major coat proteins, pVIII form SKBR-3 specific bacteriophage. B. Synthesis and functionalization of gold nanorods (using carbodiimide chemistry).

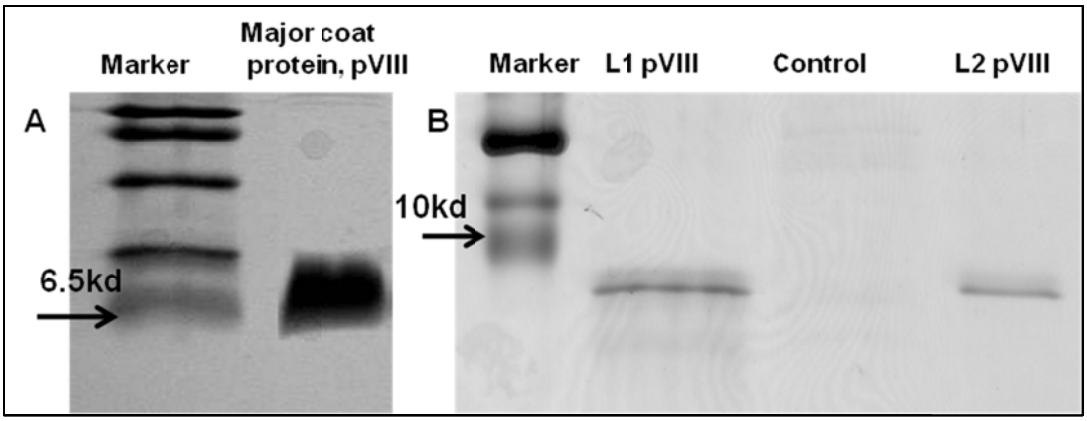

Figure 3-2: Characterization of isolated major coat proteins. A: Commassie staining; B: Immunoblot analysis against anti pVIII antibodies.

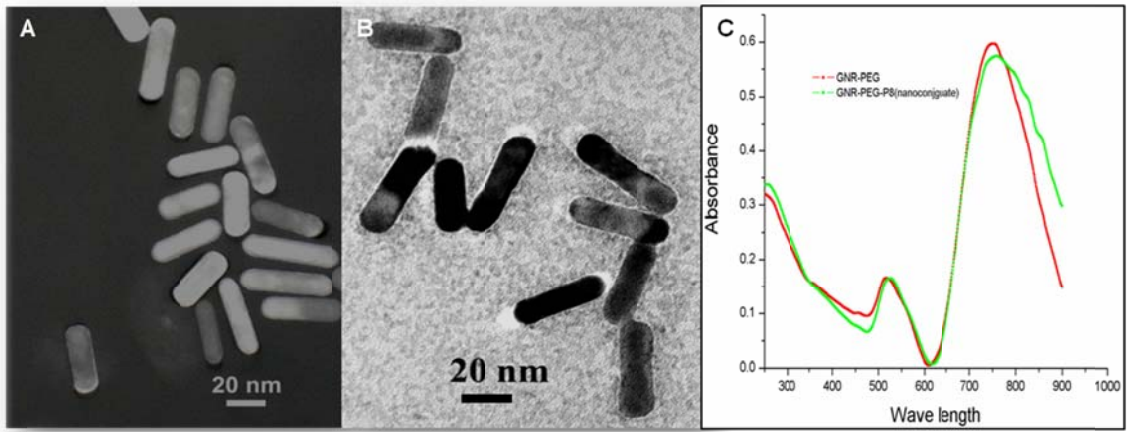

Figure 3-3: Characterization of GNR-Phage protein conjugates (protein-nanoconjugates) A. Transmission electron micrograph (TEM) of Gold nanorods. B. TEM image of gold nanorods conjugates to phage protein with negative stain (Image indicates nanorods are not aggregated upon conjugation). C. Surface plasmon spectra of as synthesized nanoconjugates.

3.3.2 Affinity, stability, biocompatibility and cell internalization studies of nanoconjugates:

As the binding of phage protein to nanorod surface influence their distribution in the cells or tissue, it is important to understand the affinity of protein on the nanorod surface. Hence, the GNR binding to phage protein is estimated using a fluorometric method. Changes caused by different concentrations of GNR are shown in Figure 3-4, the fluorescence emission spectra of phage protein. As expected we observed a fluorescence quenching when protein was bound to the gold nanorod surface. This could be due to a complex formation between the GNR and phage protein. Further analysis of data using double log plot as shown in Figure 3-4 reveals the binding constant of nanorods coated with phage protein is $K_b = 1.2 \times 10^9\ M^{-1}$. This show the affinity between the protein and the nanorod is very high.

In order to understand the stability of various nanoconjguates in serum, we used UV-Visible spectrophotometer to study the aggregation behavior of the synthesized nanoconjugates. As shown in Figure 3-5 no obvious change in the UV-visible spectra of nanoconjugates was observed when the synthesized nanoparticles are transferred from PBS to serum. Instability indicates flattening of the peak. Since, there is no flattening, it confirms the stability of various nanoparticles in serum and their potential use for *in vivo* applications.

The cytotoxicity of nanoconjguates was studied by using MTT assay. Figure 3-6 shows the viability of SKBR-3 cells grown for 24 h in the presence of nanoparticles at a

concentration of 40 μM. Except gold nanorods, other conjugates are found to be non toxic to SKBR-3 cells at this particular concentration. This toxicity of GNR may be due to the presence of cytotoxic CTAB on its surface. The concentration of nanoparticles used for cytotoxic measurements are much higher than the concentration used for performed specificity, imaging and photo thermal experiments.

Cell internalization studies were performed using TEM section cutting. As shown in Figure 3-7 the ultra microtome thin sections of SKBR-3 cells and examination under transmission electron microscopy confirmed the internalization of protein nanoconjugates with in the cells.

The amount of nanorods uptake into our target SKBR-3 cells was measured by incubation at different time points (15min, 1h and 6 h). For these studies, the phage protein is replaced with fluorescently labeled (FITC) synthetic peptide containing the same target SKBR-3 cells binding sequence to that of phage protein. As shown in Figure 3-8 the uptake was observed to be high at 6 h incubation and no characteristic uptake is noticed at 15 min incubation time. Also, we did not observe any significant difference in the fluorescent signal at much higher time points in comparison to 6 h.

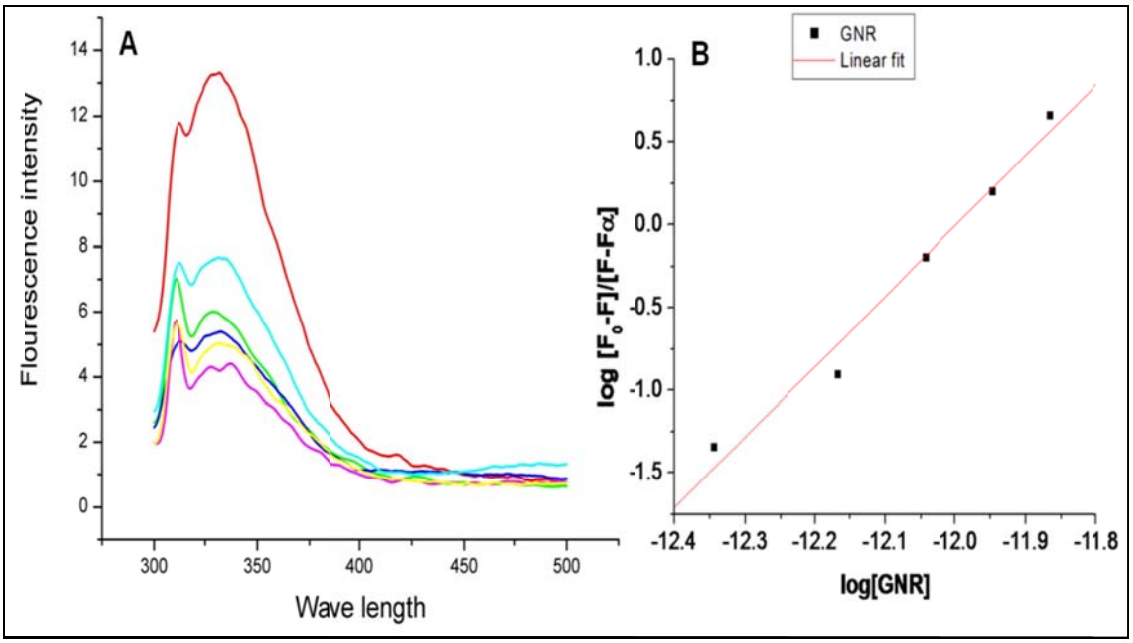

Figure 3-4: Binding studies of GNR-Phage protein conjugate (protein-nanoconjugates) A. Fluorescence spectra of protein conjugated to gold nanorods. B. The double logarithmic plot of protein nanoconjugates.

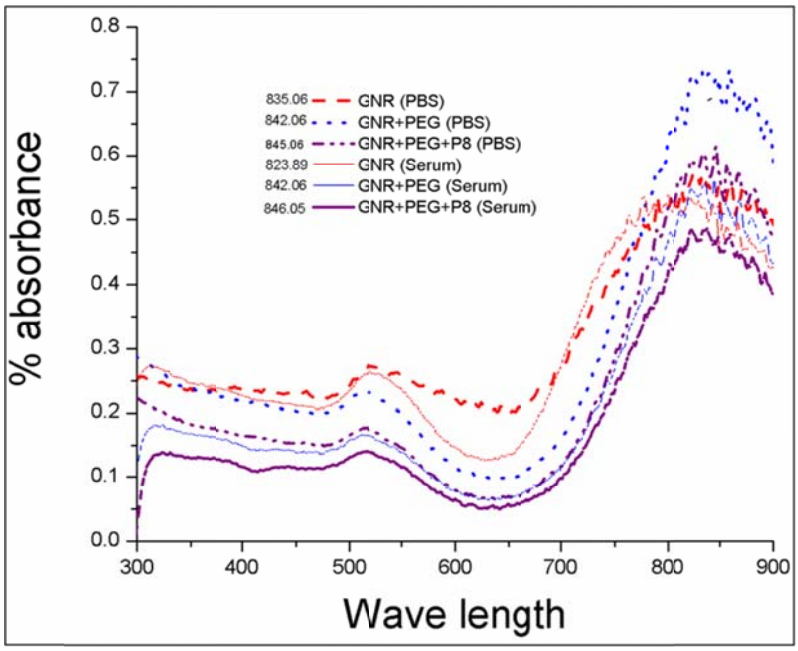

Figure 3-5: Stability of protein nanoconjguates.

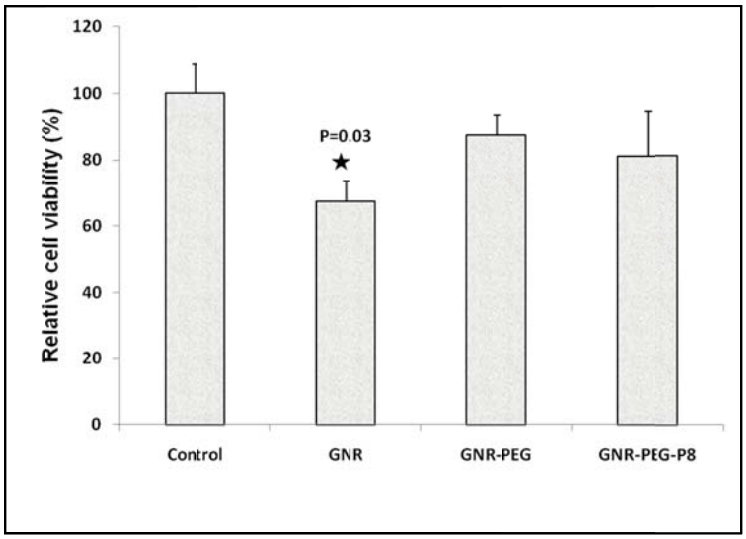

Figure 3-6: Cytotoxicity of the synthesized protein nanoconjguates.

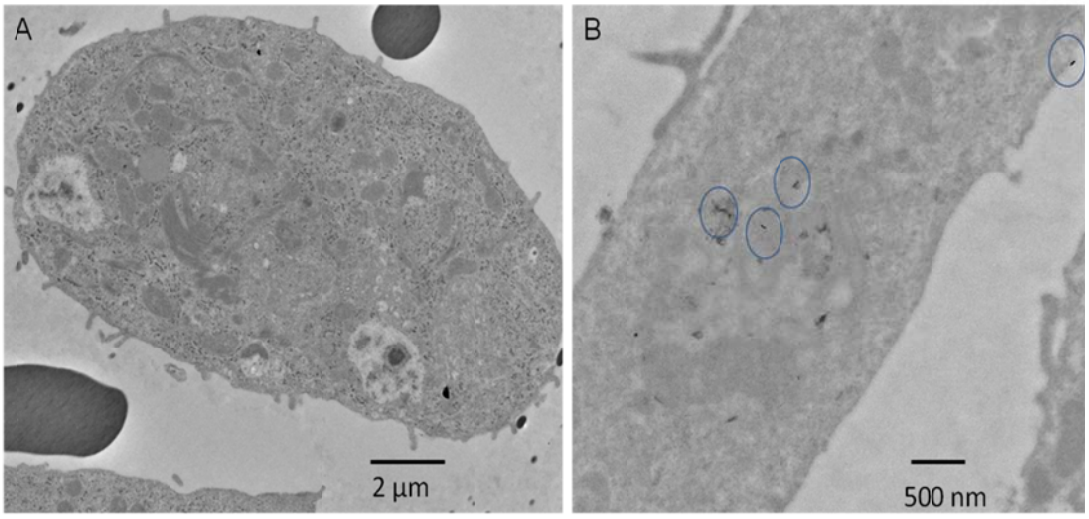

Figure 3-7: Internalization of protein-nanoconjugates using section cutting.

A: Cross section of SKBR-3 breast cancer cell. B: Internalization of protein nanoconjugates (circled in blue).

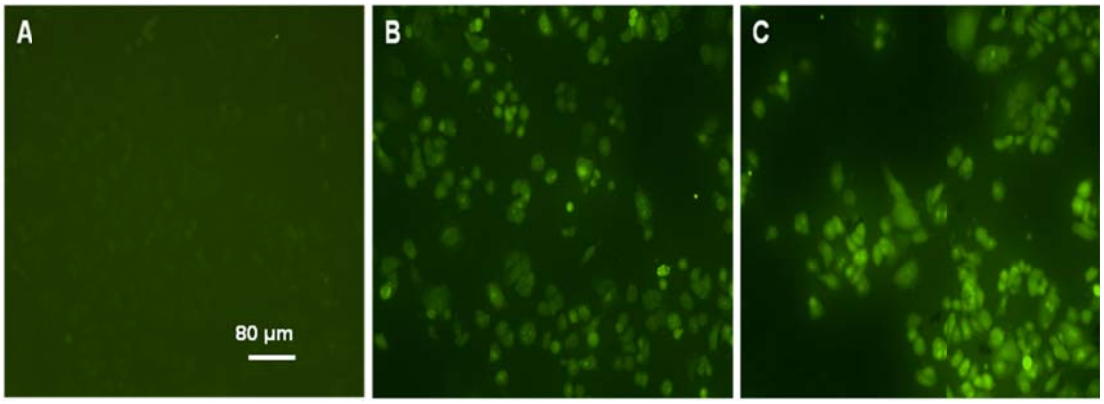

Figure 3-8: Cell uptake studies using gold nanorods conjugated to fluorescently labeled peptide. A. 15 min B. 1 h and C. 6 h incubation times**.**

3.3.3 Specificity, Light Scattering and Photo thermal therapy using protein coated nanorods (GNR-pVIII) on mammalian cells:

In vitro evaluation was performed to demonstrate the target specificity, imaging and photo thermal destruction of our novel protein nanoconjugates. Three different cell lines namely SKBR-3 cells, MCF-10A cells and fibroblast cells were incubated with nanoconjugates and the specificity was tested using indirect fluorescent labeling against phage protein present in the nanohybrid. As the GNR-pVIII has phage protein, we hypothesized mammalian binding to these nanoconjguates can be labeled with anti pVIII antibody. All the cells were counterstained with DAPI. From the fluorescence immune labeling (as shown in Figure 3-9), the binding of protein nanoconjugates (GNR-pVIII) to the target SKBR-3 cells is remarkably different to that of other control normal breast cells (MCF-10A) and fibroblast. This confirms the binding of our novel nanoconjugates to target SKBR-3 breast cancer cells.

Dark -field microscopy is used to analyze the light scattering of nanoconjugates from target and control cell lines. In this method, a narrow beam of white light is passed through the samples. Previous studies show different nanoparticles scatter different colored light under dark field based on their size and shape [190] . Because of the presence of strong longitudinal surface Plasmon oscillation with a frequency in the NIR region, protein-nanoconjugates exhibit strong light scattering in target SKBR-3 cells as expected (Figure 3-10). The high scattering in Figure 3-10 is correlated with areas containing gold nanorods. By contrast, control normal breast cells (MCF-10a) and

fibroblast showed little or no light scattering from gold nanorods. As the protein bound on the nanorod surface is specific to SKBR-3 cells, we believe protein coated nanorods bind specifically to target SKBR-3 breast cancer cells and gave them a distinguished back scattering from other control cells. This confirms the use of our nanoconjugates for imaging applications.

Previous studies showed that gold nanorods can act as strong photo thermal absorbers for destroying harmful cells. In order to test the cell destruction ability, the cells were incubated with nanorods which exhibited characteristic SPR absorbance band around 808nm and exposed to near infra red (NIR) radiations using 808nm laser radiations. Here, the target and the control cells were incubated with various nanoconjugates for 30 min and are exposed to different laser powers for 5 min, and the viability of the cells was verified using fluorescence microscope. Our optimized conditions showed exposure to laser at 808nm and 0.079 W/cm^2 power density in the presence of GNR-pVIII caused photo destruction of target cancer cells alone and no significant death is observed in control cells as detected by live/dead cell viability kit as shown in Figure 3-11. Increasing the power to 20 W/cm^2 resulted in the death of target as well as normal cells. Thus, by conjugating nanorods with phage protein that can selectively bind to target malignant cells, the cells can be photo thermally destroyed with very less energy than required to kill the normal health cells. Further quantitative analysis revealed around 60% of the target cells are dead when treated with protein

nanoconjugates. Together these results support the applications of our phage protein coated nanoconjugates for target specificity, imaging and therapy of breast cancer cells.

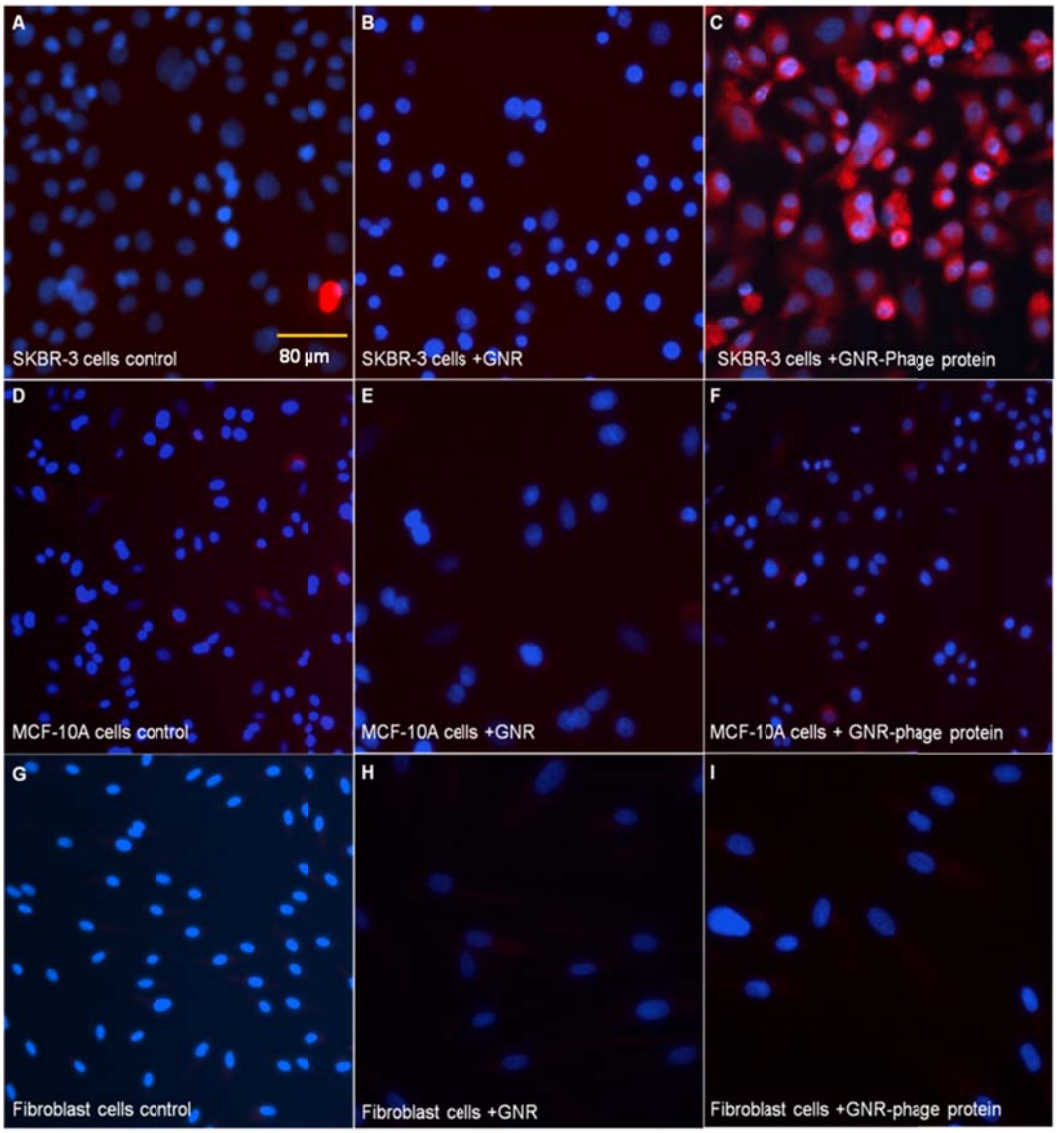

Figure 3-9: Specificity of protein-nanoconjugates using fluorescence studies. All the target and control cells were labeled with anti pVIII antibody and IgG conjugated rhodamine and cell nuclei was labeled with DAPI images at 20 x objectives.

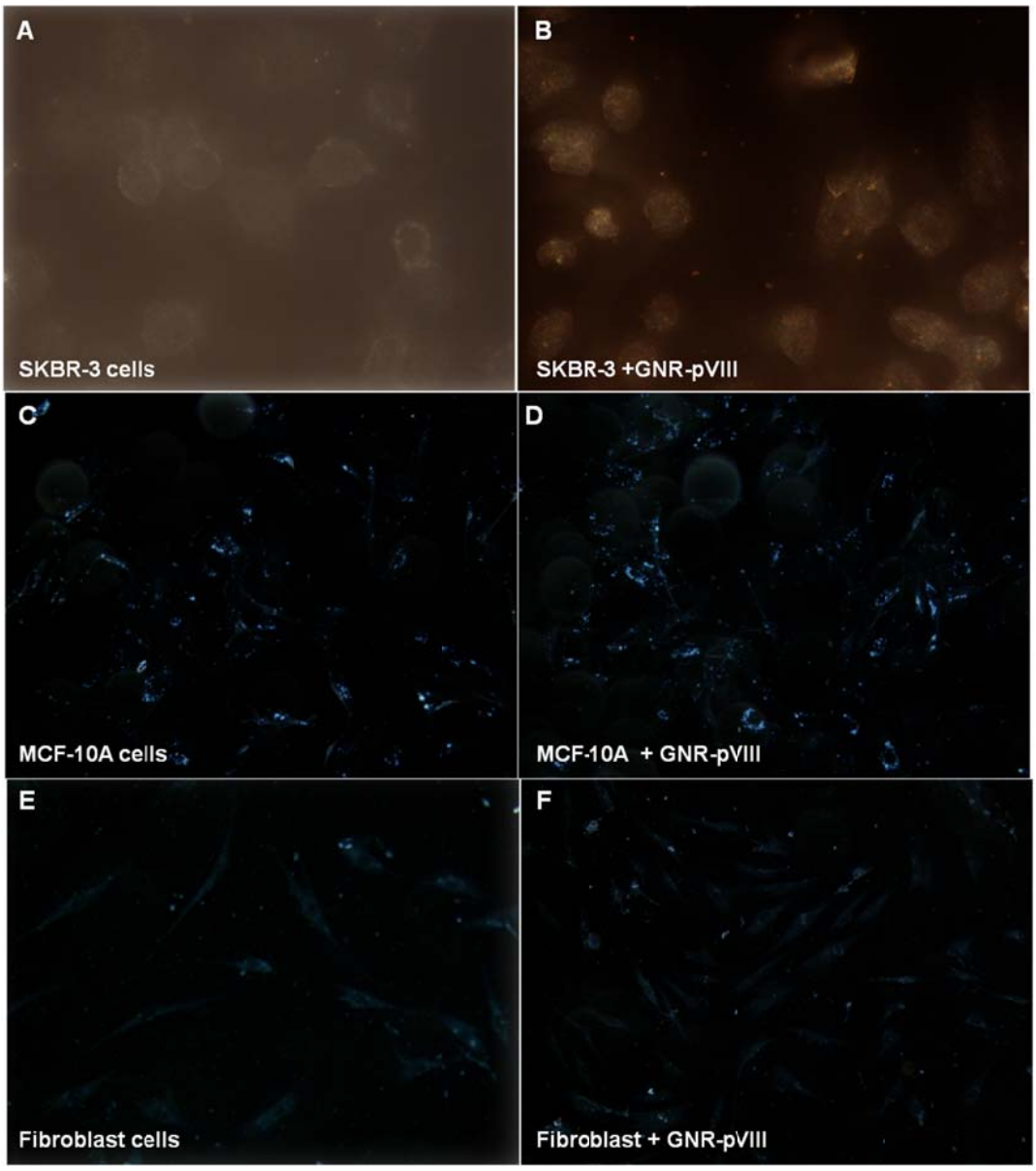

Figure 3-10: Light scattering of protein-nanoconjugates using dark field microscscope. All the target and control cells were exposed to a beam of white light and images were obtained at 20 x objectives.

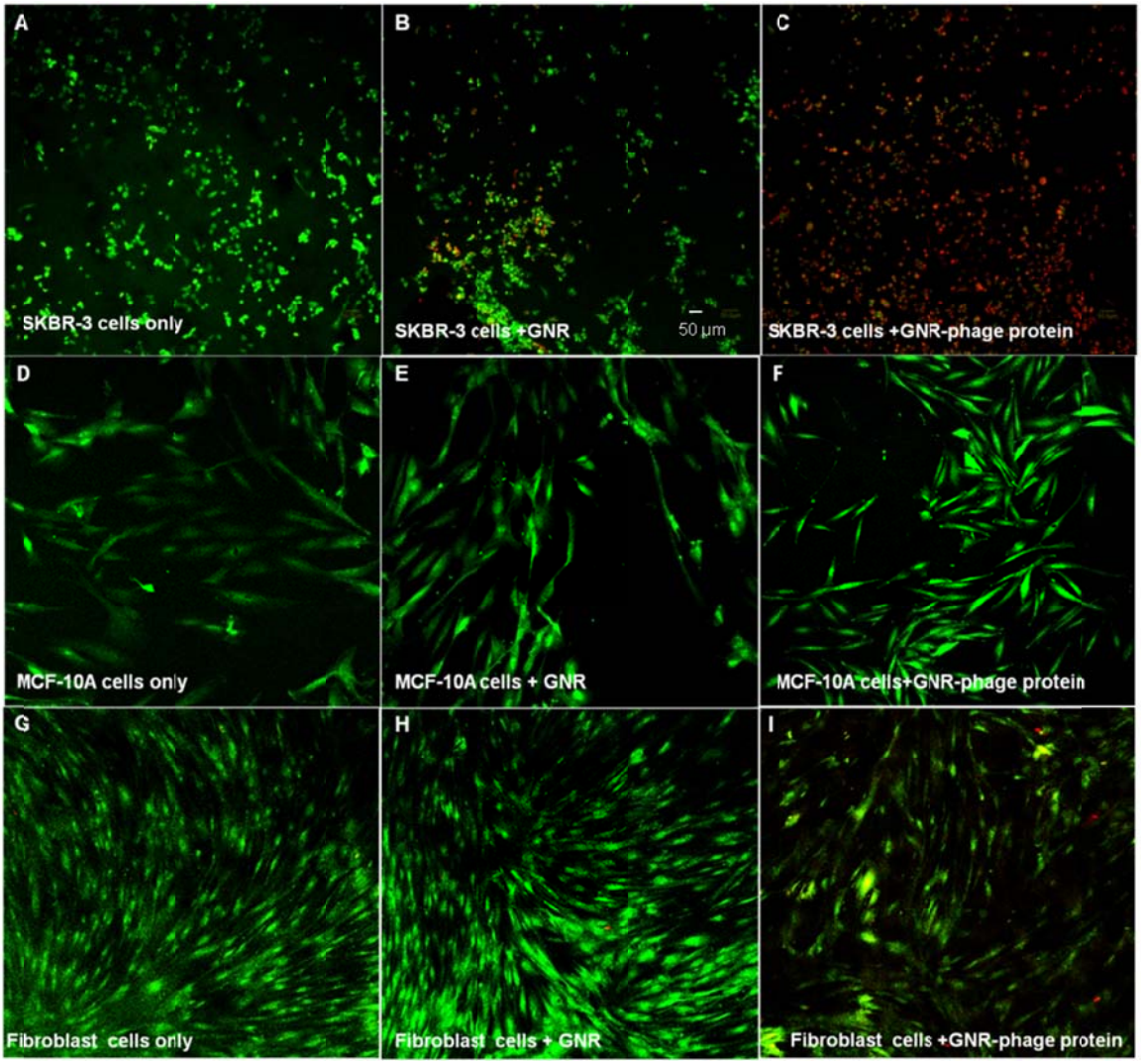

Figure 3-11: Photo thermal destruction studies of protein-nanoconjugates using Live/Dead cell viability kit. All the target and control cells were exposed to 808 nm for 5 min at a power density of 0. 079 W/Cm^2.

3.3.4 Cell behavior using video microscopy:

In order to explore the morphological changes during GNR-pVIII uptake into target SKBR-3 cancer cells, we performed live cell video imaging. Interestingly, we observed significant changes in the membrane ruffling when unmodified gold nanorods were incubated with SKBR-3 cells (Figure 3-12). However, such drastic changes are not observed when protein coated nanorods (GNR-pVIII) are incubated with target cells (Figure 3-13). Unlike significant membrane retraction towards the center in case of GNR alone treated cells, we observed SKBR-3 cells are sufficed to induce membrane ruffling during protein coated nanorods incubation which might indicates the cellular response is mediated through cytoskeleton. GNR-pVIII showed minimal abrupt cell changes when compared to GNR alone treatment where active cells are withdrawing their contacts with neighbouring cells and in some places the cells are rounding up. This may be due to the cytotoxicity of the CTAB present around GNR, where as such behavior is not observed in GNR-pVIII treated SKBR-3 cells. Since majority of live cells treated with GNR-pVIII studied by digital videomicroscopy showed increased activity at their edges, we believe that GNR-pVIII are taken into the SKBR-3 cells using actin mediated endocytosis. Our lab is currently performing more detailed research to understand the cell biology aspects during GNR-pVIII treatment.

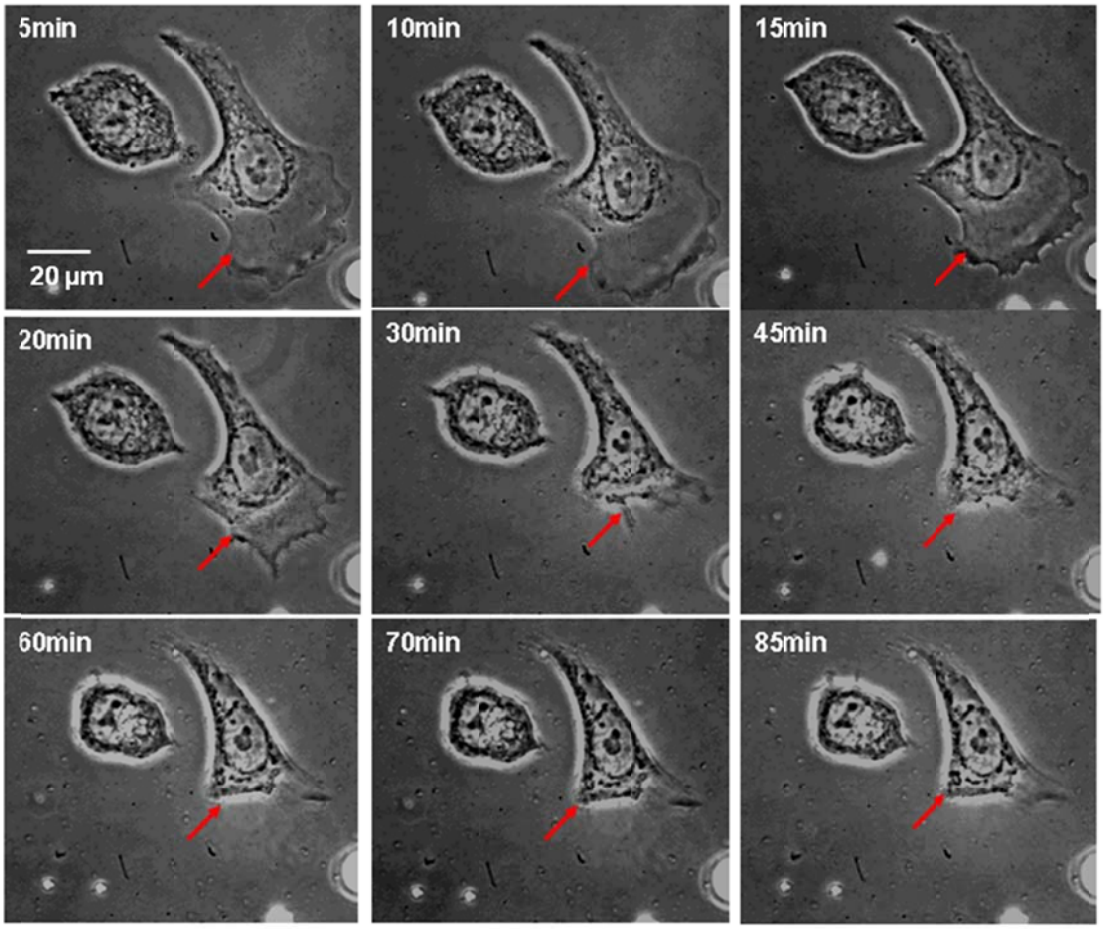

Figure 3-12: Video microscopy imaging of SKBR-3 cells incubated with Goldnanorods (GNRs) alone.

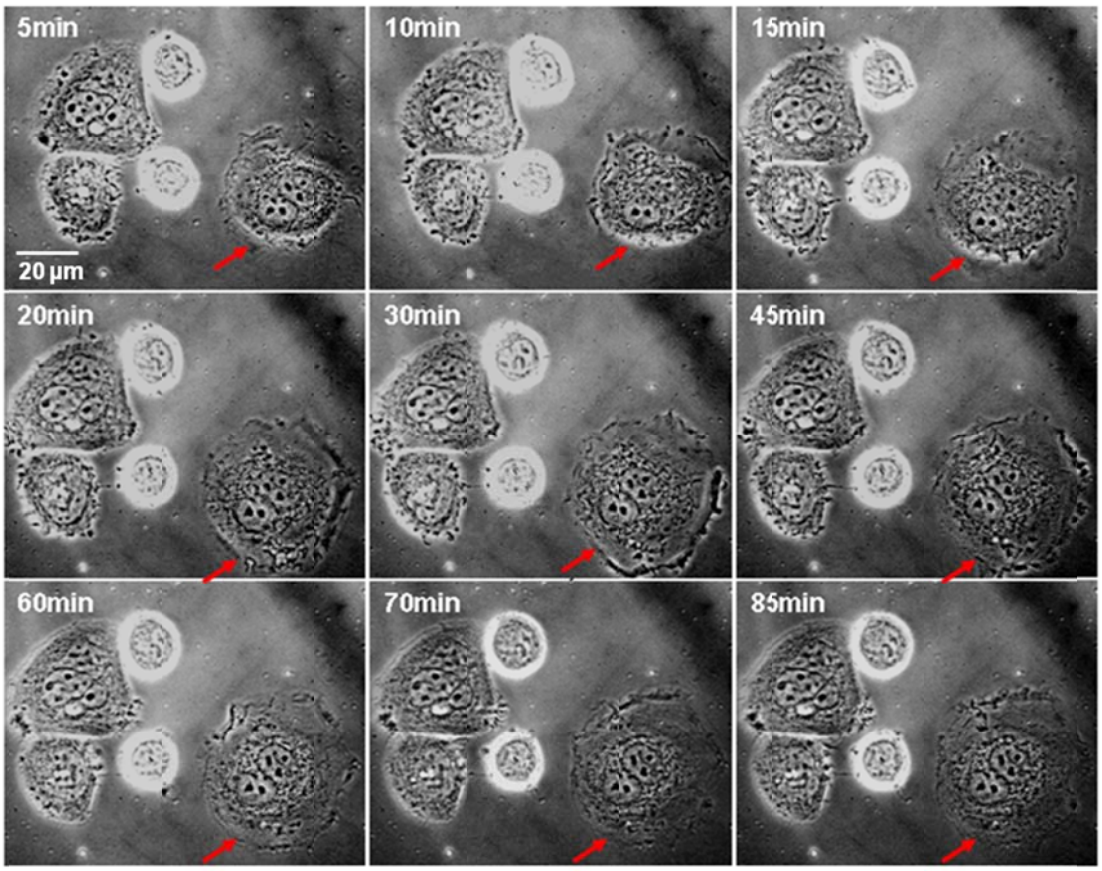

Figure 3-13: Video microscopy imaging of SKBR-3 cells incubated with Gold nanorods coated with phage protein (GNR-pVIII).

3.3.5 Gene expression analysis

In order to explore the cascade of the molecular interactions during GNR-pVIII entry into our model SKBR-3 cells, we compared the transcriptional profile of untreated SKBR-3 cells with cells treated with GNR-pVIII [Figure 3-15A and Table 3-1 & 3-2]. Analysis of >48,000 genes from Illumina WG-6_v3 microarrays identified 70 upregulated and 26 downregulated genes in the GNR-pVIII treated cells.

Lysosome activation, heparin binding, and response to inorganic substances were the most significant ontologies affected by GNR-pVIII internalization (Table 3-3). Heparin binding may represent the main mechanism by which cells recognize phage peptide bound to gold nanorods. Interestingly, Heparin-coating has been proposed as a non-toxic way of delivering nanoparticles into the cells [191, 192], reflecting our observations of non-cytotoxicity of GNR-pVIII. Heparin binding nanostructures have been shown to promote growth of blood vessels [193], and ANG (angiogenin) was one of the genes upregulated by GNR-pVIII treatment. Best known for its angiogenesis-promoting properties, it also possesses heparin- and actin binding activity. Once bound, angiogenin is endocytosed and translocated to the nucleus, thereby promoting the endothelial invasiveness. Angiogenin activation may indicate increased endothelial permeability upon GNR-pVIII treatment and enhanced GNR-pVIII delivery as a consequence. VTN (vitronectin) is another heparin binding, cell adhesion and spreading factor found in serum and tissues. Vitronectin interact with glycosaminoglycans and proteoglycans and is recognized by certain members of the integrin family and serves as a cell-to-substrate adhesion molecule. As such, it may act in concert with angiogenin in GNR-pVIII internalization process. Another gene in this category, APOE (apolipoprotein E), has been found to mediate binding, internalization, and catabolism of lipoprotein and nanoparticles [194]. APOE was present in another category; response to inorganic Substance, along with OLR1 (oxidized low density lipoprotein (lectin-like) receptor 1). OLR1 is a receptor that mediates the recognition, internalization and degradation of

oxidatively modified low density lipoprotein (oxLDL) by vascular endothelial cells. These molecules appeared in a single network of genes affected by GNR-pVIII (Figure 3-15B), and appeared as main sensors for GNR-pVIII recognition and internalization via binding to heparin-like gylcosaminoglycans.

The most significant ontology represented by four genes was Lysosome. Activation of lysosomes membrane-limited organelles responsible for degradation of macromolecules has been observed upon cell exposure to nanoassemblies [195, 196]. We hypothesize that activation of lysosomes may represent cellular attempt to degrade internalized GNR-pVIII.

Antigen Presentation Pathway was the most significant canonical pathway affected by GNR-pVIII internalization, followed by Neuregulin Signaling and Virus Entry via Endocytosis (Table 3-4). Since GNR-pVIII contain bacteriophage peptide it was not surprising that Antigen Presentation Pathway and endocytotic virus entry were the most overrepresented. Specifically, two members of Major histocompatibility complex (MHC) class I molecules (HLA-A and HLA-K) were highly upregulated upon GNR-pVIII treatment, with other members being upregulated slightly below the threshold for statistical significance. Interestingly, no change in expression of MHC class II molecules was observed, implying that target cells act as non-professional antigen presenting cells upon GNR-pVIII exposure. MHC class I molecules present degradation products derived from intracellular proteins in the cytosol. Harnessing this pathway has been proposed as a method of delivery of cancer vaccines using nanoparticles [197].

Activation of MHC class I signaling through HLA-A and HLA-K receptors appeared to complement aforementioned lysosome activity and processing of internalized GNR-pVIII.

Some intracellular or viral proteins, as well as nanoparticles, are processed by a proteasome [198] whose members include proteasome subunit, beta type, 8 (PSMB8, aka large multifunctional peptidase 7), and upregulated in response to GNR-pVIII. The activated proteasomes are translocated into the endoplasmic reticulum by the transporter associated with antigen processing (TAP). Both TAP1 and TAP2 were also upregulated in response to GNR-pVIII. An essential function of a modified proteasome, the immunoproteasome, is the processing of class I MHC peptides. This suggest that MHC class I molecules may be responsible for recognition of GNR-pVIII within a cell via proteasome-mediated processing.

A prominent group of seven members of G antigen family of genes were identified as upregulated by GNR-pVIII treatment. These molecules by their antigen nature appeared to fit to the picture of MHC class I signaling, but were excluded from the analysis due to lack of annotation. G antigens may represent a unique mechanism of non-cytotoxic GNR-pVIII recognition by cells and currently are under investigation in our lab.

Neuregulins are members of EGF family of growth factors and are ligands for the ErbB receptors. Since SKRB-3 cells express receptors for epidermal growth factors [199] and selection of peptide for nanoconjugate construction was performed with high

affinity to these receptors up regulation of neuregulin signaling appeared as a logical part in SKRB-3 cell line treated with GNR-pVIII. The major pathways involved in neuregulin's signal transduction include the Ras- and Shc-activated MAPK pathway, the PI3K-activated AKT pathway, the JAK/STAT pathway and the PLC-γ pathway, which ultimately affect cell proliferation and migration (both associated with tumorigenesis), adhesion, differentiation and apoptosis. These molecules appeared as parts of a single network built from up- and downregulated genes (Figure 3-15 B). This network highlights APOE-mediated signaling, activation of HLA-A and OLR1 receptors, upregulation of AKT complex and proteosomal parts integrated through IRS1 and LDL with kinase signaling. Interferon alpha connected signal transduction to the nucleus culminating in activation of STAT5A transcription factor and NFkB complex. Genes from lysosome (IFI27) and proteasome (PSMB8) ontologies were also regulated by Interferon alpha. Interestingly, although ErbB2 gene did not change its mRNA expression it was included in the network as another master regulator of the downstream signaling. Members of G antigen family were not present in the network due to lack of their interaction information.

Nanoassemblies similar to GNR-pVIII have been used to increase drug delivery into tumors. However, such delivery is often associated with cytotoxicity of normal cells [195]. The distinctive feature of GNR-pVIII is that no activation of cytotoxic pathways was observed. This makes GNR-pVIII an ideal model for imaging and targeted delivery of drugs into tumors.

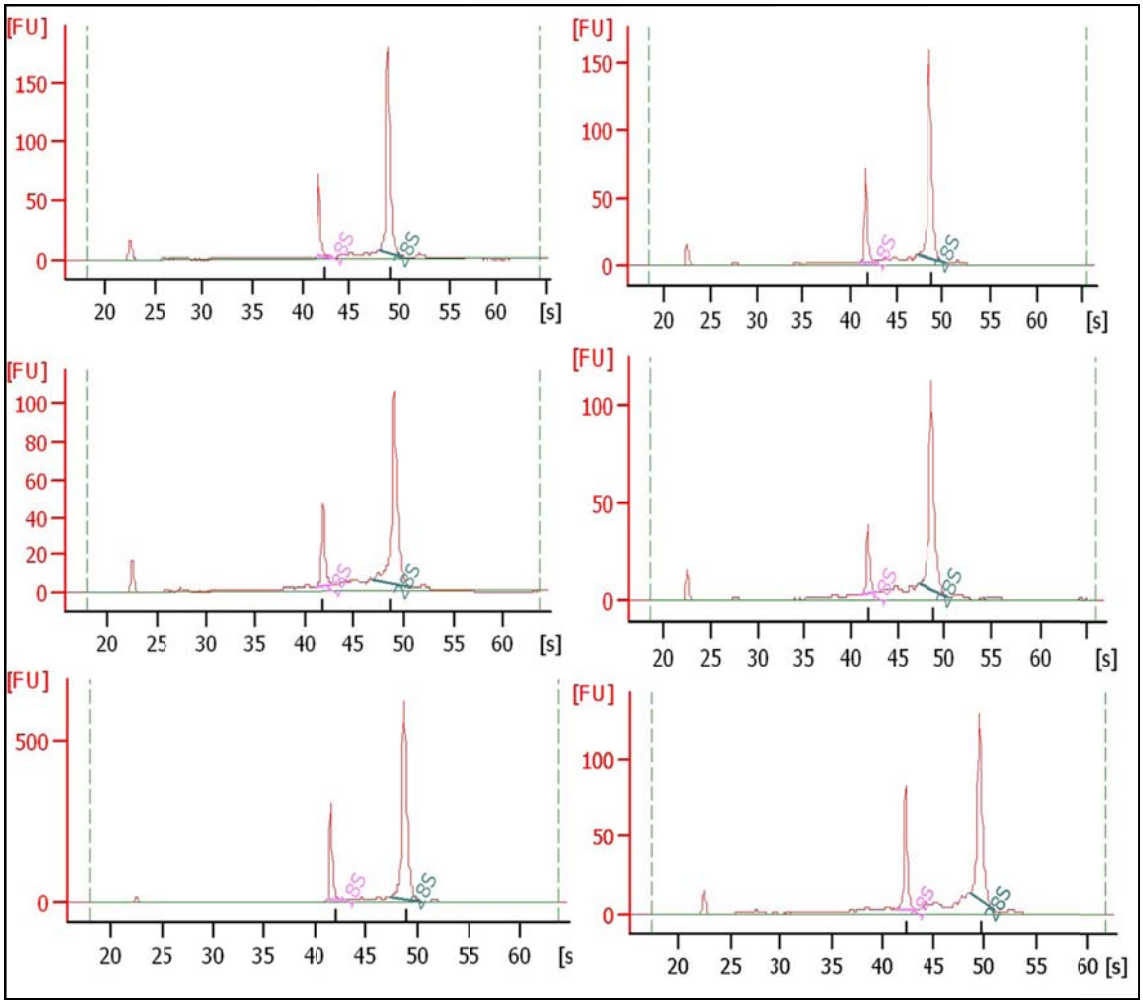

Figure 3-14: **Electropherograms obtained from capillary gel electrophoresis showing the quality of RNA used for microarray**. RNA isolated form untreated SKBR-3 cells (Left) and the RNA isolated from the GNR-pVIII treated SKBR-3 cells.

Table 3-1: **Genes downregulated in SKBR-3 cells in response to protein coated nanorods**

PROBE_ID	SYMBOL	DEFINITION
ILMN_1699217	C1orf96	chromosome 1 open reading frame 96 (C1orf96), mRNA.
ILMN_1713008	ABCC11	ATP-binding cassette, sub-family C (CFTR/MRP), member 11 (ABCC11), transcript variant 3, mRNA.
ILMN_1757347	C22orf9	chromosome 22 open reading frame 9 (C22orf9), transcript variant 1, mRNA.
ILMN_1684461	CADPS2	chromosome 3 open reading frame 57 (C3orf57), mRNA.
ILMN_1684461	CADPS2	Ca2+-dependent activator protein for secretion 2 (CADPS2), transcript variant 1, mRNA.
ILMN_1691566	CCDC140	coiled-coil domain containing 140 (CCDC140), mRNA.
ILMN_1669118	FUNDC2	FUN14 domain containing 2 (FUNDC2), mRNA.
ILMN_1684931	GPR119	G protein-coupled receptor 119 (GPR119), mRNA.
ILMN_1732071	HIST2H2BE	histone cluster 2, H2be (HIST2H2BE), mRNA.
ILMN_1687546	HSP90AA1	heat shock protein 90kDa alpha (cytosolic), class A member 1 (HSP90AA1), transcript variant 1, mRNA.
ILMN_1664861	ID1	inhibitor of DNA binding 1, dominant negative helix-loop-helix protein (ID1), transcript variant 2, mRNA.
ILMN_1663991	LOC387885	PREDICTED: similar to hCG1652305 (LOC387885), mRNA.
ILMN_1712347	LOC644422	PREDICTED: misc_RNA (LOC644422), miscRNA.
ILMN_1732776	NUP98	nucleoporin 98kDa (NUP98), transcript variant 1, mRNA.
ILMN_1652819	OPA3	optic atrophy 3 (autosomal recessive, with chorea and spastic paraplegia) (OPA3), transcript variant 2, mRNA.
ILMN_1810181	PCGF6	polycomb group ring finger 6 (PCGF6), transcript variant 1, mRNA.
ILMN_1795930	PTGER4	prostaglandin E receptor 4 (subtype EP4) (PTGER4), mRNA.
ILMN_1691048	SLC22A18AS	solute carrier family 22 (organic cation transporter), member 18 antisense (SLC22A18AS), mRNA.
ILMN_1811387	TFF3	trefoil factor 3 (intestinal) (TFF3), mRNA.
ILMN_2068122	TMEM65	transmembrane protein 65 (TMEM65), mRNA.
ILMN_2371685	UBE2E1	ubiquitin-conjugating enzyme E2E 1 (UBC4/5 homolog, yeast) (UBE2E1), transcript variant 1, mRNA.

Table 3-2: Genes up-regulated in SKBR-3 cells in response to protein coated nanorods

PROBE_ID	SYMBOL	DEFINITION
ILMN_1740938	**APOE**	apolipoprotein E (APOE).
ILMN_1726388	**ACBD7**	PREDICTED: acyl-Coenzyme A binding domain containing 7 (ACBD7).
ILMN_1760727	**ANG**	angiogenin, ribonuclease, RNase A family, 5 (ANG), transcript variant 2
ILMN_1780170	**APOD**	apolipoprotein D (APOD).
ILMN_1782057	**ATP8B2**	ATPase, class I, type 8B, member 2 (ATP8B2), transcript variant 1.
ILMN_1712608	**BFSP1**	beaded filament structural protein 1, filensin (BFSP1).
ILMN_1723480	**BST2**	bone marrow stromal cell antigen 2 (BST2).
ILMN_1772074	**C19orf51**	chromosome 19 open reading frame 51 (C19orf51).
ILMN_1733288	**C1RL**	complement component 1, r subcomponent-like (C1RL).
ILMN_1689585	**C20orf194**	chromosome 20 open reading frame 194 (C20orf194).
ILMN_1806488	**CCDC108**	coiled-coil domain containing 108 (CCDC108), transcript variant 1.
ILMN_1758778	**CEP110**	centrosomal protein 110kDa (CEP110).
ILMN_1696537	**DDIT4L**	DNA-damage-inducible transcript 4-like (DDIT4L
ILMN_1669376	**DRAM**	damage-regulated autophagy modulator (DRAM).
ILMN_1705035	**FBXL7**	F-box and leucine-rich repeat protein 7 (FBXL7).
ILMN_1778144	**FLJ20489**	hypothetical protein FLJ20489 (FLJ20489).
ILMN_1671482	**GALM**	galactose mutarotase (aldose 1-epimerase) (GALM).
ILMN_1671054	**HLA-A**	major histocompatibility complex, class I, A (HLA-A).
ILMN_2203950	**HLA-A**	major histocompatibility complex, class I, A (HLA-A).
ILMN_2165753	**HLA-A29.1**	major histocompatibility complex class I HLA-A29.1 (HLA-A29.1)
ILMN_2092850	**HPSE**	heparanase (HPSE).
ILMN_1766499	**HSPA2**	heat shock 70kDa protein 2 (HSPA2).
ILMN_2058782	**IFI27**	interferon, alpha-inducible protein 27 (IFI27).
ILMN_1784178	**IFT172**	intraflagellar transport 172 homolog (Chlamydomonas) (IFT172).
ILMN_2334296	**IL18BP**	interleukin 18 binding protein (IL18BP), transcript variant A.
ILMN_1759232	**IRS1**	insulin receptor substrate 1 (IRS1).
ILMN_1702385	**LILRA4**	leukocyte immunoglobulin-like receptor, subfamily A (with TM domain), member 4

ILMN_1767665	**LOC493869**	similar to RIKEN cDNA 2310016C16 (LOC493869).
ILMN_1674097	**LOC645037**	similar to GAGE-2 protein (G antigen 2) (LOC645037).
ILMN_1674710	**LOC647784**	PREDICTED: hypothetical protein LOC647784, transcript variant 1.
ILMN_2391891	**MAP2K5**	mitogen-activated protein kinase kinase 5 (MAP2K5), transcript variant A.
ILMN_2071809	**MGP**	matrix Gla protein (MGP).
ILMN_1653278	**MUC20**	mucin 20, cell surface associated (MUC20), transcript variant S.
ILMN_2370091	**NGFRAP1**	nerve growth factor receptor (TNFRSF16) associated protein 1
ILMN_2347592	**NMB**	neuromedin B (NMB), transcript variant 1.
ILMN_1757019	**NTN4**	netrin 4 (NTN4).
ILMN_1723035	**OLR1**	oxidized low density lipoprotein (lectin-like) receptor 1 (OLR1).
ILMN_1790106	**PLP1**	proteolipid protein 1 (Pelizaeus-Merzbacher disease, spastic paraplegia 2, uncomplicated) (PLP1), transcript variant 2.
ILMN_1787509	**PRIC285**	peroxisomal proliferator-activated receptor A interacting complex 285 (PRIC285), transcript variant 2.
ILMN_1771538	**PSCA**	prostate stem cell antigen (PSCA).
ILMN_1767006	**PSMB8**	proteasome (prosome, macropain) subunit, beta type, 8 (large multifunctional peptidase 7) (PSMB8), transcript variant 2.
ILMN_2390299	**PSMB8**	proteasome (prosome, macropain) subunit, beta type, 8 (large multifunctional peptidase 7) (PSMB8), transcript variant 1.
ILMN_1713829	**PTGES**	prostaglandin E synthase (PTGES).
ILMN_2042771	**PTTG1**	pituitary tumor-transforming 1 (PTTG1).
ILMN_1709795	**RAC2**	ras-related C3 botulinum toxin substrate 2 (rho family, small GTP binding protein Rac2) (RAC2).
ILMN_1701613	**RARRES3**	retinoic acid receptor responder (tazarotene induced) 3 (RARRES3).
ILMN_1709683	**RASSF2**	Ras association (RalGDS/AF-6) domain family 2 (RASSF2), transcript variant 2.
ILMN_1654398	**RGL1**	ral guanine nucleotide dissociation stimulator-like 1 (RGL1).
ILMN_1753547	**STAT5A**	signal transducer and activator of transcription 5A (STAT5A).
ILMN_1804663	**THBS3**	thrombospondin 3 (THBS3).
ILMN_1741768	**TMPRSS3**	transmembrane protease, serine 3 (TMPRSS3), transcript variant D.
ILMN_1809842	**TNNC1**	troponin C type 1 (slow) (TNNC1).
ILMN_1782295	**TRPC4**	transient receptor potential cation channel, subfamily C, member 4 (TRPC4).
ILMN_1747546	**TSPAN1**	tetraspanin 1 (TSPAN1).
ILMN_1657554	**TSPYL2**	TSPY-like 2 (TSPYL2).
ILMN_1691127	**VTN**	vitronectin (VTN).

ILMN_1800317	**WNT5A**	wingless-type MMTV integration site family, member 5A (WNT5A).
ILMN_1771093	**ZNF414**	zinc finger protein 414 (ZNF414).
ILMN_1836309		PREDICTED: LOC440151 (LOC440151)

Table 3-3: Overrepresented functions among upregulated genes in protein coated nanorods treated SKBR-3 cells.

Functional category	**Molecules**	**p-value**
Lysosome	IFI27, DRAM, TSPAN1, SLC48A1	0.009
Heparin binding	ANG, APOE, VTN	0.032
Response to inorganic substance	APOE, MGP, OLR1, TNNC1	0.028

Table 3-4. Genes and canonical pathways overrepresented in protein coated nanorods treated cells. Bold highlights up regulated genes, regular font marks down regulated genes.

Canonical Pathways	**Molecules**	**p-value**
Antigen Presentation Pathway	**HLA-K, HLA-A, PSMB8**	0.0005
Neuregulin Signaling	**RAC2, STAT5A,** HSP90AA1	0.0071
Virus Entry via Endocytic Pathways	**RAC2, HLA-A**	0.05

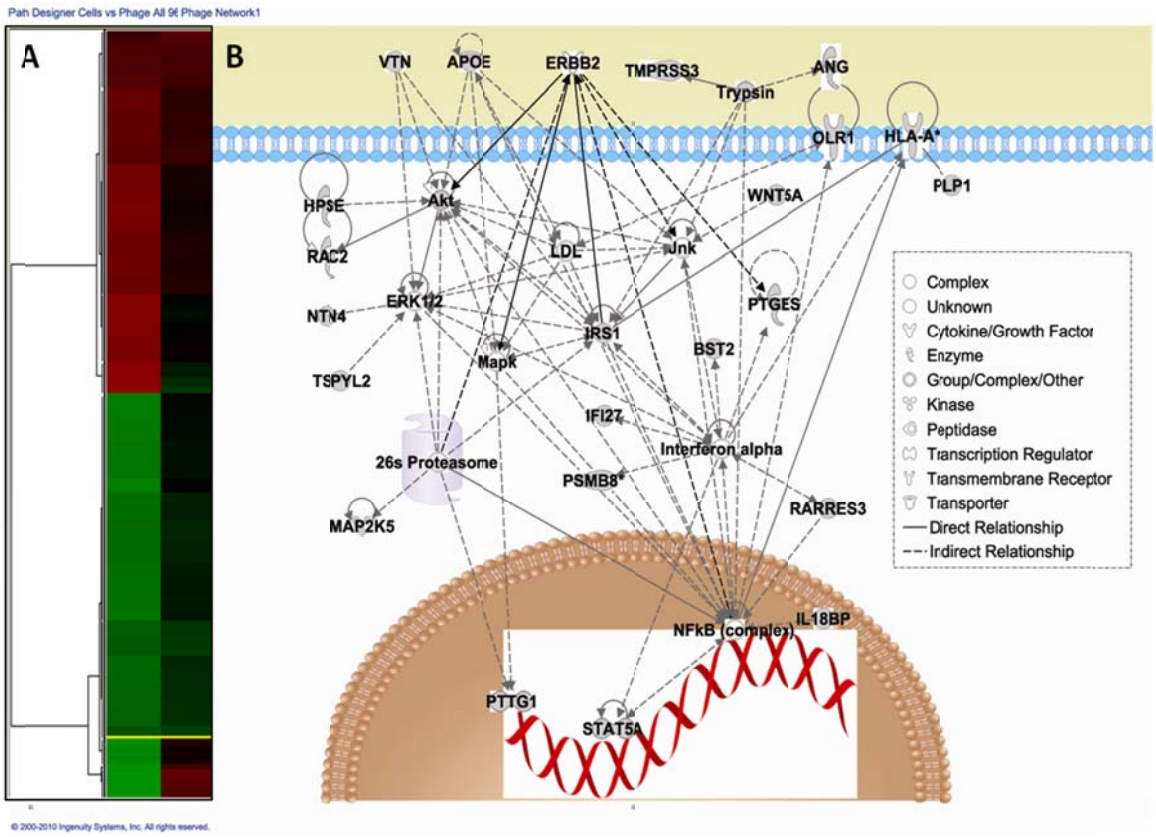

Figure 3-15: Model of protein-nanoconjugates (GNR-pVIII) internalization into SKBR-3 cells. A. Heat map of untreated (left) and GNR-pVIII treated (right) SKBR-3 cells. B. Molecular interactions among the genes in SKBR-3 cells treated with GNR-pVIII.

3.3.6 In vivo tumor development and specificity experiments

As the nude mouse is deficient in thymus, it is able to take the epithelial cells from human origin. Thus, SKBR-3 epithelial breast cancer cells are injected into nude mice and a tumor model is developed. The developed tumor is physically and microscopically characterized. As shown in Figure 3-16 (A, B) the nude mice before and after tumor development is physically verified. The size of the tumor is measured using a digital caliper. In order to further confirm the pathological condition of the tumor, it is excised and sent for immune histology staining. Figure 3-17 (A, B) shows the typical H&E staining of tumor tissue at low and high magnifications. Appearance of dark granules (hetero chromatin staining) confirms the presence of tumor.

In order to perform the specificity experiments, three nude mice with tumors are injected with PBS, GNR, and GNR-pVIII separately and allowed to circulate for 24 hrs. Later, the tumor is excised and immunolabeled with dye labeled anti pVIII antibody. We hypothesized phage protein that has specificity to *in vitro* cells may also be specific in the *in vivo* environment. So, we labeled tumor tissue with rhodamine conjugated antibody and DAPI is used as a nuclear counter stain. As expected Figure 3-18 (C) shows the tumor is successfully labeled with anti pVIII antibody in GNR-pVIII treated mice where as in the controls Figure 3-18 (A,B) no characteristic labeling is observed. This confirms the feasibility of *in vivo* specificity experiments. The *in vivo* imaging and photo thermal abilities are yet to be examined.

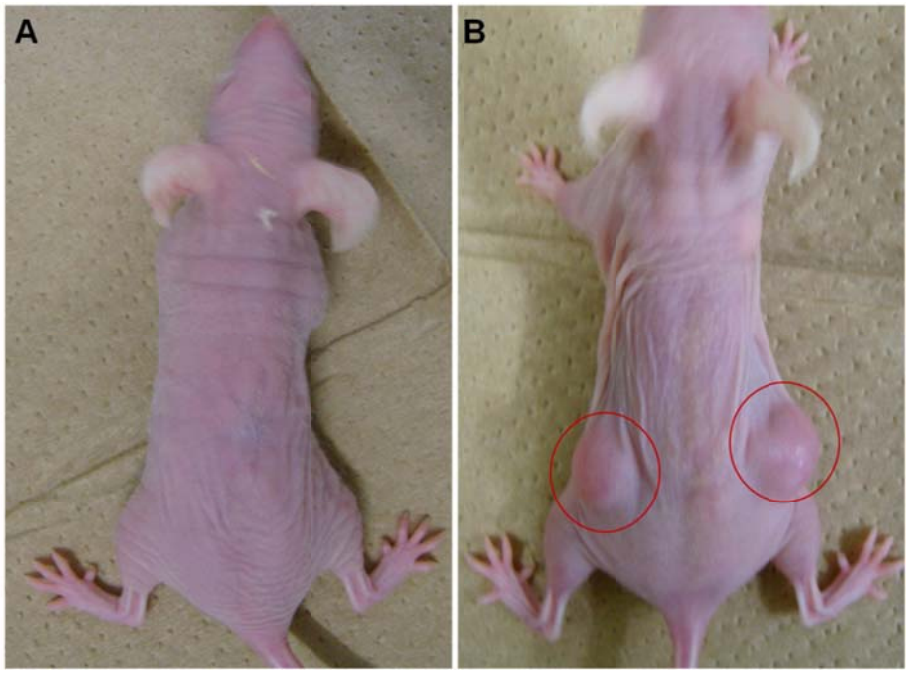

Figure 3-16: **Development of In vivo SKBR-3 nude mice tumor model.**

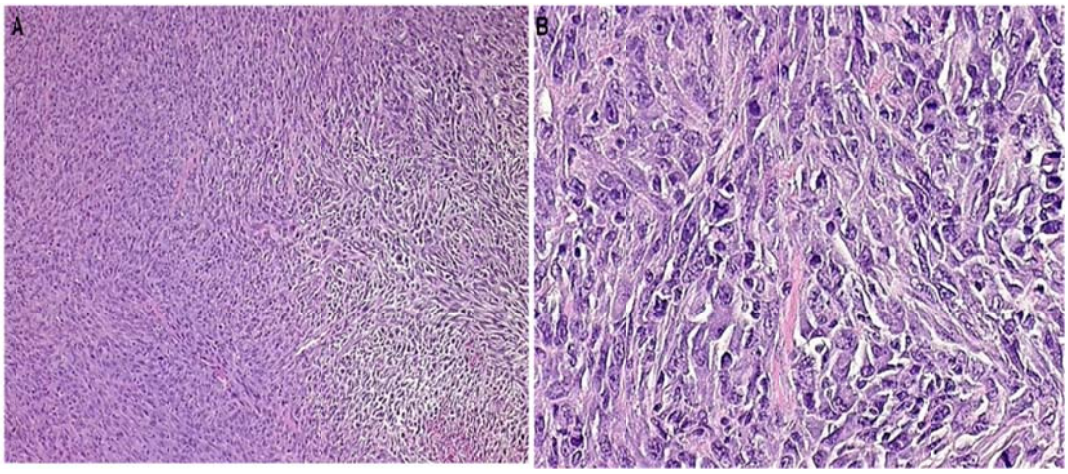

Figure 3-17: **H&E staining of developed breast tumor** A. low magnification (5x)

B. High magnification (20x).

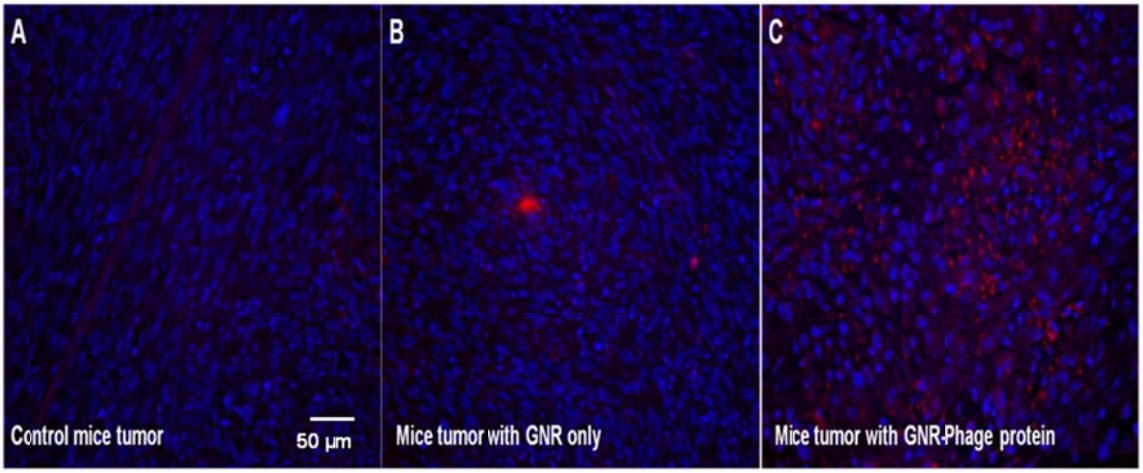

Figure 3-18: **Specificity of nanoconjugates in tumor bearing nude mice model** A. Control tumor mice with PBS injection. B. Mice injected with GNR in PBS. C. Mice injected with GNR-Phage protein in PBS.

3.4 Discussion

Recently photo thermal therapy (PTT) involving deep penetrating near infra red (NIR) radiations has emerged as a promising treatment modality because of its ability to deliver lethal dose of heat at the target site. In order to achieve desired thermal effect at the target site, we need a suitable vector with two important capabilities one exogenous NIR absorbing ability and second, receptor specific targeting moiety. Currently antibodies confer great specificity as targeting moieties for photothermal therapy [200]. However, antibodies are limited by their large size, cost of production and inherent ability to bind to components of reticuloendothelial system [171].

Thus, here we developed a new exogenous absorbing agent with phage protein as a substitute to antibody. We have previously demonstrated that landscape phage displaying VSSTQDFP motifs binds to SKBR-3 cells with high affinity and frequency [179]. Our data also suggested that using multivalent phage libraries considerably increases the repertoire of available cell-internalizing ligands with potential applications in targeted drug delivery, imaging, molecular monitoring and profiling of breast cancer cells. As the affinity selection using phage libraries results in identifying phage and peptide ligands that strongly and specifically bind to a target receptor, we hypothesized the isolation of major coat proteins from the selected phage should theoretically retains the target binding capabilities. On the basis of this hypothesis, we designed and synthesized novel GNR-pVIII conjugates know as hybrid nanoprobes by integrating phage display technology and nanosynthesis. Our results provide compelling evidence to show the feasibility of our new design. Accordingly, when the isolated peptide is conjugated onto a photo active substrate such as gold, it can be used for imaging and therapy applications. The resulting novel nanomaterial is versatile as any phage protein specific to a target cell can be selected and conjugated to functionalized gold nanorods. This design confers the target specificity, imaging and destruction of our model SKBR-3 breast cancer cells.

Our results show that when SKBR-3 cells are incubated with GNR-pVIII at an optical density of 0.5, and a minimum NIR light dose of 0.079 W/cm^2 for 5 min with 0.3 cm spot size is required to destroy viable target cells leaving the control cells unharmed

and is in agreement with the previous studies [170]. The resulting cell death could be because of the increase in localized temperature due to thermal effect resulting from the accumulation of gold nanorods at the target site. As several earlier studies have discussed the optical properties of gold including imaging and its mechanism of action at the target site upon NIR radiations [201] , here we limit our discussion to GNR-pVIII effect at the gene level.

In order to understand the cell biological aspects and the gene expression levels, we performed video microscopy and microarray experiments respectively. From our video microscopy experiments we can clearly see that the SKBR-3 cells undergo rapid membrane ruffling which might indicate the global nature of cellular response mediate through cytoskeleton. Interestingly, when SKBR-3 cells are incubated with unmodified gold nanorods, we observed most of the cells are withdrawing their membrane ruffling towards its center leading to cell shrinkage. However, when cells are incubated with protein coated gold nanorods no such behavior is observed. One possible reason for such morphological changes observed could be due to the presence of cytotoxic CTAB molecules on the surface of gold nanorods. In case of GNR-pVIII conjugate, the surface of CTAB is completely modified with polymer and protein decreasing its cytotoxic effects on cells.

Based on our microarray data, we hypothesize GNR-pVIII are binding to heparin-like gylcosaminoglycans, and activate endocytotic entry pathways predominantly by lysosomes. This in turn activates Antigen presentation pathway for their internalization

and processing by immunoproteasomes. The expression of few genes from the network namely APOE, HLA-A and GAGE-121 were further verified using real time PCR. In summary, we hypothesize recognition of GNR-pVIII by cells via heparin-like binding to several receptors, including ErbB2, APOE and OLR1, and its internalization via endocytotic mechanism. Degradation of GNR-pVIII via lysosomal and proteosomal mechanisms was accompanied by activation of immune response utilizing MHC class I and G antigen family of genes. Therefore, selective GNR-pVIII entry into target cells allows their destruction not only via photoactivation of the nanorods but also by recognition of processed peptides by cytotoxic T-cells. Temporal profiling of cellular changes in gene expression upon GNR-pVIII exposure will help to answer exact sequence of the described events. Our lab is currently investigating the molecular level interaction using additional controls such as only gold nanorods, nanorods coated with PEG and only phage protein.

Although, these novel nanomaterials are yet to be optimized for maximum efficiency, the ability to control the loading of phage proteins on the surface of functionalized nanorods have allowed us to synthesize new nanomaterials that make them attractive candidates for medical applications. Similar to the conjugation of oligonucleotide on the surface of gold nanoparticles [202], these novel nanovectors can enhance target specificity and allow us to add different functionalities on the nanoparticle surface.

Chapter 4 : Other Biomedical applications of phage protein and genetically engineered filamentous bacteriophage in nanoscience.

4.1 Introduction

Mimicking the controlled assembly of complex biological structures such as viruses to modify nanomaterials holds great promise in this new era of molecular biomimetics. Carbon nanotubes (CNTs) continue to receive great attention due to their interesting chemical, physical, mechanical and electrical properties. These unique properties make them ideal candidates for the development of fuel cells [203], chemical sensors [204], catalysis [205], and targeted drug [206] and gene delivery vehicles [207]. The introduction and delivery of DNA, proteins, or drug molecules into living cells is important for therapeutics [208, 209]. Although some of the existing anticancer drugs are very potent, their efficacy is constrained not only by their systemic toxicity and narrow therapeutic window, but also as a result of drug resistance and limited cellular entry. For this reason, the development of more efficient delivery systems with an ability to enhance cellular uptake of existing potent drugs is essential.

Phage display has being extensively applied to develop nanotechnology [210], leading to the burgeoning of a new branch of science known as phage nanobiotechnology [211]. The filamentous bacteriophage can be genetically modified to display desired peptide or the evolutionary phage libraries can be used to select a target binding phage as

described in the previous chapter. The filamentous phage such as M13 or fd can be simply viewed as the assembly of coat proteins around a circular single-stranded DNA (ssDNA) as its genome. During such assembly process, the C-terminal end of the coat protein electrostatically interacts with the negatively charged ssDNA. While the N-terminal end of the coat protein is exposed to the environment and can be fused with a foreign peptide such as a cancer cell targeting peptide. Thus, the formation of the filamentous phage particle can be simplified as the assembly of pVIII along the ssDNA template through non-covalent interactions.

In this chapter we used three different examples to demonstrate the biomedical applications of filamentous bacteriophage. In one, we used the major coat protein of screened bacteriophage to demonstrate its assembly on functionalized carbon nanotubes. The assembly of virus protein displaying cancer cell receptor binding peptides around nanotubes allows the resultant nanoconjugates to bear cell-specific peptides on its surface for use in targeted drug and gene delivery and bio-imaging. In the other examples we used genetically modified phage as a template for conjugation with photo sensitizer for photo dynamic therapy (PDT) applications and for biomimetic assembly of liposomes for drug delivery applications.

In the first example, we used simple layer-by layer self assembly technique for the assembly of an oligonucleotide (ss-DNA) and fd bacteriophage major coat proteins onto polycationic polyethylenimine (PEI) functionalized multi-walled carbon nanotubes using non-covalent interactions. The fd virus major coat proteins used in this study was

previously screened using landscape phage libraries and is found to be specific to SKBR-3 breast cancer cells. We employed Fourier transform infrared spectroscopy, UV-Visible spectroscopy, transmission electron microscopy (TEM) and zeta potential analysis to confirm the serial assembly process.

Previous studies show preferential accumulation of photosensitizer in the target cancer cells followed by irradiation with appropriate wavelength of light will generate cytotoxic singlet oxygen that can eradicate the tumor tissue via apoptosis or necrosis [212]. This method is efficiently used to treat several cancers and other diseases [212]. The current disadvantage in using the photosensitizer is the lack of specificity against tumor cells. Hence, in our recent study, the SKBR-3 specific phage described in the earlier chapters is conjugated with porphyrin, pyropheophorbid-a (PPa) for the first time to form a novel phage-PPa complex [213]. The complex is characterized by TEM, UV-visible spectroscopy and the time resolved singlet oxygen measurements. The resulting phage-porphyrin complex has potential photodynamic therapy (PDT) application in target SKBR-3 breast cancer cells [213].

Liposomes are evolved as excellent drug delivery vehicles because of their central hydrophilic core and outer hydrophobic compartment [214]. The entrapment of drugs within the inner core makes it isolated from the surrounding environment. However, its gene/drug delivery and PDT applications are limited because of the instability of liposomes in biological medium and sensitivity to external environment (temperature and osmotic shock). In our study, we used a biomimetic approach to self-assemble the drug

loaded liposomes onto filamentous bacteriophage using electrostatic interactions [215] to increase their stability. As a proof of concept, the filamentous M13 bacteriophage is genetically modified to display eight glutamic acid residues and assembled with zinc phthalocyanine (ZnPc) loaded cationic liposomes. The resulting phage-liposome complex has potential PDT and drug delivery applications.

4.2 Experiments Performed

4.2.1 Genetic modification of bacteriophage surface with eight glutamic acid residues

Traditional phage display technology was used to introduce eight glutamic acid residues (E8) on the N terminus of the major coat protein (pVIII) of M13 bacteriophage. In this procedure, an oligonucleotide sequence that codes for eight glutamic acid residues is designed. The sequence of forwards and reverse primers is shown below: GLU1 (forward primer):

ATCCATGGGAAGAAGAAGAAGAAGAAGAAGAAGATCCCGCAAAAGCG

GLU2 (reverse primer): GCAATTTTATCAGCTTGCTTTCGAG

DNA containing the genes for eight glutamic acids was amplified by using the polymerase chain reaction (PCR). Here, we used M13 replicative form (RF) of DNA as template and oligonucleotides GLU1 and GLU2 as primers for PCR reaction. Once the PCR is completed, the products obtained are purified and isolated. The DNA fragment

was digested with Hind III and NCo1 restriction endonucleases and cloned into a phagemid that had been previously digested with same restriction enzymes. The phagemid permitted the display of eight glutamic acid residues on the N terminus of p8 protein. The incorporation of the oligonucleotide sequence into the phagemid was confirmed by DNA sequencing.

4.2.2 Purification of genetically filamentous bacteriophage

The SKBR-3 specific bacteriophage was purified by double polyethylene glycol (PEG) precipitation as described previously [216]. Briefly, 40 ml of NZY medium containing 20 µg/ml tetracycline was inoculated with a fresh single colony of phage-infected cells in a 250 ml flask. The culture was incubated under shaking at 37^0C and 200 rpm for overnight. Pour the overnight culture in a 250ml Beckman centrifuge bottle and centrifuged at 3000 g for 10 min at 4^oC. The supernatant was poured into a fresh tube and centrifuged at 12000 g for 10 min at 4^oC. The resultant cleared supernatant was again poured into a fresh tube, to which 6 ml PEG/NaCl solution (100 g PEG 8000, 116.9 g NaCl and 475 ml water) was then added. The tube was kept at 4^0C overnight for phage precipitation. The precipitated phages were collected by centrifugation at 31000 g for 15 min and the supernatant was removed. The pellet was then dissolved in 1 mL Tris buffered saline (TBS) in a micro-centrifuge tube and centrifuged again at 12000 g for 2 min to remove any non dissolved material. 150 µl PEG/NaCl solutions was added to the supernatant and kept on ice overnight. The tube was then centrifuged at 12000 g at 4^oC

for 10 min and the supernatant was removed. The pellet was dissolved in 200 µl double distilled water by vortexing. The concentration of phage was estimated using UV-visible spectrophotometer by measuring the absorbance at 269nm [217]. The eight glutamic acid residue-displayed phage (engineered phage) was obtained by incubating a phage suspension with Escherichia coli XL1 blue strain. To obtain the phage suspension, an overnight culture of E. coli XL1 blue cells was used. Two tubes of bacterial culture (5 mL) were incubated with phage in LB medium (1 L) on a shaking incubator at 37 8C. The overnight culture was first centrifuged at 2400 g for 10min at 4 8C with a Beckman Coulter high performance centrifuge, and the supernatant was collected and recentrifuged at 6700 g for 10 min at 4 8C. Then a solution of PEG and NaCl was added and the suspension was stored in refrigerator.

4.2.3 Purification of SKBR-3 specific phage protein

SKBR-3 targeting phage selected from f8/8 landscpe library is solubilized as described by [218]. The major coat protein was isolated as described in earlier chapter. Briefly, 5 ml of purified phage solution (1x 10^{14} virions/ml) was mixed with 10ml of 120mM cholate in 10mM Tris-HCl, 0.2mM EDTA, pH 8.0, and chloroform(2.5% v/v). The mixture was incubated for 1h at 37^{O}C with occasional stirring. The dissociated phage was then applied to a sepharose column and eluted with 10mM cholate in 10mM Tris-HCl/0.2 mM EDTA, pH 8.0, to separate the major coat proteins from the phage DNA. The various fractions at 1ml each was then collected and analyzed using a UV-Visible

nanophotometer. Fractions with an absorbance ratio of A280/A260 greater than 1.5 were stored at 4^{o}C for further use. The protein concentration was estimated using a Bradford assay and the purified protein was confirmed using 15% SDS-PAGE electrophoresis and western blotting.

4.2.4 Carbon nanotube functionalization with SKBR-3 specific coat protein

Pristine multiwalled CNT (length 15μm and diameter 20-60nm) were purchased from Carbon Nanotechnologies Incorporation (CNI). All chemicals were of analytical grade and used as received. The surface modification of carbon nanotubes was performed using the following procedure [219]. First, 10mg of multi walled carbon nanotube (MWNTs) powder was treated with 10 ml of concentrated sulfuric acid/nitric acid mixture (3/1 in v/v) under strong sonication for 10 hr. After this treatment, the oxidized MWNTs were obtained after filtration and were then thoroughly rinsed. Subsequently, the pH was adjusted to 7 in order to achieve net negatively charged carboxylate groups. For typical functionalization with PEI, oxidized MWNTs (0.5 mg mL^{-1}) were mixed with polycationic polyethylenimine (PEI) (2 mg ml^{-1}) under ultra-sonication for 1hr immediately followed by 30 min of vigorous vortexing. The mixture was centrifuged at 10,000 rpm for 25 min and the pellets were collected and redispersed in 5mL of deionized water. This centrifugation/wash/redispersion cycle was further repeated twice to remove any physically absorbed polymer and free polymer attached to the carbon nanotubes. Finally, the polymer-MWNTs composite was redispersed in water. Later PEI

was used as a linker to adsorb anionic ss-DNA. The ss-DNA (OD 20) was mixed with 5ml of MWNT conjugated PEI and vortexed for 30 min. After vortexing the mixture was treated with a series of centrifugation / wash / dispersion /centrifuge/redispersion cycles, and finally the MWNT@PEI/ssDNA conjugate was obtained. The pVIII (1.03 mg/ml) solution was mixed with 5ml of MWNTs@PEI/ssDNA conjugate dispersion and vortexed for 30min. The resultant pellet was collected after centrifugation and purification. Finally the MWNTs@PEI/ssDNA/pVIII was dissolved in 0.5x PBS.

4.2.5 Conjugation of SKBR-3 specific bacteriophage with photosensitizer, PPa

In this procedure, first 1 mg of PPa was dissolved in 1 mL of DMSO and the carboxyl groups are activated with 0.4 mg EDC. The reaction mixture was incubated at 37^{o}C on a shaker for 1hr and after incubation; the unreacted EDC was quenched by few 2 µl of mercapto ethanol (MeSH). The resultant activated PPa was stored at -80^{o}C for further use. The modification of bacteriophage with PPa was performed by carefully adjusting molar ratio between the two. In order to retain the target specificity of the resulting phage, the phage is partially modified with PPa. Briefly, 22.5µl of activated PPa was added to 2ml of phage solution (6.4x1012 virons/ml). The mixture is incubated for 1h at 37^{o}C under constant shaking. The free dye is removed using extensive dialysis against distilled water. The solutions are stored at -20^{0}C for further use.

4.2.6 Assembly of cationic liposomes on glutamic acid displayed bacteriophage :

Lipid 1,2-dioleoyl-3- trimethylammonium propane chloride (DOTAP) and 1,2-dioleoyl-sn-glycerophosphocholine (DOPC) were obtained as chloroform solutions from Avanthi lipids. Later the cationic liposomes were prepared from 1,2-dioleoyl-3-trimethylammonium propane chloride (DOTAP) and 1,2-dioleoyl-sn-glycerophosphocholine (DOPC) in a mass ratio of 30:70 in the presence of CTAB as a surfactant by using the detergent depletion method [220]. A stock solution of ZnPc was dissolved in N-methyl-2-pyrrolidinone at 50^0C and added to the chloroform mixture of DOTAP/DOPC such that the ratio of ZnPc/lipid was kept constant at 1:100. The ZnPc/ lipid solution was dried with a stream of nitrogen gas and a transparent film was deposited in the bottom of a glass vessel. A highly concentrated solution of CTAB (3:1 detergent/lipid molar ratio), prepared with a phosphate buffer (10mM NaH2PO4, pH 7.0; 100mM NaCl), was added to the dried film. Samples were then sonicated until clear to form mixed micelles, and extensive dialysis was performed with a dialysis bag (molecular weight cutoff 6–8000) with three changes of phosphate buffer solution. After dialysis, residual CTAB was removed from the liposome mixture by eluting the suspension through a Sephadex G-50 column with the same solvent. The resultant liposome solution was filtered by extrusion through a polycarbonate membrane with 200-nm pores (Avestin, Ottawa, Canada) to remove ZnPc that was not incorporated in the lipid bilayer of the liposomes. The assembly of liposomes on the phage to form phage–

liposome complexes was initiated by adding an aliquot of phage to a solution of the liposome.

4.2.7 Transmission electron microscopic studies

The surface morphology of carbon nanotubes after polymer coating and protein coating was verified using TEM. The morphological differences between the SKBR-3 specific phage before and after modification with PPa was examined using high resolution TEM. Also, the assembly of liposomes on glutamic acid residues displayed phage is verified using TEM. The various functionalized carbon nanotubes samples are dropped on a copper grid and viewed under TEM. In case of porphyrin modified phage, solution was dropped on a Tedpella carbon coated silver grids and stained with uranium acetate for 10 sec. All TEM images were recorded at the same magnification to understand the morphological changes using JEOL 2000 FX. In case of phage-liposome complex, the phage was stained with 1.5% uranyl acetate (pH 3.5), and the phage–liposome complex was stained with a neutral solution containing 2.5% phosphotungstic acid and 1.5% trehalose and viewed under Zeiss 10 TEM.

4.2.8 Singlet oxygen measurements using steady state method

In order to demonstrate the ability of phage-PPa complex to produce singlet oxygen necessary for PDT experiments, we performed steady state method to confirm the generation of singlet oxygen. Here we used 1,3-diphenylisobenzofuran (DPBF), as a

standard singlet oxygen $^1O_2$ trap [221] in dimethyl sulphoxide (DMSO) and excited with 658±10 nm of continuous wave laser. In these steady state experiments, the absorption of PPa and p-PPPa at 658nm was fixed to 0.1. All the experiments were carried out in an air saturated DMSO solution using picomolar concentrations of DPBF at ambient temperatures of 20-22^{o}C in completely dark conditions. Samples were photolyzed in a 1 cm quartz cell with a 658 nm diode laser (using continuous laser) at 50 mW of power. The disappearance of DPBF was monitored at: 0, 15, 45, 75, 105, 135, and 165 seconds by its change in absorbance at 410 nm.

4.2.9 Cell culture, functionalized nanotubes incubation and fluorescence microscopy

The target SKBR-3 breast cancer cells and the control MCF-7 cells were cultured in Mc. Coy's and DMEM medium supplemented with penicillin (100 μg /mL), streptomycin (100 μg/mL), and 10% heat-inactivated FBS. Both the target and control cells were incubated with MWNT@PEI and MWNT@PEI/ssDNA/pVIII (the DNA here is fluorescently labeled with fluorescein isothiocyanate (FITC)) conjugates at a concentration of 10μg/mL and allowed to interact for 1hr. After incubation, the medium was removed and the cells were washed thoroughly three times to remove non-specific interactions between the carbon nanotubes and cells. All the target and control cells were examined under a Zeiss Universal epiflourescence microscope equipped with Olympus oil immersion DApo UV objectives. Digital images of the cells were collected using the Olympus DP-70 camera and software.

4.2.10 *In Vitro* Photo dynamic therapy (PDT) studies

The target SKBR-3 cells and control MCF-7 cells were cultured in a six well plate till they reached 90% confluence as described above. Then a 10 μM concentration of porphyrin and phage coated porphyrin were prepared in suitable medium and incubated with target and control cells for 1 h at 37^{o}C. After 1h of incubation, the unbound conjugates are removed by through washings with PBS and the finally replaced with fresh medium. For PDT experiments, 7.5 J/cm^2 of illumination was delivered using a visible green laser light. The light spot covered four wells, which were considered as one experimental group illuminated at the same time. Control groups involved cells without conjugates, treated with laser light alone, treated with bacteriophage without prophyrin complex and with porphyrin alone (absorption at 685 nm is 0.1). For time course incubation studies the phage coated porphyrin were incubated with SKBR-3 cells and MCF-7 cells for various times (1h, 15h and 24h) and subsequently PDT with 7.5 J/cm^2 of 658 nm light was delivered at dose of 50 mW/cm^2. Following PDT treatment the cells were returned to the incubator for few hours and a live/dead cell viability kit is used to evaluate the cell death. All the fluorescence images were captured using Nikon Eclipse Ti system.

4.3 Results

4.3.1 Self assembly of coat proteins on functionalized carbon nanotubes

In our biomimetic protein self assembly procedure (as shown in Figure 4-1), the MWNTs were first oxidized with a sulphuric acid mixture and modified with polycationic PEI polymer. The functionalized nanotubes were further wrapped with negatively charged ssDNA and then coated with pVIII specific to SKBR-3 cells by mimicking the phage assembly process where several thousand copies of pVIII are assembled along ssDNA to form a mature phage particle (as shown in Figure 1-3). The initial surface modifications were characterized by FT-IR as shown in Figure 4-2. A broad band is found at 3420 cm^{-1} for the oxidized MWNT which is attributed to the presence of –OH groups. The peaks at 1712 and 1624 cm^{-1} correspond to carboxylic groups and carbonyl groups, respectively. The coating of PEI on MWNTs was also characterized by FT-IR spectra, which show double peaks within 2800-2900 cm^{-1} assignable to the $–CH_2-$ group (Figure 4-2). Later ssDNA was added to the MWNT@PEI composite, resulting in a MWNT@PEI/ssDNA conjugate. Figure 4-3 shows the UV-visible spectra of the MWNTs, MWNT@PEI and MWNT@PEI/ssDNA suspension. The MWNT@PEI composite exhibited the same characteristic peak found for PEI, suggesting that PEI is attached to the MWNT surface. On the other hand, the purified MWNT@PEI/ssDNA composite showed small peaks at 260 nm, which was also found to be the characteristic peak from ssDNA, suggesting that ssDNA is attached to the surface. We further performed zeta potential measurements to determine the surface charge of functionalized nanotubes as shown in Figure 4-4. MWNTs are negatively charged at pH 7 which is consistent with the Zeta potential value of -23.84 mV. This suggests a

deprotonation of the functional carboxylic groups on the MWNTs surface after modification with the sulfuric acid/nitric acid mixture. After functionalization with the polycationic PEI coating, the surface charge turned positive, suggesting that the outermost layer is a polycation. This implies a successful coating of the polymer on the MWNTs. The oligonucleotide coating on the MWNTs surfaces was expected to have a change in polarity and zeta potential values. As expected, the zeta potential of the resultant dispersion is negative, indicating that the ssDNA was successfully coated onto the surface. Further, when the pVIII solution was added to the MWNTs@PEI/ssDNA conjugate dispersion and vortexed for 30min, the zeta potential of the suspension is changed but still negative upon the assembly of pVIII onto the MWNTs@PEI/ssDNA conjugate. The pVIII-terminated surface showed a negative surface charge, indicating that the positively charged C-terminal domain of pVIII was in contact with the negatively-charged ssDNA surface via electrostatic interactions, as in the case of phage assembly [218]. As a result, the slightly negative N-terminal domain of the same pVIII, to which cell-targeting peptides are fused, is extended outside, enabling the targeting of the nanotubes to cancer cells. The successful functionalization of MWNTs resulted in remarkably increased water solubility, providing stability for longer times in aqueous solutions (Figure 4-5).

The increase in thickness of polymer and protein on carbon nanotubes surface were further evaluated using TEM (as shown in Figure 4-6 & 4-7). Figure 4-6 shows a typical lattice structure of unmodified MWNTs. Upon coating with PEI, the MWNTs

resulted in the appearance of an amorphous layer having a thickness of approximately 2 nm covered on the MWNT surface (Figure 4-7 B). When a solution of MWNTs@PEI in aqueous suspension was mixed with ssDNA, a further increase in the thickness of the amorphous coat was observed as shown in Figure 4-7 C, this could be resulting from the interactions of ssDNA and positively charged groups on the nanotubes. The degree of condensation of ssDNA on nanotubes depended mainly on the charge density and number of ssDNA molecules. [222] Finally, the SKBR-3 cell-specific pVIII, which bears positively charged amino acids on the C-terminus, was electrostatically interacted with ssDNA functionalized MWNTs. This resulted in an increase in the average surface thickness by approximately 1 nm (Figure 4-7 D), which is in agreement with the length of pVIII proteins (the major coat protein is composed of 50 amino acids), [223] suggesting the formation of a monolayer of pVIII on functionalized MWNTs/ssDNA.

In order to demonstrate the *in vitro* applications of carbon nanotubes coated with cell-targeting phage-derived coat proteins for targeted delivery applications, we studied their interactions with target breast cancer cells (SKBR-3) cells and control cells (MCF-7 cells). For this application purpose the nanotubes were functionalized with fluorescent DNA. Therefore, the functionalized carbon nanotubes were first wrapped with fluorescein conjugated DNA and then conjugated with SKBR-3 specific pVIII. As expected, no fluorescence was observed in the SKBR-3 cells treated with MWNT@PEI due to a lack of chromophore on the polymer. However, the SKBR-3 cells treated with MWNT@PEI/ss-DNA/pVIII showed obvious green fluorescence from the DNA (Figure

4-8B) but no characteristic fluorescence is observed in control cells (as shown in Figure 4-8D, indicating that these MWNTs nanocomposites could be used for target specific delivery purposes. The dark circular regions, being the cell nuclei, appear free of fluorescence, and the complex of MWNT@PEI/ssDNA/pVIII seems to be accumulated within the cytoplasm.

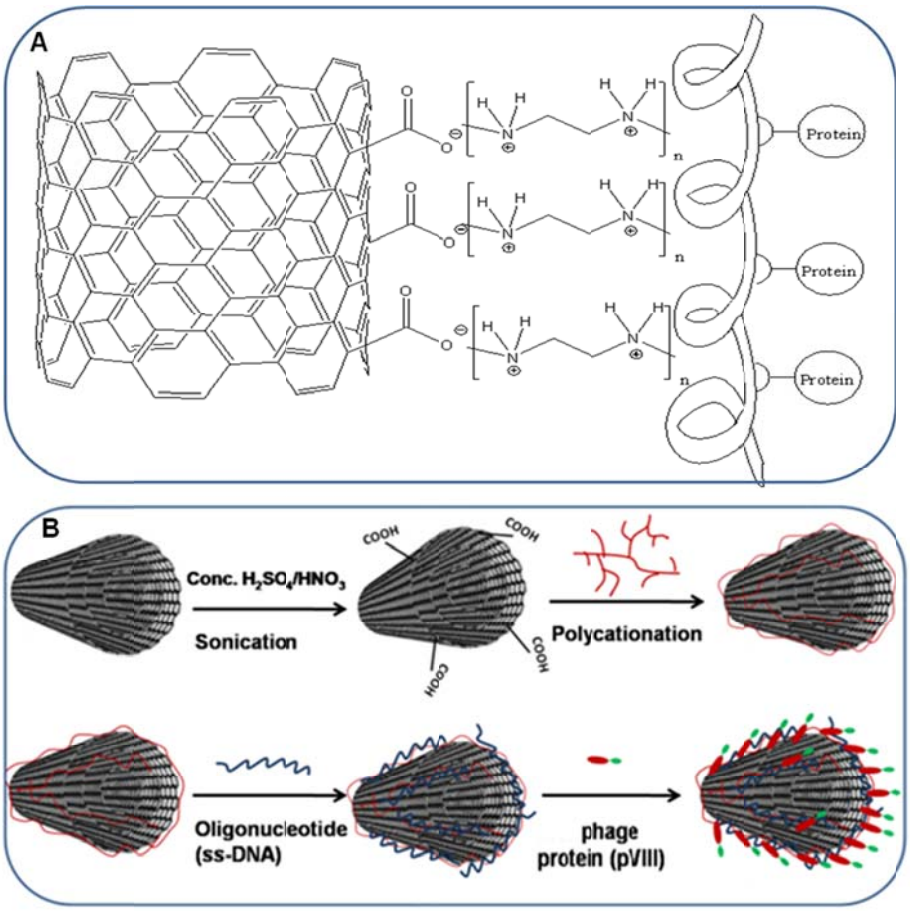

Figure 4-1: Structure (A) and the Design (B) of protein coated multiwall carbon nanotubes (MWNTs).

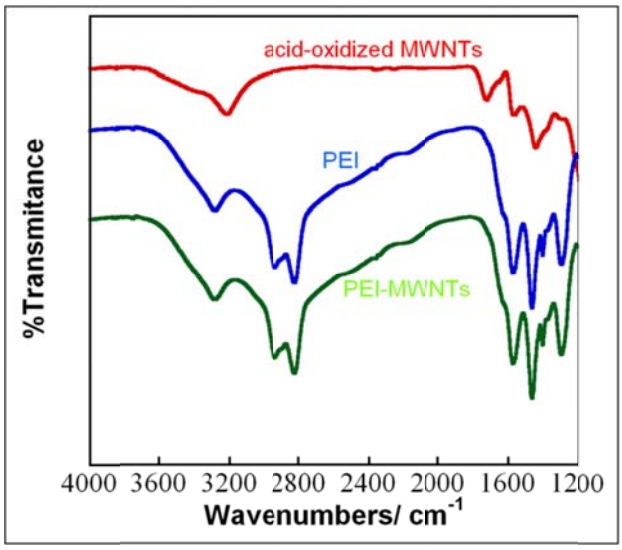

Figure 4-2: FTIR spectra of acid oxidized MWNTs and MWNT@PEI.

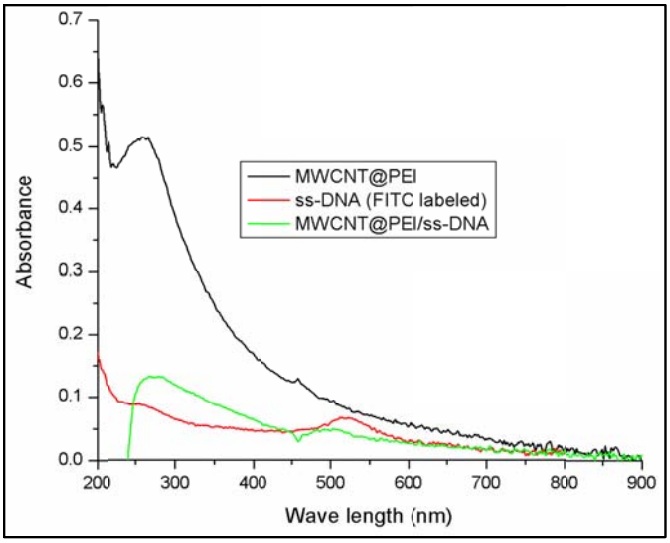

Figure 4-3: UV-visible spectra of DNA and PEI functionalized MWNTs.

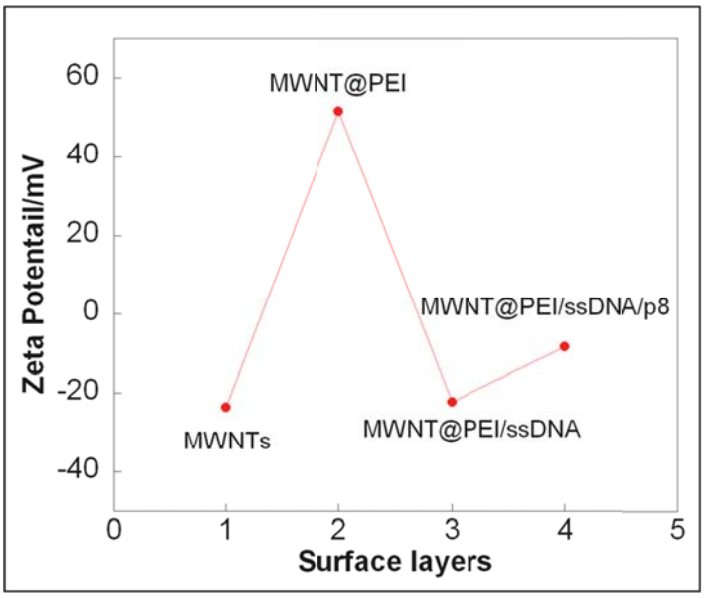

Figure 4-4: Zeta potential measurements of functionalized MWNTs.

Figure 4-5: Stability of MWNT before and after surface modification (A. MWNTs; B. MWNT@PEI; C. MWNT@PEI/ssDNA; D. MWNTs@PEI/ssDNA/PVIII).

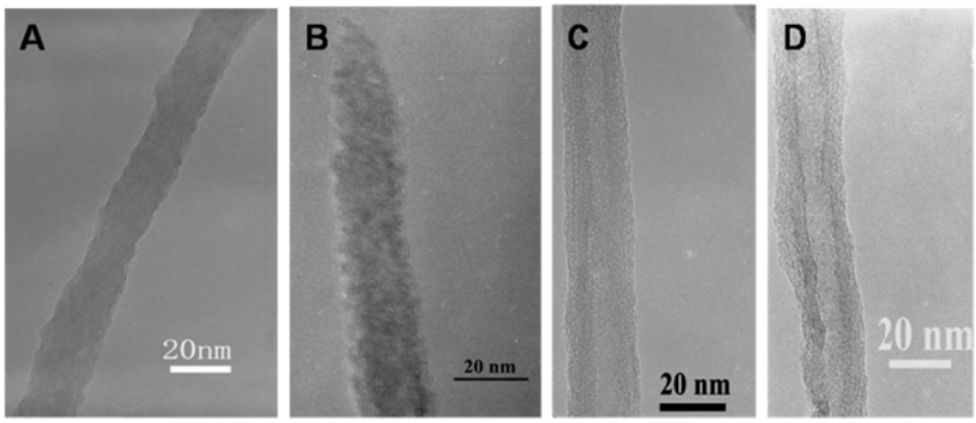

Figure 4-6. Low magnification TEM images of functionalized carbon nanotubes MWNT (A), MWNT@PEI (B), MWNT@PEI/ssDNA(C), and MWNT@PEI/ssDNA/pVIII (D).

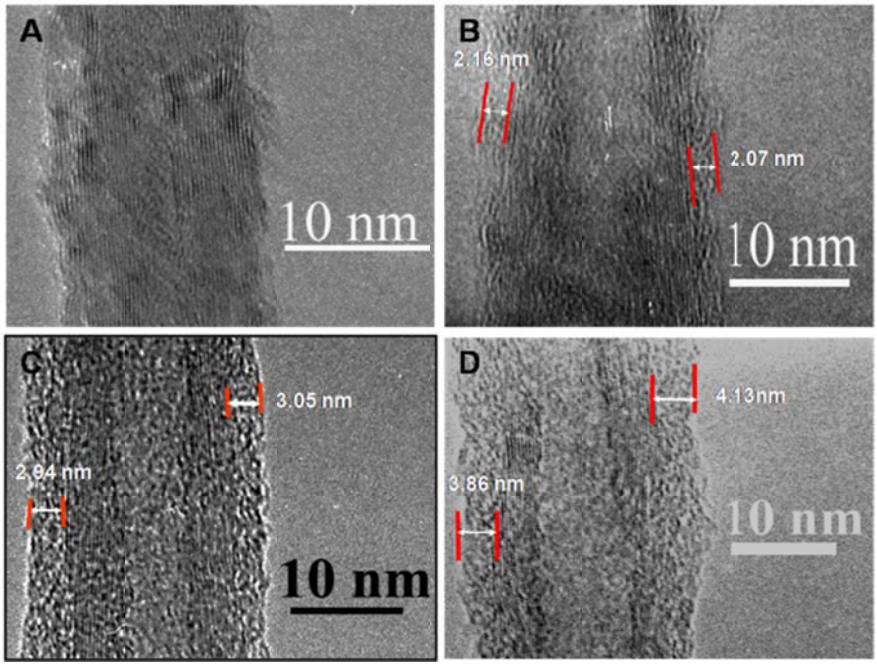

Figure 4-7: High magnification TEM images of functionalized carbon nanotubes MWNT (A), MWNT@PEI (B), MWNT@PEI/ssDNA (C), and MWNT@PEI/ssDNA/pVIII (D).

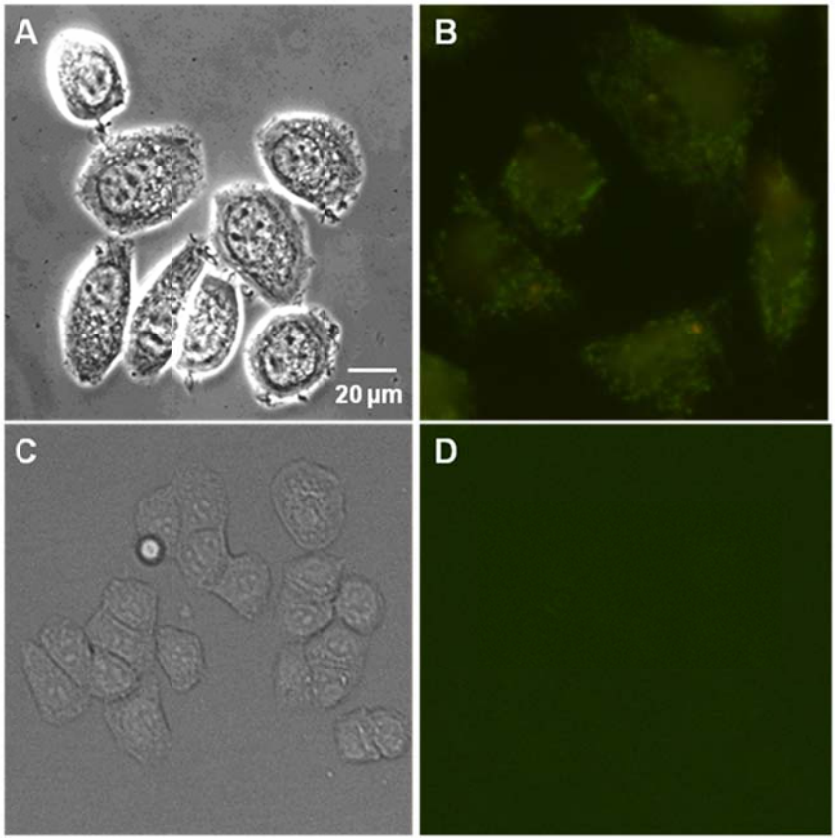

Figure 4-8. Uptake of carboxylated MWNT@PEI/ssDNA/pVIII by SKBR-3 cells and MCF-7 cells (A), Phase contrast image of SKBR-3 cells (B), and fluorescence image upon nanotube conjugates incubation in target SKBR-3 cells. (C) Phase contrast image of MCF-7 cells and (D) fluorescence image upon nanotube conjugates incubation in control cells.

4.3.2 Modification of SKBR-3 specific phage with photosensitizer, PPa

In order to understand the morphological changes of phage and phage modified with porphyrin (PPa), we used electron microscopy. As shown in Figure 4-9 we can

clearly observe a change in the morphology of filamentous bacteriophage before and after photo sensitizer modification. From the TEM images the structure of unmodified bacteriophage seems to be flexible (as shown in Figure 4-9A) in structure and upon completely coating with PPa, the phage is straightened and rigid (as shown in Figure 4-9B). Production of singlet oxygen is the most important aspect of PDT experiments. Hence, we used steady state method to understand the photo physical properties of phage coated porphyrin complex. A decrease in DPBF absorption at 410 nm confirmed the formation of $DPBFO_2$ by its reaction with $^1O_2$ produced from photolysis (Figure 4-10). We estimated the amount of $^1O_2$ molecules produced in both PPa and p-PPPa by calculating the concentration of $DPBFO_2$ formed (Figure 4-11). Kinetic calculation confirmed that the concentration of DPBF was sufficient to intercept more than 95% of the $^1O_2$ produced in the solution.

In order to understand the photodynamic therapy efficiency of phage-porphyrin complex we performed in vitro evaluation on target and control cells. As shown in Figure 4-12, target SKBR-3 cells treated with phage-PPa complex were found to be dead (stained by ethidium bromide in red) upon laser irradiation and control MCF-7 cells were not dead (stained by calsein AM in green) by phage-PPa complex. This confirms the specificity of our phage towards the target cells. However, in presence of porphyrin alone both the target and control cells were found dead. These results clearly demonstrate that our novel p-PPPa sensitizer with inherent target specific phage selectively kills SKBR3 cells upon irradiation with 658 nm laser light.

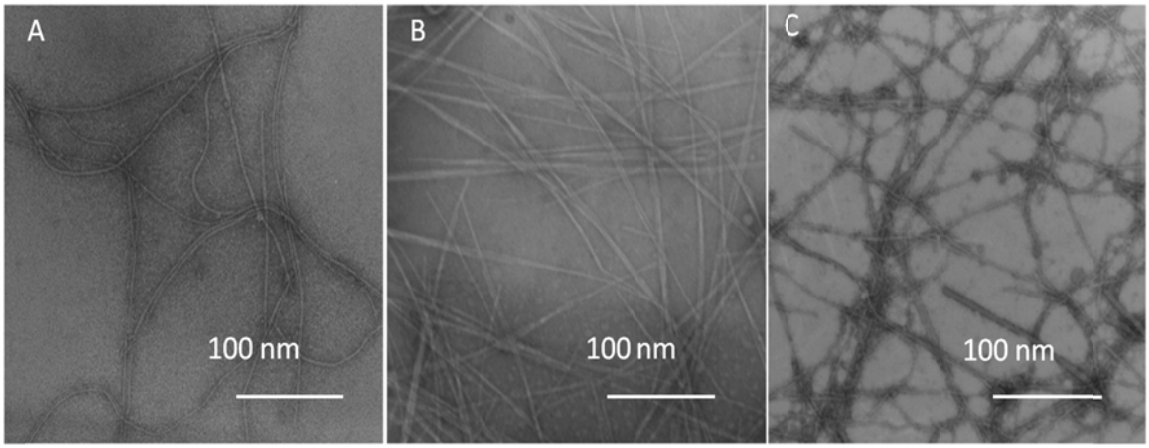

Figure 4-9: Morphology of SKBR-3 selected phage before and after modification with photosensitizer under TEM A. Unmodified filamentous bacteriophage. B. Bacteriophage completely modified with photosensitizer. C. Bacteriophage partially modified with photosensitizer.

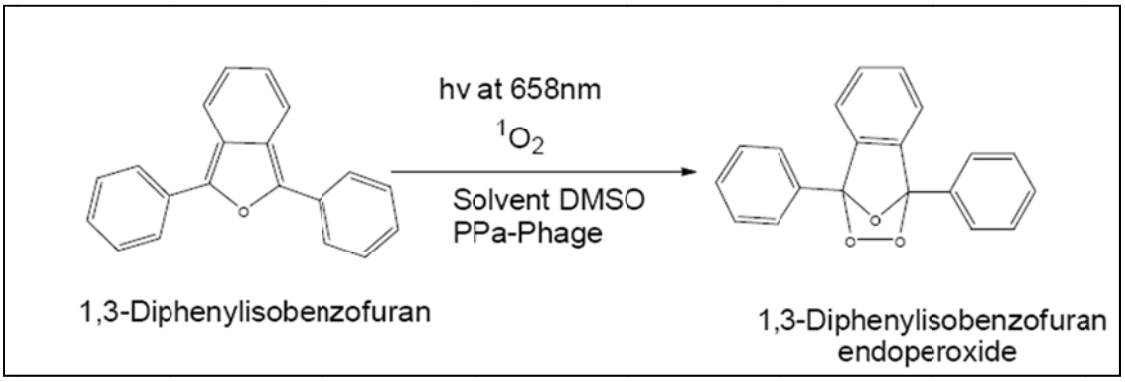

Figure 4-10: Steady State Singlet oxygen trap with 1,3-Diphenylisobenzofuran.

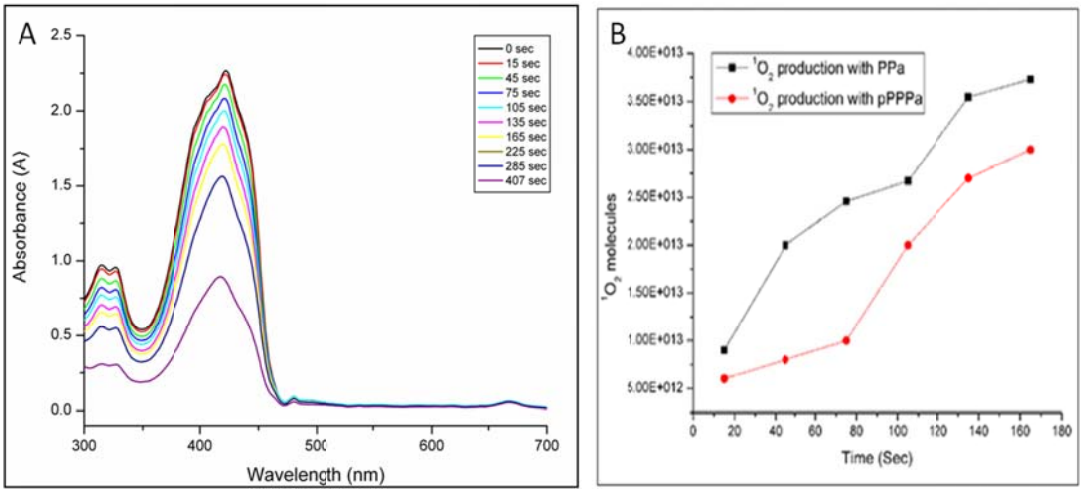

Figure 4-11: Steady State Singlet oxygen measurements of phage-PPa (Phage-pyropheophorbid-a) complex. A. The absorption maximum of DPBF at 410 nm was decreased with increase in irradiation time due to the formation of $DPBFO_2$. B. Only porphyrin is is shown (in black) and Porphyrin-phage complex is shown (in red).

4.3.3 Self assembly of liposome on genetically modified bacteriophage

In order to demonstrate the self assembly of liposomes on the filamentous phage structure, we used electron microscopy. As shown in Figure 4-13 B the liposomes are assembled uniformly with equal spaced to form bead on a rod structure. One probable reason for the assembly could be the electrostatic interaction between the neighboring vesicles. Figure 4-13A shows the electron microscope image of the bacteriophage before

assembled with bacteriophage. This study demonstrates bacteriophage can be used as a template to control the aggregation of liposomes.

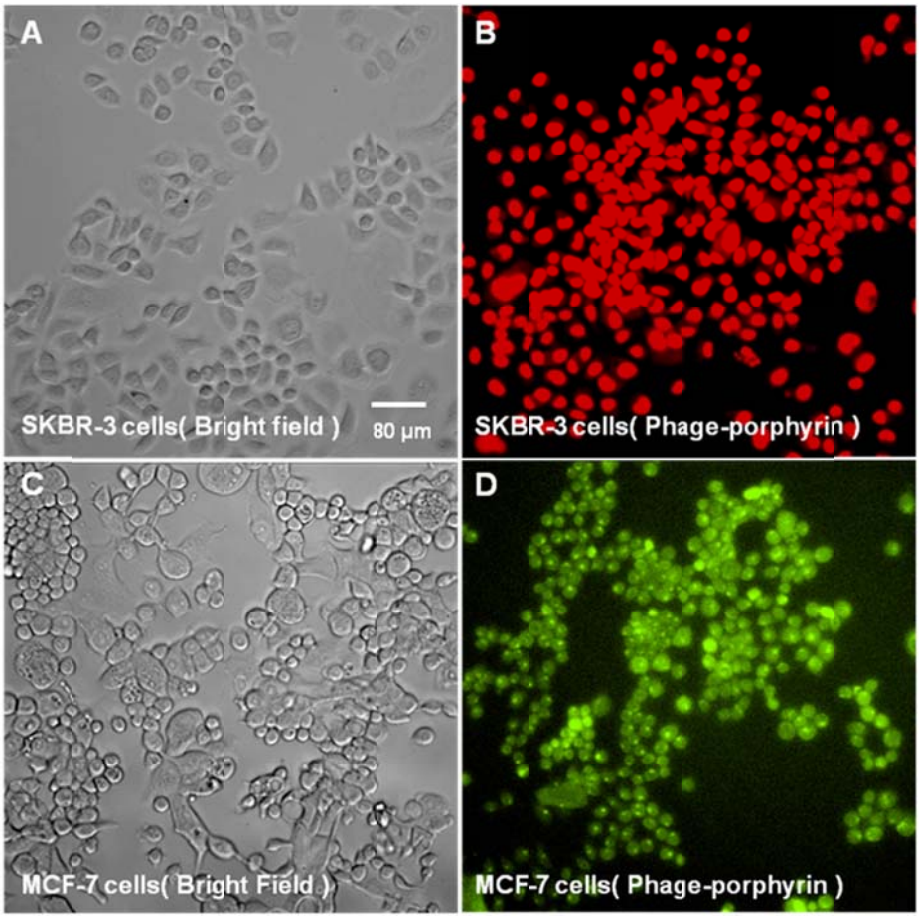

Figure 4-12: *In vitro* PDT evaluation on target and control mammalian cells. (SKBR-3 cells are used as target and MCF-7 cells are used as control. Live/dead cell viability kit is used to determine the cell death; Magnification 10x from the objectives).

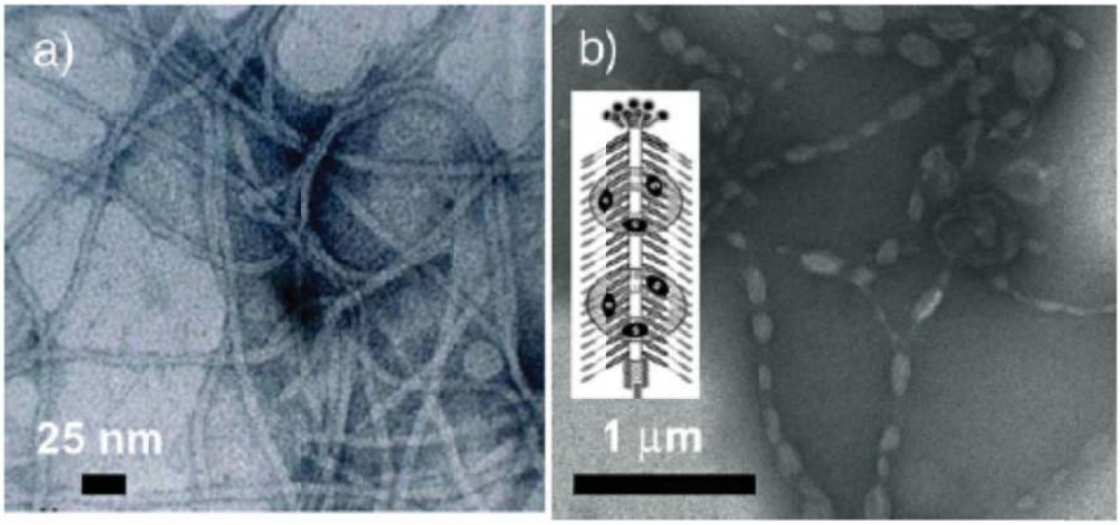

Figure 4-13: TEM images of stained engineered phages a) before and b) after complexation with ZnPc-loaded liposomes. The inset in (b) is a cartoon (not to scale) showing the assembly of liposomes on the phage (the size of the liposome is actually much larger than the width of the phage but smaller than the length of the phage) figure adapted from [215].

4.4 Discussion

The results presented here show the use of bacteriophage as a template for synthesizing novel photosensitizing agent for PDT and assembly of liposomes. We are also the first to assembled phage protein on functionalized carbon nanotubes. The delivery and PDT effects of bacteriophage were confirmed on target SKBR-3 cells and control MCF-7 cells. The driving force for the assembly of protein on the nanotube

surface is electrostatic interactions. Because, the phage protein present on the nanotube surface show specificity to target SKBR-3 breast cancer cells, we expected the fluorescently labeled DNA present on the nanotubes binds to the desired cells. As expected no significant binding is noticed in the control MCF-7 cells. In principle, we believe the structure of protein-nanotubes formed here can be regulated by modifying the different bases in the oligonucleotide sequence or by the number of oligonucleotide chains grafted onto the nanotube surface. Thus, the results presented here show the synthesis of multicomponent assemblies resulting from oligonucleotide and protein conjugation for biomedical applications.

The bacteriophage morphology is an important aspect for retaining the binding properties with targeted cells. When the bacteriophage surface is partially modified with photosensitizer, no significant morphological changes are observed but when the phage is completely modified with porphyrin, they became straightened and rigid. This major morphological change could be due to the strong hydrophobic interactions between the phage major coat proteins and the PPa macrocycle.

In cancer PDT, upon irradiation with light, excited singlet oxygen ($^1O_2$) is generated to induce the killing of cancer cells.[32] Thus, we investigated the efficiency of using phage–porphyrin complexes for cancer PDT by measuring the production of excited singlet oxygen ($^1O_2$) and also by imaging breast cancer cells after their interaction with the phage-PPA complexes for 1 h. The activity of Phage-PPa for the production of $^1O_2$ was studied by following time resolved experiments as discussed earlier. Target and

control cells were treated with porphyrin and phage-porphyrin complex separately and irradiated with a laser power density of 50 mW/cm^2 for a period of 4 minutes. The laser power used in our study is much lower than the power generally used in PDT experiments (200mW/cm^2). This study highlights the new class of virus enabled PDT photosensitizers for targeted cancer treatment. Further evidence showing the mechanism of cell death is under current investigation.

The electrostatic interaction between the anionic phage and cationic liposomes resulted in the self-assembly and immobilization of liposomes on the phage to form a phage–liposome complex. The self-assembled phage–liposome complex can not only stabilize the liposomes against flocculation and but also help in the delivery of drug-loaded liposomes to specific targets (Example: cancer cells). Also, when a cationic electron acceptor such as methyl viologen ions are electrostatically immobilized on the sidewall, it results in desired charge separation in electron-transfer reactions between the dye in the liposomes and the immobilized electron acceptor on the phage.

In summary, we have studied the morphological control of nanomaterial assembly on filamentous bacteriophage and evaluated their chemical and biological properties for possible applications in imaging, PDT and drug delivery. Thus by exploiting the multivalent nature of the phage and its rigidity, we can assemble novel virus-based nanostructures that can be used to various biomedical applications.

Chapter 5

5.1 Summary of this dissertation

Cancer continues to be the leading disease causing killer in the United States. Development of more efficient methods for the simultaneous imaging and selective destruction of cancer is currently an active field of research. The well defined geometries, surface functionalities and monodisperse nature of viruses make them an ideal candidate for phage display technology and nanofabrication. With the recent advancement in nanotechnology and the applications of phage display technology, it is now possible to combine both on a single platform for potential biomedical applications. This new approach of cancer treatment integrates the target specific binding and circulatory behavior of viruses and nanosize architecture with unique optical properties for effective molecular interactions and novel practical applications.

The first part of this dissertation is aimed at exploring unique protein-protein interactions between the target SKBR-3 breast cancer cells and landscape phage libraries. Here we identified new cell targeting/internalizing peptides (and the phages with such peptides fused to each of ~3900 copies of their major coat protein) using landscape phage libraries and for the first time investigated the actin dynamics when selected phages are internalized into the SKBR-3 breast cancer cells. Our results show that phages harboring VSSTQDFP and DGSIPWST peptides could selectively internalize into the SKBR-3 breast cancer cells with high affinity, and specificity. The actin dynamics was studied by

using live cell and fluorescence imaging. The cell-internalizing phages were found to enter breast cancer cells through energy dependent mechanism; and phage entry interferes with actin dynamics, resulting in reorganization of actin filaments and increased membrane rufflings in SKBR-3 cells. These results suggest that, when phage enters epithelial cells, it triggers transient changes in the host cell actin cytoskeleton. This study also shows that using multivalent phage libraries considerably increases the repertoire of available cell-internalizing ligands with potential applications in targeted drug delivery, imaging, molecular monitoring and profiling of breast cancer cells.

With the recent progress in nanotechnology it is now possible to custom synthesize a variety of nanomaterials for biological applications. In particular gold nanorods has been of great interest to researchers in cancer because of their easy preparation, ability for bioconjugation, excellent biocompatibility, tunable and enhanced scattering and absorption properties. The strong scattering and absorption from gold nanorods provides an opportunity for their use in cancer cell imaging and photo thermal therapy applications.

The second part of this dissertation is aimed at the synthesis, multipurpose applications, and molecular level interactions of novel nanoprobes. Here, we demonstrate the first example of the self-assembly of coat protein pVIII derived from filamentous phage onto gold nanorods to form GNR-pVIII complex (nanoprobe). The biocompatibility, specificity, imaging and photo thermal abilities of GNR-pVIII were demonstrated using various spectroscopic and microscopic techniques. Our results show

that phage coat proteins enable the tumor-specific targeting and internalization of nanoparticles to target cells. Further, gene expression profiling using microarrays identified the novel mechanism of the interaction between GNR-pVIII and target breast cancer cells. We hypothesize GNR-pVIII were first bound to heparin on the cell surface and then internalized by lysosomes. Due to the structural similarity of GNR-pVIII with phage, the coat proteins on the GNRs might be interacted with the Major Histocompatibility Complex I (MHC class I), and transported to immune system for destruction, leaving gold nanorods inside the cells. Furthermore, seven members of the poorly annotated G antigen family (GAGE) genes were activated by GNR-pVIII complex, possibly representing novel mechanisms of GNR-pVIII processing by immune system. Thus mimicking phage structure to develop novel nanoprobes opens up a new way to develop targeted therapeutics. In conclusion, GNR-pVIII exhibited excellent multi-functional properties including target specificity, non-cytotoxicity, as well as imaging and photo thermal destruction capability in our model SKBR-3 breast cancer cells.

The third part of this dissertation is aimed at exploring the filamentous structure and proteins components of bacteriophage for novel biomedical applications. Here, three different examples are used to prove the biomedical applications of bacteriophage. In the first example, we demonstrate the conjugation of coat proteins on functionalized multi walled nanotubes for targeted delivery. Here, we report a simple layer-by layer self assembly technique for the assembly of an oligonucleotide (ss-DNA) and fd

bacteriophage major coat proteins onto polycationic polyethylenimine (PEI) functionalized multi-walled carbon nanotubes using non-covalent interactions. The use of various spectroscopic and microscopic techniques confirmed the assembly of coat proteins on functionalized nanotubes. The resulting nanocomposites may find potential applications in drug/gene delivery, medical therapy, and bioanalytical sensing.

In the second example we report the first conjugation of porphyrin, pyropheophorbid-a (PPa), to SKBR-3 specific bacteriophage (L1 phage), to form a novel phage-PPa complex and its successful in vitro PDT application in targeting SKBR-3 breast cancer cells. The resulting complexes were characterized by various spectroscopic and microscopic techniques. The incubation of phage-PPa complex with target SKBR-3 cells for 1h and irradiation with 7.5 J/cm^2 red laser at 658nm resulted in the death of target cancer cells leaving the control cells unharmed. Thus, the reported virus enabled photosensitizers open new avenues for novel photosensitizers for clinical applications.

In the third example, a biomimetic approach is used to stabilize the drug loaded liposomes via the self-assembly of ZnPc-loaded liposomes on the glutamic acid engineered bacteriophage. The resultant composites can be used for PDT (if the liposomes are entrapped with a photosensitizer) and drug-delivery applications (if the liposomes are entrapped with a chemotherapeutic agent). Here, M13 phage was genetically modified to display a negatively charged peptide (eight glutamic acid residues) on the sidewall of 2700 copies of ordered major coat protein pVIII which allowed strong multivalent electrostatic interactions with the cationic liposomes. The

electrostatic interaction between the anionic phage and cationic liposomes resulted in the self-assembly and immobilization of liposomes on the phage to form a phage–liposome complex and characterized by using electron microscopic imaging. The resulting self-assembled phage–liposome complex can not only stabilize the liposomes against flocculation but might also help in the delivery of drug-loaded liposomes to specific targets.

In conclusion, genetically engineered nanoconstructs derived from phage components and nanomaterials can be envisioned as novel probes for biomedical applications. A variety of novel nanoassembled structures are currently under investigation in which bacteriophage is being an active ingredient because of their interesting characteristics features such as monodispersity, characteristic surface properties, and error free production. Despite extensive research in utilizing genetically engineered nanoconstructs for medical applications, there is still concern regarding their toxicity. At present the great challenges in front of researcher are to successfully overcome the toxicity, immunogenicity of the hybrid system and to increase the therapeutic efficiency at the target site. Overall, genetically engineered nanoconstructs are showing tremendous advancement in many fields of research indicating great potential for applications in the future.

References

1. Rodi, D.J.; Mandava, S.; Makowski, L., Filamentous bacteriophage structure and biology. In *Phage display in biotechnology and drug discovery*, Carmen, A., Ed. Taylor & Francis group, LLC: San Diego, 2005.

2. Marvin, D.A. Model-building studies of Inovirus: genetic variations on a geometric theme. *Int. J. Biol. Macromol.* **1990**, *12*, 125-138.

3. Stengele, I.; Bross, P.; Garces, X.; Giray, J.; Rasched, I. Dissection of functional domains in phage fd adsorption protein : Discrimination between attachment and penetration sites. *J. Mol. Biol.* **1990**, *212*, 143-149.

4. Beck, E.; Zink, B. Nucleotide sequence and genome organisation of filamentous bacteriophages f1 and fd. *Gene* **1981**, *16*, 35-58.

5. Kehoe, J.; Kay, B. Filamentous phage display in the new millennium. *Chem Rev.* **2005**, *105*, 4056-4072.

6. Petrenko, V.A. Landscape phage as a molecular recognition interface for detection devices. *Microelectronics J.* **2008**, *39*, 202–207.

7. Spruijt, R.B.; Wolfs, C.J.A.M.; Hemminga, M.A. Aggregation-related conformational change of the membrane-associated coat protein of bacteriophage M13. *Biochemistry* **1989**, *28*, 9158-9165.

8. Russel, M.; Model, P. Genetic analysis of the filamentous bacteriophage packaging signal and of the proteins that interact with it. *J. Virol.* **1989**, *63*, 3284–3295.

9. Petrenko, V.A.; Smith, G.P., Vectors and Modes of Display. In *Phage display in biotechnology and drug discovery*, Sidhu, S. S., Ed. Taylor & Francis group, LLC: San Diego, 2005.

10. Marvin, D. Filamentous phage structure, infection and assembly. *Curr. Opin. Struct. Biol.* **1998**, *8*, 150-158.

11. Smith, G., Filamentous phage as cloning vectors. In *Vectors: A survey of molecular cloning vectors and their uses.*, Rodriquez RL, ed ed.; Boston, 1987; pp 61–83.

12. Abbineni, G.; Mao, C.B., Design and Applications of Genetically Engineered Nanocomposites. In *Nanomaterials for Life Sciences: Nanocomposites*, Kumar, C., Ed. Wiley-VCH: 2010.

13. Maniatis, T.; Hardison, R.; Lacy, E.; Lauer, J.; O'Connell, C.; Quon, D.; Sim, G.; Efstratiadis, A. The isolation of structural genes from libraries of eucaryotic DNA. *Cell* **1978**, *15*, 687–701.

14. Bratkovic, T. Progress in phage display: evolution of the technique and its applications. *Cell. Mol. Life Sci.* **2010**, *67*, 749–767.

15. Smith, G. Filamentous fusion phage: novel expression vectors that display cloned antigens on the virion surface. *Science* **1985**, *228*, 1315-1317.

16. Du, C.; Chan, W.C.; McKeithan, T.W.; Nickerson, K.W. Surface Display of Recombinant Proteins on Bacillus thuringiensis Spores. *Appl. Environ. Microbiol.* **2005**, *71*, 3337–3341.

17. Feldhaus, M.J.; Siegel, R.W.; Opresko, L.K.; Coleman, J.R.; Feldhaus, J.M.; Yeung, Y.A.; Cochran, J.R.; Heinzelman, P.; Colby, D.; Swers, J.; Graff, C.; Wiley, H.S.; Wittrup, K.D. Flow-cytometric isolation human antibodies from a nonimmune saccharomyces cerevisiae surface display library. *Nat. Biotechnol.* **2003**, *21*, 163-170.

18. Wang, Y.; Rubtsov, A.; Heiser, R.; White, J.; Crawford, F.; Marrack, P.; Kappler, a.J.W. Using a baculovirus display library to identify MHC class I mimotopes. *Proc. Nat. Acad. Sci. U.S.A.* **2005**, *102*, 2476-2481.

19. Efimov, V.P.; Nepluev, I.V.; Mesyanzhinov, V.V. Evolution of T4-related phages. *Virus Genes* **1995**, *10*, 173-177.

20. Sternberg, N.; Hoess, R.H. Display of peptides and proteins on the surface of bacteriophage lambda. *Proc. Natl. Acad. Sci. USA* **1995**, *92*, 1609-1613.

21. Hoess, R.H. Protein design and phage display. *Chem. Rev.* **2001**, *101*, 3205-3218.

22. Arap, M. Phage display technology - Applications and innovations *Genet. Mol. Biol.* **2005**, *28*, 1-9.

23. Smith, G.P.; Petrenko, V.A. Phage display. *Chem. Rev.* **1997**, *97*, 391-410.

24. Clackson, T.; Lowman, H., *Phage display. A practical approach.*; Oxford University Press: New York, 2004.

25. Sidhu, S., *Phage display in biotechnology and drug discovery.*; CRC Boca Raton, 2005.

26. Parmley, S.; Smith, G. Antibody-selectable filamentous fd phage vectors: affinity purification of target genes. *Gene* **1988**, *73*, 305-318.

27. Cwirla, S.; Peters, E.; Barrett, R.; Dower, W. Peptides on phage: a vast library of peptides for identifying ligands. *Proc Natl Acad Sci U S A.* **1990**, *87*, 6378-6382.

28. Pasqualini, R.; Ruoslahti, E. Organ targeting in vivo using phage display libraries. *Nature* **1996**, *380*, 364-366.

29. Krag, D.; Shukla, G.; Shen, G.; Pero, S.; Ashikaga, T.; Fuller, S.; Weaver, D.; Burdette-Radoux, S.; Thomas, C. Selection of tumor-binding ligands in cancer patients with phage display libraries. *Cancer Res.* **2006**, *66*, 7724-7733.

30. Petrenko, V.A.; Smith, G.P.; Gong, X.; Quinn, T. A library of organic landscapes on filamentous phage. *Protein Eng.* **1996**, *9*, 797-801.

31. Sidhu, S.S.; Fairbrother, W.J.; Deshayes, K. Exploring protein - protein interactions with phage display. *ChemBioChem* **2003**, *4*, 14-25.

32. Woiwode, T.; Haggerty, J.; Katz, R.; Gallop, M.; Barrett, R.; Dower, W.; Cwirla, S. Synthetic compound libraries displayed on the surface of encoded bacteriophage. *Chem Biol.* **2003**, *10*, 847-858.

33. Wagner, S.; Hafner, C.; Allwardt, D.; Jasinska, J.; Ferrone, S.; Zielinski, C.; Scheiner, O.; Wiedermann, U.; Pehamberger, H.; Breiteneder, H. Vaccination with a human high molecular weight melanoma-associated antigen mimotope induces a humoral response inhibiting melanoma cell growth in vitro. *J. Immunol.* **2005**, *174*, 976-982.

34. Larocca, D.; Kassner, P.; Witte, A.; Ladner, R.; Pierce, G.; Baird, A. Gene transfer to mammalian cells using genetically targeted filamentous bacteriophage. *FASEB J.* **1999**, *13*, 727-734.

35. Arap, W.; Haedicke, W.; Bernasconi, M.; Kain, R.; Rajotte, D.; Krajewski, S.; Ellerby, H.; Bredesen, D.; Pasqualini, R.; Ruoslahti, E. Targeting the prostate for destruction through a vascular address. *Proc. Natl. Acad. Sci. U.S.A.* **2002**, *99*, 1527-1531.

36. Fack, F.; Hügle-Dörr, B.; Song, D.; Queitsch, I.; Petersen, G.; Bautz, E. Epitope mapping by phage display: random versus gene-fragment libraries. *J. Immunol. Methods.* **1997**, *206*, 43-52.

37. Scott, J.; Smith, G. Searching for peptide ligands with an epitope library. *Science* **1990**, *249*, 386-390.

38. Doorbar, J.; Winter, G. Isolation of a peptide antagonist to the thrombin receptor using phage display. *J. Mol. Biol.* **1994**, *244*, 361-369.

39. Abbineni, G.; Modali, S.; Safiejko-Mroczka, B.; Petrenko, V.; Mao, C. Evolutionary selection of new breast cancer cell-targeting peptides and phages with the cell-targeting peptides fully displayed on the major coat and their effects on actin dynamics during cell internalization. *Mol Pharm.* **2010**, *7*, 1629–1642.

40. Ruoslahti, E. RGD and other recognition sequences for integrins. *Annu Rev Cell Dev Biol.* **1996**, *12*, 697-715.

41. Dente, L.; Vetriani, C.; Zucconi, A.; Pelicci, G.; Lanfrancone, L.; Pelicci, P.; Cesareni, G. Modified phage peptide libraries as a tool to study specificity of phosphorylation and recognition of tyrosine containing peptides. *J Mol Biol.* **1997**, *269*, 694-703.

42. Cardó-Vila, M.; Arap, W.; Pasqualini, R. Alpha v beta 5 integrin-dependent programmed cell death triggered by a peptide mimic of annexin V. *Mol Cell.* **2003**, *11*, 1151-1162.

43. Goodson, R.; Doyle, M.; Kaufman, S.; Rosenberg, S. High-affinity urokinase receptor antagonists identified with bacteriophage peptide display. *Proc. Natl. Acad. Sci. U.S.A.* **1994** *91*, 7129-7133.

44. Kolonin, M.; Saha, P.; Chan, L.; Pasqualini, R.; Arap, W. Reversal of obesity by targeted ablation of adipose tissue. *Nat Med.* **2004**, *10*, 625-632.

45. Mintz, P.; Kim, J.; Do, K.; Wang, X.; Zinner, R.; Cristofanilli, M.; Arap, M.; Hong, W.; Troncoso, P.; Logothetis, C.; Pasqualini, R.; Arap, W. Fingerprinting the circulating repertoire of antibodies from cancer patients. *Nat Biotechnol.* **2003** *21*, 57-63.

46. American Cancer Society. Cancer Facts & Figures 2010. In American cancer society: Atlanta, 2010.

47. AmericanCancerSociety, Cancer Facts & Figures 2009. In 2009.

48. Yarden, Y.; Sliwkowski, M. Untangling the ErbB signalling network. *Nat Rev Mol Cell Biol.* **2001**, *2*, 127-137.

49. Vargo-Gogola, T.; Rosen, J.M. Modelling breast cancer: one size does not fit all. *Nat Rev Cancer.* **2007**, *7*, 659-672.

50. Schaefer, G.; Akita, R.; Sliwkowski, M. A discrete three-amino acid segment (LVI) at the C-terminal end of kinase-impaired ErbB3 is required for transactivation of ErbB2. *J Biol Chem.* **1999**, *274*, 859-866.

51. Moy, B.; Goss, P. Lapatinib: current status and future directions in breast cancer. *Oncologist.* **2006**, *11*, 1047-1057.

52. Holbro, T.; Civenni, G.; Hynes, N.E. The ErbB receptors and their role in cancer progression. *Experimental Cell Research* **2003**, *284*, 99-110.

53. Wieduwilt, M.J.; Moasser, M.M. The epidermal growth factor receptor family: Biology driving targeted therapeutics. *Cellular and Molecular Life Sciences* **2008**, *65*, 1566 – 1584.

54. Roskoski Jr, R. The ErbB/HER receptor protein-tyrosine kinases and cancer. *Biochemical and Biophysical Research Communications* **2004**, *319*, 1-11.

55. Citri, A.; Yarden, Y. EGF–ERBB signalling: towards the systems level. *Nature Review Molecular Cell Biology* **2006**, *7*, 505-516.

56. Mukai, H. Targeted therapy in breast cancer: current status and future directions. *Jpn J Clin Oncol.* **2010**, *40*, 711-716.

57. Wang, X.; Yang, L.; Chen, Z.G.; Shin, D.M. Application of nanotechnology in cancer therapy and imaging. *CA Cancer J. Clin.* **2008**, *58*, 97-110.

58. Peer, D.; Karp, J.M.; Hong, S.; Farokhzad, O.C.; Margalit, R.; Langer, R. Nanocarriers as an emerging platform for cancer therapy. *Nature Nanotech.* **2007**, *2*, 751-760.

59. Salata, O. Applications of nanoparticles in biology and medicine. *Journal of Nanobiotechnology* **2004**, *2*, 1-6.

60. Ferrari, M. Cancer nanotechnology: opportunities and challenges. *Nat Rev Cancer.* **2005**, *5*, 161-171.

61. Gaspar, R.; Duncan, R. Polymeric carriers: preclinical safety and the regulatory implications for design and development of polymer therapeutics. *Adv. Drug. Deliv. Rev.* **2009**, *61*, 1220-1231.

62. Couvreur, P.; Vauthier, C. Nanotechnology: intelligent design to treat complex disease. *Pharm. Res.* **2006**, *23*, 1417-1450.

63. Moghimi, S. Recent developments in polymeric nanoparticle engineering and their applications in experimental and clinical oncology. *Anticancer Agents Med. Chem.* **2006**, *6*, 553-561.

64. Kim, D.; Kim, S.; Kim, H.; Kim, S.; Shin, S.; Kim, J.; Park, K.; Lee, M.; Heo, D. Multicenter phase II trial of Genexol-PM, a novel Cremophor-free, polymeric micelle formulation of paclitaxel, with cisplatin in patients with advanced non-small-cell lung cancer. *Ann. Oncol.* **2007**, *18*, 2009-2014.

65. Hirsch, L.; Gobin, A.; Lowery, A.; Tam, F.; Drezek, R.; Halas, N.; West, J. Metal nanoshells. *Ann Biomed Eng.* **2006**, *34*, 15-22.

66. Bardhan, R.; Grady, N.; Ali, T.; Halas, N. Metallic Nanoshells with Semiconductor Cores: Optical Characteristics Modified by Core Medium Properties. *ACS Nano* **2010**, *4*, 6169-6179.

67. Bickford, L.R.; Agollah, G.; Drezek, R.; Yu, T.-K. Silica-gold nanoshells as potential intraoperative molecular probes for HER2-overexpression in ex vivo breast tissue using near-infrared reflectance confocal microscopy. *Breast Cancer Res. Treat.* **2010**, *120*, 547-555.

68. Kukowska-Latallo, J.; Candido, K.; Cao, Z.; Nigavekar, S.; Majoros, I.; Thomas, T.; Balogh, L.; Khan, M.; Jr, B.J. Nanoparticle targeting of anticancer drug improves therapeutic response in animal model of human epithelial cancer. *Cancer Res.* **2005**, *65*, 5317-5324.

69. Linuma, H.; Maruyama, K.; Okinaga, K.; Sasaki, K.; Sekine, T.; Ishida, O.; Ogiwara, N.; Johkura, K.; Yonemura, Y. Intracellular targeting therapy of cisplatin-encapsulated transferrin-polyethylene glycol liposome on peritoneal dissemination of gastric cancer. *Int. J. Cancer* **2002**, *99*, 130-137.

70. Allen, T. Ligand-targeted therapeutics in anticancer therapy. *Nat. Rev. Cancer.* **2002**, *10*, 750-763.

71. Sapra, P.; Tyagi, P.; Allen, T. Ligand-targeted liposomes for cancer treatment. *Curr. Drug Deliv.* **2005**, *2*, 369-381.

72. Lila, A.S.A.; Ishida, T.; Kiwada, H. Targeting anticancer drugs to tumor vasculature using cationic liposomes. *Pharm. Res.* **2010**, *27*, 1171-1183.

73. Lopes de Menezes, D.E.; Pilarski, L.M.; Allen, T.M. In vitro and in vivo targeting of immunoliposomal doxorubicin to human B-cell lymphoma. *Cancer Res.* **1998**, *58*, 3320–3330.

74. Torchilin, V.P. Recent advances with liposomes as pharmaceutical carriers. *Nat. Rev. Drug Discov.* **2005**, *4*, 145-160.

75. Kim, D.W.; Kim, S.Y.; Kim, H.K.; Kim, S.W.; Shin, S.W.; Kim, J.S.; Park, K.; Lee, M.Y.; Heo, D.S. Multicenter phase II trial of Genexol-PM, a novel Cremophor-free, polymeric micelle formulation of paclitaxel, with cisplatin in patients with advanced non-small-cell lung cancer. *Annals of Oncology* **2007**, *18*, 2009-2014.

76. Maeda, H.; Fang, J.; Inutsuka, T.; Kitamoto, Y. Vascular permeability enhancement in solid tumor: various factors, mechanisms involved and its implications. *Int. Immunopharmacol.* **2003**, *3*, 319-328.

77. Maeda, H.; Sawa, T.; Konno, T. Mechanism of tumor-targeted delivery of macromolecular drugs, including the EPR effect in solid tumor and clinical overview of the prototype polymeric drug SMANCS. *J. Controlled Release* **2001**, *74*, 47-61.

78. Matsumura, Y.; Maeda, H. A new concept for macromolecular therapeutics in cancer chemotherapy: Mechanism of tumor tropic accumulation of proteins and antitumor agent SMANCS. *Cancer Res.* **1986**, *46*, 6387–6392.

79. Hobbs, S.; Monsky, W.; Yuan, F.; Roberts, W.; Griffith, L.; Torchilin, V.; Jain, R. Regulation of transport pathways in tumor vessels: role of tumor type and microenvironment. *Proc Natl Acad Sci U S A.* **1998**, *95*, 4607-4612.

80. Pastan, I.; Hassan, R.; FitzGerald, D.J.; Kreitman, R.J. Immunotoxin therapy of cancer. *Nat. Rev. Cancer* **2006**, *6*, 559-565.

81. Park, J.; Hong, K.; Kirpotin, D.; Colbern, G.; Shalaby, R.; Baselga, J.; Shao, Y.; Nielsen, U.; Marks, J.; Moore, D.; Papahadjopoulos, D.; Benz, C. Anti-HER2 immunoliposomes: enhanced efficacy attributable to targeted delivery. *Clin. Cancer Res.* **2002**, *8*, 1172-1181.

82. Faraday, M. Experimental relations of gold (and other metals) to light. *Philos. Trans. R. Soc. London* **1857**, *147*, 145-181.

83. Nikoobakht, B.; El-Sayed, M.A. Preparation and growth mechanism of gold nanorods (NRs) using seed-mediated growth method. *Chem. Mater.* **2003**, *15*, 1957-1962.

84. Franklin, K.; Jae Hee, S.; Peidong, Y. Photochemical synthesis of gold nanorods. *J. Am. Chem. Soc.* **2002**, *124*, 14316–14317.

85. Yu, Y.Y.; Ser-Sing, C.; Chien-Liang, L.; C. R. Chris, W. Gold Nanorods: Electrochemical Synthesis and Optical Properties. *J. Phys. Chem. B* **1997**, *101*, 6661-6664.

86. Jana, N.R.; Gearheart, L.; Murphy, C.J. Seed-mediated growth approach for shape- controlled synthesis of spheroidal and rod-like gold nanoparticles using a surfactant template. *Adv. Mater.* **2001**, *13*, 1383-1393.

87. Esumi, K.; Matsuhisa, K.; Torigoe, K. Preparation of rodlike gold particles by UV irradiation using cationic micelles as a template. *Langmuir* **1995**, *11*, 3285-3287.

88. Foss, C.A.; Hornyak, G.L.; Stockert, J.A.; Martin, C.R. Optical properties of composite membranes containing arrays of nanoscopic gold cylinders. *J. Phys. Chem.* **1992**, *96*, 7497-7499.

89. Huang, X.; Neretina, S.; El-Sayed, M.A. Gold nanorods: From synthesis and properties to biological and biomedical applications. *Adv. Mater.* **2009**, *21*, 4880–4910.

90. Kelly, K.L.; Coronado, E.; Zhao, L.L.; Schatz, G.C. The optical properties of metal nanoparticles: The influence of size, shape, and dielectric environment. *J. Phys. Chem. B* **2003**, *107*, 668-677.

91. Gans, R. Form of ultramicroscopic particles of silver. *Ann. Phys.* **1915**, *47*, 270-U214.

92. Jain, P.K.; Huang, X.; El-Sayed, I.H.; El-Sayed, M.A. Noble Metals on the Nanoscale: Optical and Photothermal Properties and Some Applications in Imaging, Sensing, Biology, and Medicine. *Acc. Chem. Res.* **2008**, *41*, 1578–1586.

93. Mody, V.V.; Siwale, R.; Singh, A.; Mody, H.R. Introduction to metallic nanoparticles. *J Pharm Bioall Sci.* **2010**, *2*, 282-289.

94. Yguerabide J; EE, Y. Light-scattering submicroscopic particles as highly fluorescent analogs and their use as tracer labels in clinical and biological applications - I. Theory. *Anal. Biochem.* **1998**, *262*, 137-156.

95. Link, S.; El-Sayed, M.A. Shape and size dependence of radiative, non-radiative and photothermal properties of gold nanocrystals. *Int. Reviews in Physical Chemistry* **2000**, *19*, 409-453.

96. Tong, L.; Wei, Q.; Wei, A.; Cheng, J. Gold nanorods as contrast agents for biological imaging: optical properties, surface conjugation and photothermal effects. *Photochem Photobiol.* **2009**, *85*, 21-32.

97. Yu, C.; Nakshatri, H.; Irudayaraj, J. Identity profiling of cell surface markers by multiplex gold nanorod probes. *Nano Lett.* **2007**, *7*, 2300–2306.

98. Huang, X.; El-Sayed, I.H.; Qian, W.; El-Sayed, M.A. Cancer cell imaging and photothermal therapy in the near-infrared region by using gold nanorods. *J. Am. Chem. Soc.* **2006**, *128*, 2115–2120.

99. Ding, H.; Yong, K.-T.; Roy, I.; Pudavar, H.E.; Law, W.C.; Bergey, E.J.; Prasad, P.N. Gold Nanorods Coated with Multilayer Polyelectrolyte as Contrast Agents for Multimodal Imaging. *J. Phys. Chem. C* **2007**, *111*, 12552–12557.

100. Chen, C.-C.; Lin, Y.-P.; Wang, C.-W.; Tzeng, H.-C.; Wu, C.-H.; Chen, Y.-C.; Chen, C.-P.; Chen, L.-C.; Wu, Y.-C. DNA−Gold Nanorod Conjugates for Remote Control of Localized Gene Expression by near Infrared Irradiation. *J. Am. Chem. Soc.* **2006**, *128*, 3709–3715.

101. Niidome, T.; Akiyama, Y.; Shimoda, K.; Kawano, T.; Mori, T.; Katayama, Y.; Niidome, Y. In vivo monitoring of intravenously injected gold nanorods using near-infrared light. *Small* **2008**, *4*, 1001-1007.

102. Vives, E.; Schmidt, J.; Pelegrin, A. Cell-penetrating and cell-targeting peptides in drug delivery. *Biochim. Biophys. Acta* **2008**, *1786*, 126-138.

103. Dietz, G.P.; Bahr, M. Delivery of bioactive molecules into the cell: the Trojan horse approach. *Mol. Cell. Neurosci.* **2004**, *27*, 85-131.

104. Vives, E. Present and future of cell-penetrating peptide mediated delivery systems: "is the Trojan horse too wild to go only to Troy?". *J. Control. Release* **2005**, *109*, 77-85.

105. Richard, J.P.; Melikov, K.; Vives, E.; Ramos, C.; Verbeure, B.; Gait, M.J.; Chernomordik, V.L.; Lebleu, B. Cell-penetrating peptides: a reevaluation of the mechanism of cellular uptake. *J. Biol. Chem.* **2003**, *278*, 585-590.

106. Beer, A.J.; Haubner, R.; Sarbia, M.; Goebel, M.; Luderschmidt, S.; Grosu, A.L.; O Schnell; Niemeyer, M.; Kessler, H.; Wester, H.J.; Weber, W.A.; Schwaiger, M. Positron emission tomography using [18F]Galacto-RGD identifies the level of integrin alpha(v)beta3 expression in man. *Clin. Cancer Res.* **2006**, *12*, 3942–3949.

107. Hart, S.L.; Knight, A.M.; Harbottle, R.P.; Mistry, A.; Hunger, H.D.; Cutler, D.F.; Williamson, R.; Coutelle, C. Cell Binding and Internalization by filamentous phage displaying a Cyclic Arg-Gly-Asp-containing peptide. *J. biol. chem.* **1994**, *269*, 12468-12474.

108. Shadidi, M.; Sioud, M. Identification of novel carrier peptides for the specific delivery of therapeutics into cancer cells. *FASEB J.* **2003**, *17*, 256-258.

109. Holbro, T.; Civenni, G.; Hynes, N.E. The ErbB receptors and their role in cancer progression. *Exp. Cell. Res.* **2003**, *284*, 99-110.

110. Bajaj, M.; Waterfield, M.D.; Schlessinger, J.; Taylor, W.R.; Blundell, T. On the tertiary structure of the extracellular domains of the epidermal growth-factor and insulin-receptors. *Biochim. Biophys. Acta* **1987**, *916*, 220-226.

111. Ward, C.W.; Hoyne, P.A.; Flegg, R.H. Insulin and epidermal growth-factor receptors contain the cysteine repeat motif found in the tumor-necrosis-factor receptor. *Proteins* **1995**, *22*, 141-153.

112. Garrett, T.P.J.; McKern, N.M.; Lou, M.; Elleman, T.C.; Adams, T.E.; Lovrecz, G.O.; Kofler, M.; Jorissen, R.N.; Nice, E.C.; Burgess, A.W.; Ward, C.W. The crystal structure of a truncated ErbB2 ectodomain reveals an Active Conformation, Poised to interact with other ErbB Receptors. *Mol. Cell* **2003**, *11*, 495-505.

113. Harari, P.M.; Wheeler, D.L.; Grandis, J.R. Molecular target approaches in head and neck cancer: epidermal growth factor receptor and beyond. *Semin. Radiat. Oncol.* **2009**, *19*, 63-68.

114. Harari, D.; Yarden, Y. Molecular mechanisms underlying ErbB2/HER2 action in breast cancer. *Oncogene* **2000**, *19*, 6102-6114.

115. Yarden, Y.; Sliwkowski, M.X. Untangling the ErbB signalling network. *Nat. Rev. Mol. Cell Biol.* **2001**, *2*, 127-137.

116. Brigati, J.R.; Samoylova, T.I.; Jayanna, P.K.; Petrenko, V.A. Phage display technique for generating peptide reagents. In *Current Protocols in Protein Science*; John Wiley & Sons: 2008; Vol. 51, pp. 18.19.11-18.19.27.

117. Kehoe, J.W.; Kay, B.K. Filamentous phage display in the new millennium. *Chem. Rev.* **2005**, *105*, 4056-4072.

118. Shukla, G.S.; Krag, D.N. Phage display selection for cell-specific ligands: Development of a screening procedure suitable for small tumor specimens. *J. Drug Target.* **2005**, *13*, 7-18.

119. Samoylova, T.I.; Petrenko, V.A.; Morrison, N.E.; Globa, L.P.; Baker, H.J.; Cox, N.R. Phage probes for malignant glial cells. *Mol. Cancer Ther.* **2003**, *2*, 1129-1137.

120. Mount, J.D.; Samoylova, T.I.; Morrison, N.E.; Cox, N.R.; Baker, H.J.; Petrenko, V.A. Cell targeted phagernid rescued by preselected landscape phage. *Gene* **2004**, *341*, 59-65.

121. Jayanna, P.K.; Torchilin, V.P.; Petrenko, V.A. Liposomes targeted by fusion phage proteins. *Nanomedicine* **2009**, *5*, 83-89.

122. Petrenko, V.A. Evolution of Phage Display: From Bioactive Peptides to Bioselective Nanomaterials *Expert Opinion on Drug Delivery* **2008**, *5*, 825-836.

123. Petrenko, V.A.; Smith, G.P.; Gong, X. A library of organic landscapes on filamentous phage. *Protein Engi.* **1996**, *9*, 797-801.

124. Smith, G.P.; Scott, J.K. Libraries of peptides and proteins displayed on filamentous phage. *Methods Enzymol.* **1993**, *217*, 228-257.

125. Samoylova, T.I.; Cox, N.R.; Morrison, N.E.; Globa, L.P.; Romanov, V.; Baker, H.J.; Petrenko, V.A. Phage matrix for isolation of glioma cell-membrane proteins. *Biotechniques* **2004**, *37*, 2-7.

126. Lu, T.K.; Collins, J.J. Dispersing biofilms with engineered enzymatic bacteriophage. *Proc. Natl. Acad. Sci. USA* **1999**, *104*, 11197–11202.

127. Smith, G.P.; Petrenko, V.A.; Matthews, L.J. Cross-linked filamentous phage as an affinity matrix. *J. Immunol. Methods.* **1998**, *215*, 151-161.

128. Samoylova, T.; Cox, N.; Morrison, N.; Globa, L.; Romanov, V.; Baker, H.; Petrenko, V. Phage matrix for isolation of glioma cell membrane proteins. *Biotechniques.* **2004**, *37*, 254-260.

129. Abbineni, G.; Modali, S.; Safiejko-Mroczka, B.; Petrenko, V.; Mao, C.B. Evolutionary selection of new breast cancer cell-targeting peptides and phages with the cell-targeting peptides fully displayed on the major coat and their effects on actin dynamics during cell internalization. *Mol. Pharmaceutics* **2010**, *7*, 1629–1642.

130. Abbineni, G.; Safiejko-Mroczka, B.; Mao, C.B. Development of an optimized protocol for studying the interaction of filamentous bacteriophage with mammalian cells by fluorescence microscopy. *Microsc. Res. Tech* **2010**, *73*, 548-554.

131. Mandava, S.; Makowski, L.; Devarapalli, S.; Uzubell, J.; Rodi, D.J. RELIC - A bioinformatics server for combinatorial peptide analysis and identification of protein-ligand interaction sites. *Proteomics* **2004**, *4*, 1439-1460.

132. Carter, D.M.; Gagnon, J.N.; Damlaj, M.; Mandava, S.; Makowski, L.; Rodi, D.J.; Pawelek, P.D.; Coulton, J.W. Phage display reveals multiple contact sites between FhuA, an outer membrane receptor of Escherichia coli, and TonB. *J. Mol. Biol.* **2006**, *357* 236-251

133. Makowski, L.; Soares, A. Estimating the diversity of peptide populations from limited sequence data. *Bioinformatics* **2003**, *19*, 483-489.

134. Rodi, D.J.; Soares, A.S.; Makowski, L. Quantitative assessment of peptide sequence diversity in M13 combinatorial peptide phage display libraries. *J. Mol. Biol.* **2002**, *322*, 1039-1052.

135. Khalil, I.A.; Kogure, K.; Akita, H.; Harashima, H. Uptake pathways and subsequent intracellular trafficking in nonviral gene delivery. *Pharmacol Rev* **2006**, *58*, 32-45.

136. Gitisa, V.; Adina, A.; Nasserb, A.; Guna, J.; Lev, O. Fluorescent dye labeled bacteriophages—a new tracer for the investigation of viral transport in porous media: Introduction and characterization *Water Research* **2002**, *36*, 4227-4234.

137. Nooren, I.M.A.; Thornton, J.M. Diversity of protein-protein interactions. *EMBO J.* **2003**, *22*, 3486-3492.

138. Roskoski, R. The ErbB/HER receptor protein-tyrosine kinases and cancer. *Biochem. Biophys. Res. Commun.* **2004**, *319*, 1-11.

139. Shukla, G.S.; Krag, D.N. Selection of tumor- targeting agents on freshly excised human breast tumors using a phage display library. *Oncol. Rep.* **2005**, *13*, 757-764.

140. Fernandez-Carneado, J.; Kogan, M.J.; Castel, S.; Giralt, E. Potential peptide carriers: Amphipathic proline-rich peptides derived from the n-terminal domain of gamma-zein. *Angew. Chem. Int. Ed.* **2004**, *43*, 1811-1814.

141. Foerg, C.; Ziegler, U.; Fernandez-Carneado, J.; Giralt, E.; Rennert, R.; Beck-Sickinger, A.; Merkle, H. Decoding the entry of two novel cell-penetrating peptides in HeLa cells: Lipid raft-mediated endocytosis and endosomal escape. *Biochemistry* **2005**, *44*, 72-81.

142. Fernandez-Carneado, J.; Kogan, M.J.; Mau, N.V.; Pujals, S.; Lopez-Iglesias, C.; Heitz, F.; Giralt, E. Fatty acyl moieties: improving Pro-rich peptide uptake inside HeLa cells. *J. Pept. Res.* **2005**, *65*, 580-590.

143. Pujals, S.; Fernandez-Carneado, J.; Kogan, M.J.; Martinez, J.; Cavelier, F.; Giralt, E. Replacement of a proline with silaproline causes a 20-fold increase in the cellular uptake of a pro-rich peptide. *J. Am. Chem. Soc.* **2006**, *128*, 8479–8483.

144. Kaksonen, M.; Sun, Y.; Drubin, D.G. A pathway for association of receptors, adaptors, and actin during endocytic internalization. *Cell* **2003**, *115*, 475–487.

145. Kaksonen, M.; Toret, C.P.; Drubin, D.G. Harnessing actin dynamics for clathrin-mediated endocytosis. *Nature Rev. Mol. Cell. Biol.* **2006**, *7*, 404-414.

146. Merrifield, C.J. Seeing is believing: imaging actin dynamics at single sites of endocytosis *Trends. Cell Biol.* **2004**, *14*, 352-358.

147. Engqvist-Goldstein, A.E.; Drubin, D.G. Actin assembly and endocytosis: From yeast to mammals. *Annu. Rev. Cell. Dev. Biol.* **2003**, *19*, 287-332.

148. Conner, S.D.; Schmid, S.L. Regulated portals of entry into the cell. *Nature* **2003**, *422*, 37-44.

149. Qualmann, B.; Kessels, M.M.; Kelly, R.B. Molecular Links between Endocytosis and the Actin Cytoskeleton. *J Cell Biol* **2000**, *150*, 111-116.

150. Pollard, T.D. Actin. *Curr. Opin. Cell Biol.* **1990**, *2*, 33-40.

151. Copper, J.A. The role of actin polymerization in cell motility. *Annu. Rev. Physiol.* **1991**, *53*, 585-605.

152. Heath, J.; Holifield, B. Actin alone in lamellipodia. *Nature* **1991**, *352*, 107-108.

153. Theriot, J.A.; Mitchison, T.J. Actin microfilament dynamics in locomoting cells. *Nature* **1991**, *352*, 126-131.

154. Stossel, T. On the crawling of animal cells *Science* **1993**, *260*, 1086-1093.

155. Zigmond, S.H. Recent quantitative studies of actin filament turnover during cell locomotion. *Cell Motil. Cytoskeleton* **1993**, *25*, 309-316.

156. Welch, M.D.; Mallavarapu, A.; Rosenblatt, J.; Mitchison, T.J. Actin dynamics in vivo. *Curr. Opin. Cell Biol.* **1997**, *9*, 54-61.

157. Safiejko-Mroczka, B.; Bell, P.B. Distribution of cytoskeletal proteins in neomycin-induced protrusions of human fibroblasts. *Exp. Cell Res.* **1998**, *242*, 495-514.

158. Safiejko-Mroczka, B.; Bell, P.B. Reorganization of the actin cytoskeleton in the protruding lamellae of human fibroblasts. *Cell Motil. Cytoskeleton* **2001**, *50*, 13-32.

159. Abbineni, G.; Safiejko-Mroczka, B.; Mao, C. Development of an optimized protocol for studying the interaction of filamentous bacteriophage with mammalian cells by fluorescence microscopy. *Microsc. Res. Tech.* **2010**, *73*, 548-554.

160. Greene, W.; Gao, S.-J. Actin dynamics regulate multiple endosomal steps during Kaposi's sarcoma-associated herpesvirus entry and trafficking in endothelial cells. *PLoS Pathog.* **2009**, *5*, 1-18.

161. Sun, X.; Whittaker, G.R. Role of the actin cytoskeleton during influenza virus internalization into polarized epithelial cells. *Cell Microbiol.* **2007**, *9*, 1672-1682.

162. Dausend, J.; Musyanovych, A.; Dass, M.; Walther, P.; Schrezenmeier, H.; Landfester, K.; Mailander, V. Uptake mechanism of oppositely charged fluorescent nanoparticles in HeLa cells. *Macromol. Biosci.* **2008**, *8*, 1135-1143.

163. Weissleder, R. Molecular imaging in cancer. *Science* **2006**, *312*, 1168-1171.

164. Downing, G. Materials and biology. Nanotechnology takes aim at cancer. *Science* **2005**, *310*, 1132-1134.

165. Ferrari, M. Cancer nanotechnology: opportunities and challenges. *Nat Rev Cancer* **2005**, *5*, 161-171.

166. Vargo-Gogola, T.; Rosen, J.M. Modelling breast cancer: one size does not fit all. *Nat Rev Cancer* **2007**, *7*, 659-672.

167. Herschman, H.R. Molecular Imaging: Looking at problems, seeing solutions. *Science* **2003**, *302*, 605-608.

168. Lal, S.; Clare, S.E.; Halas, N.J. Nanoshell-enabled photothermal cancer therapy: impending clinical impact. *Acc Chem Res* **2008**, *41*, 1842-1851.

169. Eghtedari, M.; Liopo, A.V.; Copland, J.A.; Oraevsky, A.A.; Motamedi, M. Engineering of hetero-functional gold nanorods for the in vivo molecular targeting of breast cancer cells. *Nanoletters* **2009**, *9*, 287-291.

170. Huang, X.; El-Sayed, I.H.; Qian, W.; El-Sayed, M.A. Cancer cell imaging and photothermal therapy in the near-infrared region by using gold nanorods. *J. Am. Chem. Soc.* **2006**, *128*, 2115-2120.

171. Petrenko, V. Evolution of phage display from bioactive peptides to bioselective nanomaterials. *Expert Opin Drug Deliv* **2008**, *5*, 1-12.

172. Pietersz, G.A.; McKenzie, I.F.C. Antibody conjugates for the treatment of cancer. *Immunol Rev* **1992**, *129*, 57-80.

173. Scott, J.K.; Smith, G.P. Searching for peptide ligands with an epitope library. *Science* **1990**, *249*, 386-390.

174. Lee, Y.J.; Yi, H.; Kim, W.-J.; Kang, K.; Yun, D.S.; Strano, M.S.; Ceder, G.; Belcher, A.M. Fabricating genetically engineered high-power lithium-ion batteries using multiple virus genes. *Science* **2009**, *324*, 1051-1055.

175. Merril, C.R.; Scholl, D.; Adhya, S.L. The prospect for bacteriophage therapy in Western medicine. *Nat. Rev. Drug. Discovery* **2003**, *2*, 489-497.

176. Petrenko, V.A.; Smith, G.P.; Gong, X.; Quinn, T. A library of organic landscapes on filamentous phage. *Protein Engineering* **1996**, *9*, 797-801.

177. Giordano, R.; Cardó-Vila, M.; Lahdenranta, J.; Pasqualini, R.; Arap, W. Biopanning and rapid analysis of selective interactive ligands. *Nat. Med.* **2001**, *7*, 1249-1253.

178. Sprujit, R.; Wolfs, C.; Hemminga, M. Aggregation-related conformational change of the membrane-associated coat protein of bacteriophage M13. *Biochemistry* **1989**, *28*, 9158-9165.

179. Abbineni, G.; Modali, S.; Safiejko-Mroczka, B.; Petrenko, V.; Mao, C. Evolutionary selection of new breast cancer cell-targeting peptides and phages with the cell-targeting peptides fully displayed on the major coat and their effects on actin dynamics during cell internalization *Molecular Pharmaceutics* **2010**.

180. Knippers, R.; Hoffmann-Berling, H. A Coat Protein from Bacteriophage fd Hydrodynamic measurements and biological characterization. *J. Mol. Biol.* **1966**, *1966*, 281-292.

181. Williams, R.W.; Dunker, A.K. Circular dichroism studies of fd coat protein in membrane vesicles. *J Biol Chem* **1977**, *252*, 6253-6255.

182. Ni, W.; Yang, Z.; Chen, H.; Li, L.; Wang, J. Coupling between Molecular and Plasmonic Resonances in Freestanding Dye−Gold Nanorod Hybrid Nanostructures. *J. Am. Chem. Soc.* **2008**, *130*, 6692-6693.

183. Tedesco, A.C.; Oliveira, D.M.; Lacavaa, Z.G.M.; Azevedo, R.B.; Lima, E.C.D.; Gansau, C.; Buske, N.; Morais, P.C. Determination of binding constant Kb of biocompatible, ferrite-based magnetic fluids to serum albumin. *Journal Of Applied Physics* **2003**, *93*, 6704-6706.

184. Hansen, M.B.; Nielsen, S.E.; Berg, K. *J. Immunol. Methods* **1989**, *119*, 203-210.

185. Jeffrey, E.M.; Linda, A.S.; Andrew, M.O.I. A rapid and simple MTT- based spectrophotometric assay for determining drug sensitivity in monolayer cultures *Journal of Tissue Culture Methods* **1988**, *11*, 15-17.

186. Dozmorov, I.; Knowlton, N.; Tang, Y.; Shields, A.; Pathipvanich, P.; Jarvis, J.N.; Centola, M. Hypervariable genes--experimental error or hidden dynamics. *Nucleic Acids Res* **2004**, *32*, e147.

187. Dozmorov, I.; Lefkovits, I. Internal standard-based analysis of microarray data. Part 1: analysis of differential gene expressions. *Nucleic Acids Res* **2009**, *37*, 6323-6339.

188. Dennis, G., Jr.; Sherman, B.T.; Hosack, D.A.; Yang, J.; Gao, W.; Lane, H.C.; Lempicki, R.A. DAVID: Database for Annotation, Visualization, and Integrated Discovery. *Genome Biol* **2003**, *4*, P3.

189. Jung, L.S.; Campbell, C.T.; Chinowsky, T.M.; Mar, M.N.; Yee, S.S. Quantitative Interpretation of the Response of Surface Plasmon Resonance Sensors to Adsorbed Films. *Langmuir* **1998**, *14*, 5636-5648.

190. Huang, X.; El-Sayed, I.H.; Qian, W.; El-Sayed, M.A. Cancer cell imaging and photothermal therapy in the near-infrared region by using gold nanorods. *J Am Chem Soc* **2006**, *128*, 2115-2120.

191. Villanueva, A.; Canete, M.; Roca, A.G.; Calero, M.; Veintemillas-Verdaguer, S.; Serna, C.J.; Morales Mdel, P.; Miranda, R. The influence of surface

functionalization on the enhanced internalization of magnetic nanoparticles in cancer cells. *Nanotechnology* **2009**, *20*, 115103.

192. Eidi, H.; Joubert, O.; Attik, G.; Duval, R.E.; Bottin, M.C.; Hamouia, A.; Maincent, P.; Rihn, B.H. Cytotoxicity assessment of heparin nanoparticles in NR8383 macrophages. *Int J Pharm* **2010**.

193. Rajangam, K.; Behanna, H.A.; Hui, M.J.; Han, X.; Hulvat, J.F.; Lomasney, J.W.; Stupp, S.I. Heparin binding nanostructures to promote growth of blood vessels. *Nano Lett* **2006**, *6*, 2086-2090.

194. Olbrich, C.; Gessner, A.; Schroder, W.; Kayser, O.; Muller, R.H. Lipid-drug conjugate nanoparticles of the hydrophilic drug diminazene-cytotoxicity testing and mouse serum adsorption. *J Control Release* **2004**, *96*, 425-435.

195. Tang, N.; Du, G.; Wang, N.; Liu, C.; Hang, H.; Liang, W. Improving penetration in tumors with nanoassemblies of phospholipids and doxorubicin. *J Natl Cancer Inst* **2007**, *99*, 1004-1015.

196. Ma, Y.J.; Gu, H.C. Study on the endocytosis and the internalization mechanism of aminosilane-coated Fe3O4 nanoparticles in vitro. *J Mater Sci Mater Med* **2007**, *18*, 2145-2149.

197. Shiku, H.; Wang, L.; Ikuta, Y.; Okugawa, T.; Schmitt, M.; Gu, X.; Akiyoshi, K.; Sunamoto, J.; Nakamura, H. Development of a cancer vaccine: peptides, proteins, and DNA. *Cancer Chemother Pharmacol* **2000**, *46 Suppl*, S77-82.

198. Chen, M.; Singer, L.; Scharf, A.; von Mikecz, A. Nuclear polyglutamine-containing protein aggregates as active proteolytic centers. *J Cell Biol* **2008**, *180*, 697-704.

199. Gilcrease, M.Z.; Zhou, X.; Lu, X.; Woodward, W.A.; Hall, B.E.; Morrissey, P.J. Alpha6beta4 integrin crosslinking induces EGFR clustering and promotes EGF-mediated Rho activation in breast cancer. *Journal of Experimental & Clinical Cancer Research* **2009**, *28*, 1-10.

200. Melancon, M.P.; Lu, W.; Yang, Z.; Zhang, R.; Cheng, Z.; Elliot, A.M.; Stafford, J.; Olson, T.; Zhang, J.Z.; Li, C. In vitro and in vivo targeting of hollow gold nanoshells directed at epidermal growth factor receptor for photothermal ablation therapy. *Mol. Cancer. Ther.* **2008**, *7*, 1730-1739.

201. Huang, X.; Jain, P.K.; El-Sayed, I.H.; El-Sayed, M.A. Plasmonic photothermal therapy (PPTT) using gold nanoparticles. *Lasers Med. Sci.* **2008**, *23*, 217-228.

202. Rosi, N.L.; Giljohann, D.A.; Thaxton, C.S.; Lytton-Jean, A.K.R.; Han, M.S.; Mirkin†, C.A. Oligonucleotide-modified gold nanoparticles for intracellular gene regulation. *Science* **2006**, *312*, 1027-1030.

203. Nazaruk, E.; Sadowska, K.; Biernat, J.; Rogalski, J.; Ginalska, G.; Bilewicz, R. Enzymatic electrodes nanostructured with functionalized carbon nanotubes for biofuel cell applications. *Anal Bioanal Chem* **2010**, 1-10.

204. Qi, P.; Vermesh, O.; Grecu, M.; Javey, A.; Wang, Q.; Dai, H. Toward large arrays of multiplex functionalized carbon nanotube sensors for highly sensitive and selective molecular detection. *Nano Lett.* **2003**, *3*, 347–351.

205. Guo, S.; Pan, X.; Gao, H.; Yang, Z.; Zhao, J.; Bao, X. Probing the electronic effect of carbon nanotubes in catalysis: NH(3) synthesis with Ru nanoparticles. *Chemistry* **2010**, *16*, 5379-5384.

206. Chakravarty, P.; Qian, W.; El-Sayed, M.; Prausnitz, M. Delivery of molecules into cells using carbon nanoparticles activated by femtosecond laser pulses. *Nat Nanotechnol* **2010**, *5*, 607-611.

207. Al-Jamal, K.; Toma, F.; Yilmazer, A.; Ali-Boucetta, H.; Nunes, A.; Herrero, M.; Tian, B.; Eddaoui, A.; Al-Jamal, W.; Bianco, A.; Prato, M.; Kostarelos, K. Enhanced cellular internalization and gene silencing with a series of cationic dendron-multiwalled carbon nanotube:siRNA complexes. *FASEB J.* **2010**, *Epub ahead of print*.

208. Kam, N.W.S.; O'Connell, M.; Wisdom, J.A.; Dai, H. Carbon nanotubes as multifunctional biological transporters and near-infrared agents for selective cancer cell destruction. *PNAS* **2005**, *102*, 11600-11605

209. Pantarotto, D.; Singh, R.; McCarthy, D.; Erhardt, M.; Briand, J.-P.; Prato, M.; Kostarelos, K.; Bianco, A. Functionalized carbon nanotubes for plasmid DNA gene delivery. *Angew. Chem. Int. Ed.* **2004**, *43*, 5242 –5246.

210. Petrenko, V.A. Evolution of phage display: from bioactive peptides to bioselective nanomaterials. *Expert Opin. Drug Discovery* **2008**, *5*, 825-836.

211. Abbineni, G.; Safiejko-Mroczka, B.; Mao, C.B. Development of an optimized protocol for studying the interaction of filamentous bacteriophage with mammalian cells by fluorescence microscopy. *Microsc. Res. Tech.* **2010**, *73*, 548-554.

212. Dolmans, D.; Fukumura, D.; Jain, R. Photodynamic therapy for cancer. . *Nat. Rev. Cancer.* **2003**, *3*, 380-387.

213. Gandra, N.; Abbineni, G.; Mao, C. Bacteriophage-enabled targeted photodynamic cancer therapy. *Submitted* **2010**.

214. Salvati, A.; Ristori, S.; Oberdisse, J.; Spalla, O.; Ricciardi, G.; Pietrangeli, D.; Giustini, M.; Martini, G. Small angle scattering and zeta potential of liposomes loaded with octa(carboranyl)porphyrazine. *J. Phys. Chem. B* **2007**, *111*, 10357–10364.

215. Ngweniform, P.; Abbineni, G.; Cao, B.; Mao, C.B. Self-assembly of drug-loaded liposomes on genetically engineered target-recognizing M13 phage: a novel nano-carrier for targeted drug delivery. *Small* **2009**, *5*, 1963-1969.

216. Smith, G.; Scott, J. Libraries of peptides and proteins displayed on filamentous phage. *Methods in enzymology* **1993**, *217*, 228.

217. Brigati, J.; Williams, D.; Sorokulova, I.; Nanduri, V.; Chen, I. Diagnostic probes for Bacillus anthracis spores selected from a landscape phage library. *Clinical chemistry* **2004**, *50*, 1899.

218. Spruijt, R.B.; Wolfs, C.J.A.M.; Hemminga, M.A. Aggregation related conformational change of the membrane-associated coat protein of bacteriophage M13. *Biochemistry* **1989**, *28*, 9158-9165.

219. Kam, N.W.S.; Liu, Z.; Dai, H. Carbon nanotubes as intracellular transporters for proteins and DNA: An investigation of the uptake mechanism and pathway. *Angew. Chem. Int. Ed.* **2006**, *45*, 577-581.

220. Brunner, J.; Skrabal, P.; Hauser, H. Single bilayer vesicles prepared without sonication physico-chemical properties *Biochim. Biophys. Acta* **1976**, *455*, 322-331.

221. Spiller, W.; Kliesch, H.; Wöhrle, D.; Hackbarth, S.; Röder, B.; Schnurpfeil, G. Singlet oxygen quantum yields of different photosensitizers in polar solvents and micellar solutions. *Porphyr. Phthalocyanines* **1998**, *2*, 145-158.

222. Wilson, R.W.; Bloomfield, V.A. Counterion-induced condensation of deoxyribonucleic acid. A light-scattering study. *Biochemistry* **1979**, *18*, 2192-2196.

223. Smith, G.P.; Petrenko, V.A. Phage display *Chem. Rev.* **1997**, *97*, 391-410.